Title

Subensemble Investigations of Molecular Catalysts: Revealing Heterogeneity via Microscopy

Author

Easter, Quinn T

Publication Date

2018

Peer reviewed|Thesis/dissertation

UNIVERSITY OF CALIFORNIA,
IRVINE

Subensemble Investigations of Molecular Catalysts: Revealing Heterogeneity via Microscopy

DISSERTATION

submitted in partial satisfaction of the requirements
for the degree of

DOCTOR OF PHILOSOPHY

in Chemistry

by

Quinn Thomas Easter

Dissertation Committee:
Professor Suzanne A. Blum, Chair
Professor David L. Van Vranken
Assistant Professor Shane Ardo

2018

Table of Contents

Page

List of Figures

List of Tables

Acknowledgements

I would first like to thank my advisor, Professor Suzanne A. Blum, for all of her guidance and mentorship throughout my graduate career. Suzanne was instrumental in helping me develop as a scientist, and she has always encouraged me to do my best in all things chemistry. I am grateful for the opportunity to have had her as my advisor, and I have learned a lot from her.

Thank you to my committee members, Professor David L. Van Vranken and Professor Shane Ardo, for serving as the other members of my dissertation committee.

The research I conducted would not have been possible without funding. I acknowledge the University of California, Irvine (UCI), the Department of Energy (DOE), and the National Science Foundation (NSF) for financial support in the form of research assistantships and research supplies during my time as a Ph.D. student at UCI.

I thank fellow UCI Ph.D. students, Ph.D.'s, and friends outside of UCI for their advice and friendship.

I am deeply grateful to Mateus, for all his support and encouragement, and especially for him being there for me through all the challenges I faced during my graduate career. I am so blessed and grateful to have him in my life and cannot wait to see our next chapters unfold!

I would like to thank my extended family for their support, especially my Aunt Sue without whom I would not have an endless supply of excellent literature!

Finally, I cannot thank my parents Ed and Debbie Easter enough for everything in my life. They taught me the importance of hard work ethic and supported me even when I had to move far away from home. They have been the most wonderful source of support I could ever ask for, and I am forever grateful and truly blessed to be their son. I love you!

Curriculum Vitae
Quinn T. Easter

EDUCATION AND TRAINING

2012–2018 **Ph.D.** Physical Organic Chemistry, *University of California*, Irvine, CA

Thesis title: "Subensemble Investigations of Molecular Catalysts: Revealing Heterogeneity via Microscopy"
Advisor: Prof. Suzanne A. Blum

2008–2012 **B.S.** Chemistry, *Indiana University*, Bloomington, IN
Advisor: Prof. Caroline C. Jarrold

PUBLICATIONS

7. **Easter, Q. T.**; Blum, S. A. "Time-Variable Catalytic Polymerization Kinetics at the Single-Particle and Single-Turnover Level." *In preparation*.
6. **Easter, Q. T.**; Blum, S. A. "Kinetics of the Same Reaction over Nine Orders of Magnitude in Concentration: When Are Unique Subensemble and Single-Turnover Reactivity Displayed?" *Submitted.*
5. **Easter, Q. T.**; Blum, S. A. "Evidence for Dynamic Chemical Kinetics at Individual Molecular Ruthenium Catalysts." *Angew. Chem. Int. Ed.* **2018**, *57*, 1572–1575.
4. **Easter, Q. T.**; Blum, S. A. "Single Turnover at Molecular Polymerization Catalysts Reveals Spatiotemporally Resolved Reactions." *Angew. Chem. Int. Ed.* **2017**, *56*, 13772–13775.

   Highlighted in *Angew. Chem. Int. Ed.* "Kinetics in the Real World."
   Highlighted in UCI News Brief, "Little green flashes unlock secrets of catalytic reactions."

3. Feng, C.; **Easter, Q. T.**; Blum, S. A. "Structure–Reactivity Studies, Characterization, and Transformation of Intermediates by Lithium Chloride in the Direct Insertion of Alkyl and Aryl Iodides to Metallic Zinc Powder." *Organometallics* **2017**, *36*, 2389–2396.

   Organometallics, Cover, July 2017.

2. Feng, C.; Cunningham, D. W.; **Easter, Q. T.**; Blum, S. A. "Role of LiCl in Generating Soluble Organozinc Reagents." *J. Am. Chem. Soc.* **2016**, *138*, 11156–11159.

   Highlighted in *Org. Process Res. Dev.* **2016**, *20*, 1691. "Some Items of Interest to Process Chemists and Engineers."

1. **Easter, Q. T.**; Trauschke, V.; Blum, S. A. "Catalyst Inefficiencies: Supported Ring-Opening Metathesis Polymerization Catalyst Yields Its Ensemble Rate from a Small Number of Molecular Active Sites." *ACS Catal.* **2015**, *5*, 2290–2295.

INDUSTRY EXPERIENCE

2012 Dow AgroSciences: Summer Internship
2011 Procter & Gamble: Summer Internship

PRESENTATIONS

2018 American Chemical Society 22nd Annual Green Chemistry & Engineering Conference
2017 American Chemical Society 253rd National Conference
2016 American Chemical Society 251st National Conference
2015 American Chemical Society 45th Western Regional Conference
2015 Southern California Society of Microscopy and Microanalysis

AWARDS AND FELLOWSHIPS

ACS Green Chemistry Institute Pharmaceutical Roundtable Student Travel Grant, 2018
Courson Greeves Scholarship, 2011 (departmental)
Indiana University Academic Excellence Award, 2008, 2009, 2010, 2011
Indiana University Valedictorian Award, 2008, 2009, 2010, 2011
Indiana University Hutton Honors College Scholarship, 2008, 2009, 2010, 2011
Indiana University County Scholarship, 2008

PROFESSIONAL AFFILIATIONS

2013–present American Chemical Society, Inorganic Division

Abstract of the Dissertation

Subensemble Investigations of Molecular Catalysts: Revealing Heterogeneity via Microscopy

By

Quinn Thomas Easter

Doctor of Philosophy in Chemistry

University of California, Irvine, 2018

Professor Suzanne A. Blum, Chair

The use of microscopy techniques to uncover the heterogeneity of molecular catalysts is herein reported. Prior to this work, molecular catalysts were detected and quantified through traditional ensemble analytical techniques, such as ^{1}H NMR spectroscopy and mass spectrometry, but no information existed on molecular catalyst activity of single catalysts or small ensembles. Although appearing efficient on the bulk scale, microscopy techniques (Chapter 2) indicated that despite a uniform distribution of catalyst, the catalytic activity of molecular catalysts was poorly distributed. Surface intermediates were transformed by LiCl into soluble organozinc reagents (Chapter 3). Using fluorescence microscopy, spatiotemporal resolution of single active molecular polymerization catalysts was achieved (Chapter 4), which was the first single-turnover fluorescence microscopy imaging at any molecular catalyst. These molecular polymerization catalysts were found to exhibit time-variant chemical kinetics (Chapter 5), rather than continue to exhibit uniform polymerization activity at all time points, in contrast to their traditional textbook depictions. Finally, boundary conditions were established through fluorescence microscopy on when unique subensemble and single-turnover catalytic activity could be detected (Chapter 6). These studies redefine the concept of a "uniform" or "average" catalyst and suggest broad applicability to understanding the full picture of catalysis.

Chapter 1

Introduction to Subensemble Investigations of Molecular Catalysts: Revealing Heterogeneity via Microscopy

Abstract: An introduction to the application of fluorescence microscopy to molecular catalysts is herein described. Organometallic chemistry is a widely studied branch of chemistry, yet observing single turnover and characterizing the chemical kinetics at individual molecular catalysts and at stoichiometric organometallic reagents has not yet been achieved. The benefits to observing these catalysts include knowledge of kinetic states and intermediates, defined structure-property relationships, and an understanding of how chemical kinetics of a reaction may be time variant. Prior characterization of this information relied on ensemble techniques, obscuring this chemical information of the system through averaging. Though previously resigned to the biological community, chemists have recently employed fluorescence microscopy to obtain information below the levels of ensemble averaging. The Blum Group has shown that using fluorescent probe molecules, chemical information on catalytic activity and stoichiometric organometallic reactions can be obtained at the single-reagent and single-catalytic turnover level, thus no longer depending on ensemble averaging. These probe molecules, and the underlying methodology behind observing catalytic activity, were successfully employed in this thesis work to obtain previously unknown information about the time variability of individual molecular catalysts. The broader impact of this work is to redefine the view of catalysis and, importantly, the concept of a "uniform" or "average" catalyst.

Introduction

Since the first synthesis of ferrocene reported in 1951,[1] organometallic chemistry has enjoyed rapid growth and has emerged as a key field in transforming organic molecules into valuable products using metal catalysts.[2,3] These catalysts function by lowering the energy needed for reactions to take place, permitting otherwise energetically unfavorable reactions to proceed. A depiction of this process in a catalytic cycle enables scientists to evaluate the pathways through which products are formed and the catalyst is regenerated. Further, using kinetics information obtained from ^{1}H NMR spectroscopy[4,5] and UV-vis spectroscopy,[6] rates of catalysis inform on catalytic efficiency and can provide insight into plausible mechanisms.

The underlying assumptions behind previous studies view catalysis in a "uniform" picture; that is, after catalyst initiation, all catalysts within a sample exhibit uniform activity and catalyze the reaction via a series of steps with fixed rate constants. Such a depiction implies that all molecular catalysts within a sample are identical. Indeed, molecular catalysts are often described as "well-defined"[7] due to their anticipated defined coordination environment. There are significant drawbacks to this view when considering molecular catalysts, which may not be detectible during catalysis, yet more than one active coordination environment might exist. For example, ligands can (re)associate with the metal center if the rate constant for this step is nonzero and may generate additional forms of active catalysts. Thus, catalyst sites or molecules in a sample might not be chemically equivalent, despite traditionally being considered this way. Traditional characterization techniques, such as ^{1}H NMR spectroscopy,[4,5] are able to uncover the distribution of kinetics of a reaction and resolve low concentration, transient chemical intermediates responsible for activity in a sample. These traditional characterization techniques provide average information from the entire sample, an effect known as ensemble averaging. Therefore, a significant amount of chemical

information, such as different structures and/or chemical kinetics is obscured by these techniques, since the information can neither be seen nor detected by them. Thus, the degree to which the concept of uniformity in molecular catalysis is a reasonable depiction remains almost completely unknown.

Another major drawback to the measurement of an "average catalyst" is the limited ability to understand how local environments impact catalysis. Due to micro- or nanoenvironment differences surrounding individual catalysts, some catalysts may be less accessible to substrate in the sample. A lack of accessibility to substrate limits the substrate from reaching the active site,[8] thereby potentially slowing down catalysis at some sites. Meanwhile, at uninhibited catalyst sites, catalysis continues with minimal interference. These hindered catalysts may constitute the majority of catalysis within the sample, whereas the hindered catalysts may contribute significantly less. Thus, the majority of catalysis may arise from a minor subpopulation. In this way, a structure-property relationship can be established between catalyst accessibility and catalytic activity. If nonuniform accessibility to substrate extends to the entire sample, then characterization of the individual constituents of the sample would provide unique insight into the structure-property relationships of these constituents. However, due to the aforementioned ensemble averaging, such relationships are obscured because the entire sample is averaged (Figure 1.1).

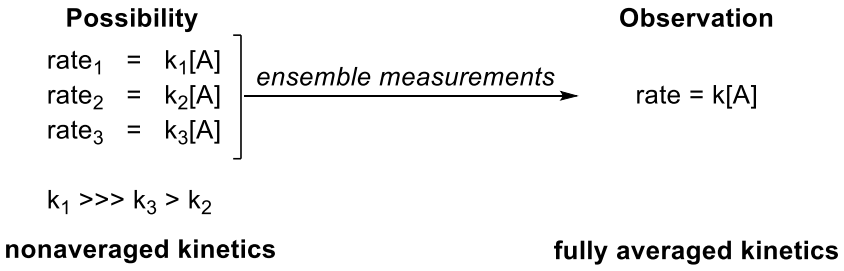

Figure 1.1. Nonaveraged kinetics of a reaction with varying rate constants become fully averaged and appear to have the same rate constant through ensemble measurements. Thus, the distribution of catalytic behavior is obscured.

Finally, underlying catalytic cycles, low-quantity intermediates, and structure-property relationships are the chemical kinetics of the system. Molecular catalysts are depicted within a catalytic cycle as having fixed rate constants that do not change over time,[3] regardless of monomer concentration. During the active state, it is unknown whether or not this active state persists throughout catalysis, or if the catalyst is cycling through different kinetic states of activity. Further, it is largely unknown if an individual catalyst cycles through highly active and then inactive states, leading to an intermediate average rate detected by ensemble techniques. Learning more about the kinetic states, including any time-dependent activity changes, would be of great value to inform on the next generation of catalyst design. However, given that monitoring of kinetic states of individual catalysts through ensemble averaging is unable to pinpoint any time-dependent changes in kinetics (Figure 1.1), aside from determining the overall reaction progress with respect to time, this information has remained obscured.

These three challenges highlight important missing information on characterization of catalytic activity below the levels of traditionally available measurement techniques. Understanding the complete picture of catalytic activity remains challenging, but a challenge that must be undertaken if the next generation of catalysts, possessing controllable activity, are to be designed. To address this challenge, a new approach to characterizing catalytic activity is needed.

Fluorescence microscopy has been extensively used in biological imaging to report on biological processes.[9–11] Through this microscopy technique, unique information about cellular processes has been discovered.[9–11] Single-molecule fluorescence microscopy has also been extensively developed, with the ability to detect single kinesin molecule movement along microtubules[8] and the exact positions of biomolecules.[12] Key to the success of fluorescence microscopy is the use of fluorophores,[13] or labeling probes that enable imaging. Fluorophores have

a wavelength of excitation, at which they most strongly absorb energy, and a wavelength of emission, at which they release this absorbed energy.[13] For many fluorophores, these wavelengths fall within the visible spectrum of light,[13] making it straightforward for visually observing events within a system. Importantly, due to the sensitivity of modern cameras and high signal from fluorescence, the available information through fluorescence microscopy provides a subensemble approach to analyzing a system. Thus, expanding this technique to chemical systems for monitoring catalytic activity would be ideal and would create a transformative approach to understanding organometallic chemistry and catalysis.

No example of employment of single-molecule/single-particle fluorescence microscopy to chemical systems existed until the seminal work from Hofkens in 2006,[14] which described the observation of single catalytic turnovers at crystal faces. Since this observation, the field of fluorescence microscopy as it relates to chemical systems has greatly expanded (Figure 1.2). Hofkens continued researching in fluorescence microscopy and described studies on polymers.[15] Chen and coworkers have described extensive studies on single catalytic turnover at gold nanoparticles and titanium nanorods, obtaining chemical kinetics and resolving locations of catalytic activity.[16] Weckhuysen and coworkers focused on the catalytic activity within zeolites.[17,18] Goldsmith and coworkers reported on ligand dissociation kinetics of palladium complexes,[19] an important step in precatalyst activation. Majima and coworkers developed single-molecule, single-particle approaches for exploring nanocatalyst structures and kinetics on solid catalysts.[20] Roeffaers and colleagues described the impact of porous structures on catalytic activity of crystals through a noninvasive microscopy approach.[21] Trapp, Jung, and Herten analyzed alternative olefin epoxidation reaction pathways by using single-molecule fluorescence microscopy.[22] Scaiano and colleagues detail catalytic behavior of samarium oxide nanoparticles

using fluorescence microscopy.[23] Finally, Wöll and coworkers report on using fluorescent photoswitches to visualize nanoscopic structures of soft materials.[24] These studies from other research groups highlight the importance of fluorescence microscopy within the global academic community.

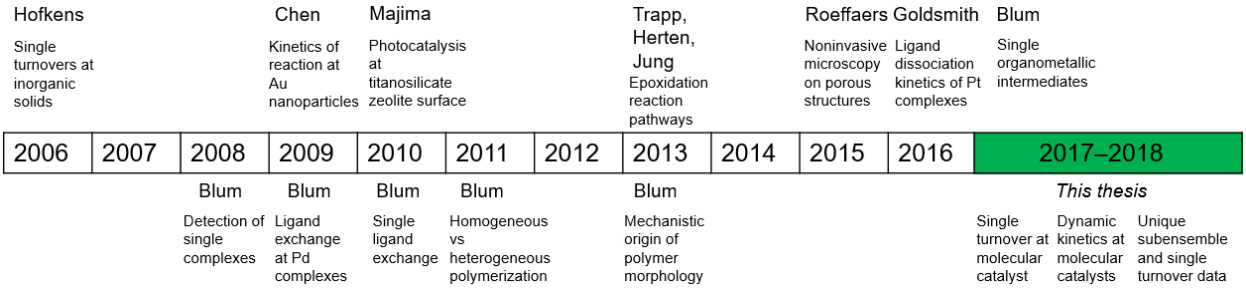

Figure 1.2. Timeline of fluorescence microscopy achievements by our group and others. Contributions to the field of fluorescence microscopy in this thesis are noted.

Research within the Blum Group[25–31] has focused on understanding catalytic activity using fluorescence microscopy and has made significant contributions to the community (Figure 1.2). Our group pioneered reaction imaging of individual molecular complexes and was the first to show that boron dipyrromethene (BODIPY) fluorophores can act as spectators during a chemical reaction, greatly expanding the strategy for imaging. As a spectator, the fluorescent core is not involved in any processes in which bonds are formed, but a chemical reaction at a distal reactive part of the molecule signals the location of the reaction (Figure 1.3). Thus, the same core can be attached to many different functional groups in order to image a range of reactions. After our development, this spectator approach was adopted by Goldsmith[19] and Scaiano.[23] This is in contrast to fluorophores that can turn on, turn off, or change colors during a chemical reaction, meaning the presence or disappearance of signal, or a color change signifies a chemical reaction where the probe gains or loses its ability to fluoresce, or where the emission wavelength is different due to a change in the bonding in the core, respectively.[13] This approach requires a fluorophore

core that is differently designed for each chemical reaction and was used in the original Hofkens paper in 2006.

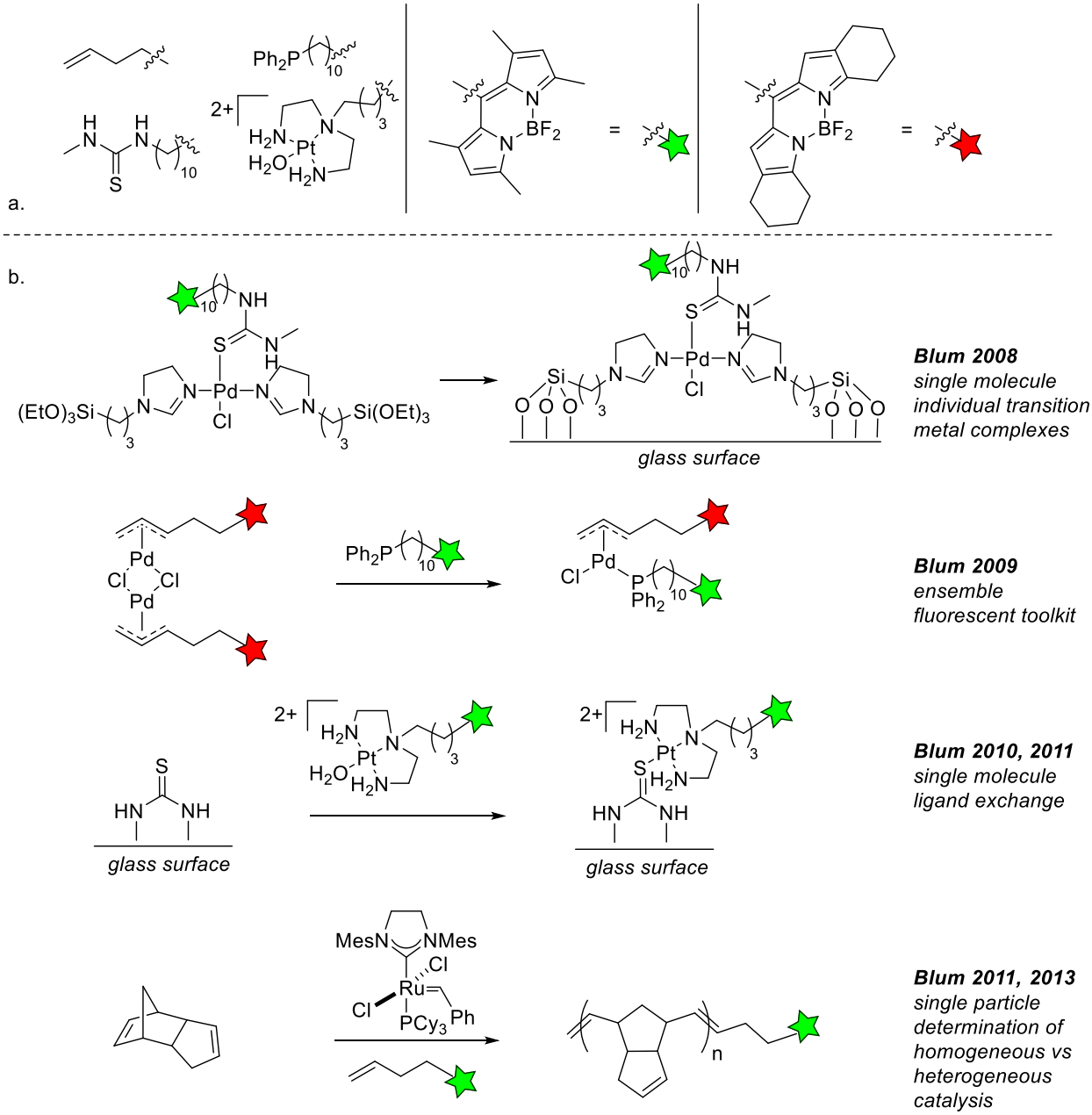

Figure 1.3. **a.** General structure of BODIPY fluorophores used in our group, indicating the previous examples of reactive groups connected via a spacer to the BODIPY fluorophore. **b.** General reaction of reactive groups of fluorophores with metals, visible through single molecule microscopy and fluorescence microscopy.

Palladium complexes were observed on glass surfaces bound to a spectator fluorophore.[25] These studies were the first example of using fluorescence microscopy to resolve individual transition metal complexes at the single molecule level, methodology that ultimately underpinned the detection of single turnovers at molecular catalysts. Using fluorescence resonance energy transfer (FRET), ligand exchange at platinum complexes could be monitored with greater sensitivity than with NMR spectroscopy.[26] These studies provided early investigations into variations in catalyst ligand exchange dynamics and detection of molecular complexes at low concentrations, which I later explored. They also provided our laboratory with expertise in the development and synthesis of fluorophore-tagged ligands for transition metal catalysts. Platinum complexes containing a spectator fluorophore were synthesized, and when these platinum complexes were exposed to thiourea immobilized on a glass coverslip, the resultant ligand exchange caused a bright green fluorescence signal indicating a single ligand exchange.[27–29] The importance of these studies was that single chemical reactions could be resolved at individual transition metal complexes for the first time, and further provided an insight into the reactivity distribution at these complexes. Such ability underpinned all future studies, because single reactions make up all steps in catalytic cycles. This fluorescence microscopy study further provided information on the rates of ligand exchange at the catalysts on siloxy surfaces similar to those used as catalyst supports. I used the knowledge from this project to design systems wherein single chemical reactions could be resolved at molecular catalysts, with spatiotemporal resolution of catalytic activity. The phase of polymerization using Grubbs' second generation catalyst was determined by using dicyclopentadiene and a spectator fluorophore.[30] This established the phase of polymerization by differentiating between homogeneous and heterogeneous catalysis as well as provided single-polymer particle data. The precipitation polymerization reaction was found to be

homogeneous, with no heterogeneous component. My research involved using single polymer particle data wherein the particles contained molecular catalysts within growing polymers. Finally, bulk polydicyclopentadiene formation was observed, starting from initiation, using a two-color fluorescence microscopy experiment.[31] The data revealed the mechanistic origin of polymer morphology through fluorescence microscopy. The studies I conducted explored local polymer morphology differences through chemical kinetics that ultimately described the variation in chain formation at precipitated polymers.

Each of the aforementioned studies in our group took advantage of the properties of the BODIPY fluorophore core (Figure 1.3), which possesses well-defined excitation-emission profiles ($\lambda_{max\ abs}$ = 493 nm; $\lambda_{max\ em}$ = 519 nm) and high quantum yields of up to ϕ = 0.99.[32] High quantum yields were required for successful observations of single fluorophores. Well-defined excitation-emission profiles enabled our group to design reactions in which the BODIPY unit served as a spectator fluorophore. In each spectator fluorophore, the reactive functional group is separated from the BODIPY unit by an organic spacer. Importantly, the BODIPY core is unreactive toward most transition metal complexes because it lacks accessible lone pairs and protic functional groups. Thus, the presence of the fluorophore does not cause side reactions that interfere with studying the native reactions of the system. Keeping the BODIPY unit separated from the reactive unit enabled the detection of the chemical reactions or ligand exchanges at the reactive groups. Such groups included terminal olefins, phosphines, thiourea derivatives, and metal catalysts. This approach enabled locations of single chemical reactions of BODIPY-tagged terminal olefins, phosphines, and thiourea derivatives with metal catalysts, and BODIPY-tagged metal catalysts with immobilized thiourea, to be identified without interfering with the properties of the BODIPY fluorophore. The data was collected in total internal reflection (TIRF) mode, meaning that

single-molecule detection was possible, and also that no fluorescence signals would be detected until a chemical reaction resulting in the probe being in the correct imaging plane for excitation by the laser.

Although the work from our group and others proved transformative for bringing single-molecule microscopy from a tool for biophysicists to a tool for organic chemists, molecular catalysts had not yet been observed in these systems. Due to the lack of available information on molecular catalyst activity,[33] studies were undertaken to understand and quantify the activity of molecular catalysts using microscopy techniques and BODIPY fluorophores (structures of fluorophores used in this thesis, Figure 1.4). Chapter 2 discusses the use of resin-supported Hoveyda-Grubbs' second generation catalyst to uncover hidden reactivity distributions at these catalysts despite uniform distributions and environments of the catalysts, observed through scanning electron microscopy (SEM), energy-dispersive X-ray spectroscopy (EDS), and optical microscopy.[34] Chapter 3 contains contributions I made to work initiated by Dr. Chao Feng on a research project involving the role of lithium chloride in solubilizing organozinc reagents.[35,36] Chapter 4 describes the first example of single turnover at molecular catalysts to give spatiotemporal resolution of catalytic activity.[37] In Chapter 5, time-variant polymerization kinetics of active molecular catalysts are described, showing subensemble differences at individual regions of catalytic activity where molecular catalysts are acting in concert.[38] These studies achieved the long-sought goal of determining the distribution of catalytic rates in a sample rather than the average rate, a challenge originally presented in Figure 1.1. Finally, Chapter 6 details a fluorescence microscopy/^{1}H NMR spectroscopy study on the kinetics of a polymerization reaction over nine orders of magnitude, describing what unique subensemble information is available and when it can be detected.[39]

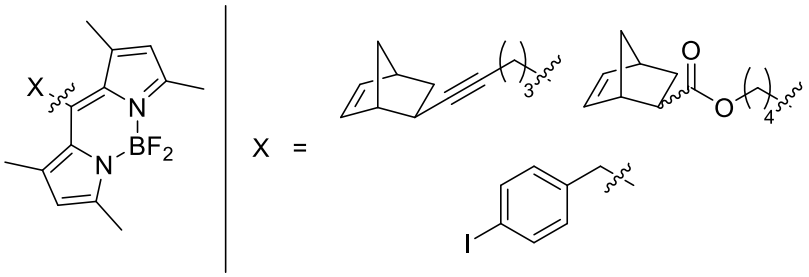

Figure 1.4. Structures of BODIPY fluorophores I developed, synthesized, and employed in the studies comprising this dissertation.

The value of these subensemble microscopy studies is to provide information that is unavailable through traditional ensemble characterization methods. Further, these studies refine the view of catalysis by revisiting catalytic cycles and chemical kinetics that chemists traditionally viewed as time-invariant and constant. Finally, they provide the first examples of single-turnover chemical information at molecular catalysts. In this system, although the molecular catalysts' activity can be quantified through fluorescence microscopy, they poorly fit the traditional concept of a "uniform" catalyst. This fundamental information will further refine the broader view of catalysis and potentially inform on designing catalysts meeting this "uniform" criterion.

References

(1) Kealy, T. J.; Pauson, P. L. *Nature* **1951**, *168*, 1039–1040.
(2) Hartwig, J. F. *Organotransition Metal Chemistry: From Bonding to Catalysis*. University Science Books: Sausalito, **2010**, pp. 547–549.
(3) Crabtree, R. H. *The Organometallic Chemistry of the Transition Metals*. Wiley: Hoboken, **2009**, p. 380.
(4. Sanford, M. S.; Love, J. A.; Grubbs, R. H. *J. Am. Chem. Soc.* **2001**, *123*, 6543–6554.
(5) Romero, P. E.; Piers, W. E. *J. Am. Chem. Soc.* **2005**, *127*, 5032–5033.
(6) Grabow, K.; Bentrup, U. *ACS Catal.* **2014**, *4*, 2153–2164.
(7) Buchmeiser, M. *Chem. Rev.* **2000**, *100*, 1565–1604.
(8) Fink, G.; Steinmetz, B.; Zechlin, J.; Przybyla, C.; Tesche, B. *Chem. Rev.* **2000**, *100*, 1377–1390.
(9) Weiss, S. *Science* **1999**, *283*, 1676–1683.
(10) Tian, H.; Fürstenberg, A.; Huber, T. *Chem. Rev.* **2017**, *117*, 186–245.
(11) Vale, R. D.; Funatsu, T.; Pierce, D. W.; Romberg, L.; Harada, Y.; Yanagida, T. *Nature* **1996**, *380*, 451–453.

(12) van Oijen, A. M.; Köhler, J.; Schmidt, J. *J. Opt. Soc. Am. A* **1999**, *16*, 909–915.
(13) Lakowicz, J. R. *Principles of Fluorescence Spectroscopy*. Springer: New York, **2006**.
(14) Roeffaers, M. B. J.; Sels, B. F.; Uji-i, H.; De Schryver, F. C.; Jacobs, P. A.; De Vos, D. E.; Hofkens, J. *Nature* **2006**, *439*, 572–575.
(15) Keshavarz, M.; Engelkamp, H.; Xu, J.; Braeken, E.; Otten, M. B. J.; Uji-i, H.; Schwartz, E.; Koepf, M.; Vananroye, A.; Vermant, J.; Nolte, R. J. M.; De Schryver, F.; Maan, J. C.; Hofkens, J.; Christianen, P. C. M.; Rowan, A. E. *ACS Nano* **2016**, *10*, 1434–1441.
(16) Chen, P.; Zhou, X.; Andoy, N. M.; Han, K.-S.; Choudhary, E.; Zou, N.; Chen, G.; Shen, H. *Chem. Soc. Rev.* **2014**, *43*, 1107–1117.
(17) Buurmans, I. L. C.; Weckhuysen, B. M. *Nat. Chem.* **2012**, *4*, 873–886.
(18) Ristanović, Z.; Kerssens, M. M.; Kubarev, A. V.; Hendriks, F. C.; Dedecker, P.; Hofkens, J.; Roeffaers, M. B. J.; Weckhuysen, B. M. *Angew. Chem. Int. Ed.* **2015**, *54*, 1836–1840.
(19) Ng, J. D.; Upadhyay, S. P.; Marquard, A. N.; Lupo, K. M.; Hinton, D. A.; Padilla, N. A.; Bates, D. M.; Goldsmith, R. H. *J. Am. Chem. Soc.* **2016**, *138*, 3876–3883.
(20) Tachikawa, T.; Majima, T. *Langmuir* **2012**, *28*, 8933–8943.
(21) Kubarev, A. V.; Janssen, K. P. F.; Roeffaers, M. B. J. *ChemCatChem* **2015**, *7*, 3646–3650.
(22) Rybina, A.; Lang, C.; Wirtz, M.; Gruβmayer, K.; Kurz, A.; Maier, F.; Schmitt, A.; Trapp, O.; Jung, G.; Herten, D.-P. *Angew. Chem. Int. Ed.* **2013**, *52*, 6322–6325.
(23) Hodgson, G. K.; Impellizzeri, S.; Scaiano, J. C. *Chem. Sci.* **2016**, *7*, 1314–1321.
(24) Nevskiy, O.; Sysoiev, D.; Opperman, A.; Huhn, T.; Wöll, D. *Angew. Chem. Int. Ed.* **2016**, *55*, 12698–12702.
(25) Canham, S. M.; Bass, J. Y.; Navarro, O.; Lim, S.-G.; Das, N.; Blum, S. A. *Organometallics* **2008**, *27*, 2172–2175.
(26) Lim, S.-G.; Blum, S. A. *Organometallics* **2009**, *28*, 4643–4645.
(27) Esfandiari, N. M.; Wang, Y.; Bass, J. Y.; Cornell, T. P.; Otte, D. A. L.; Cheng, M. H.; Hemminger, J. C.; Mcintire, T. M.; Mandelshtam, V. A.; Blum, S. A. *J. Am. Chem. Soc.* **2010**, *132*, 15167–15169.
(28) Esfandiari, N. M.; Wang, Y.; Mcintire, T. M.; Blum, S. A. *Organometallics* **2011**, *30*, 2901–2907.
(29) Esfandiari, N. M.; Wang, Y.; Bass, J. Y.; Blum, S. A. *Inorg. Chem.* **2011**, *50*, 9201–9203.
(30) Esfandiari, N. M.; Blum, S. A. *J. Am. Chem. Soc.* **2011**, *133*, 18145–18147.
(31) Hensle, E. M.; Blum, S. A. *J. Am. Chem. Soc.* **2013**, *135*, 12324–12328.
(32) Loudet, A.; Burgess, K. *Chem. Rev.* **2007**, *107*, 4891–4932.
(33) Cordes, T.; Blum, S. A. *Nat. Chem.* **2013**, *5*, 993–999.
(34) Easter, Q. T.; Trauschke, V.; Blum, S. A. *ACS Catal.* **2015**, *5*, 2290–2295.
(35) Feng, C.; Cunningham, D. W.; Easter, Q. T.; Blum, S. A. *J. Am. Chem. Soc.* **2016**, *138*, 11156–11159.
(36) Feng, C.; Easter, Q. T.; Blum, S. A. *Organometallics* **2017**, *36*, 2389–2396.
(37) Easter, Q. T.; Blum, S. A. *Angew. Chem. Int. Ed.* **2017**, *56*, 13772–13775.
(38) Easter, Q. T.; Blum, S. A. *Angew. Chem. Int. Ed.* **2018**, *57*, 1572–1575.
(39) Easter, Q. T.; Blum, S. A. *Submitted.*

Chapter 2

Catalyst Inefficiencies: Supported Ring-Opening Metathesis Polymerization Catalyst Yields Its Ensemble Rate from a Small Number of Molecular Active Sites

Abstract: A supported ruthenium catalyst misleadingly appears efficient on the basis of ensemble rate data. Nonaveraged single-particle microscopy studies described herein reveal a significant spatial reactivity distribution and a potential of increasing catalytic efficiency. These SEM, EDS, and optical microscopy studies of ring-opening metathesis polymerization establish a mechanism for this spatial distribution in which most of the molecular ruthenium centers are catalytically inactive. Further, the morphology of the growing polynorbornene arises from its synthesis at individual catalytically active regions. These results suggest an expanded role for single-particle microscopy in detecting spatial reactivity heterogeneity and mechanisms of polymer morphology formation even in such "large" systems of ~10^{15} immobilized molecular complexes, and in employing this detected heterogeneity to identify and implement specific methods for improving catalysts.

Introduction

Supported molecular catalysts have the advantage of facilitating separations and recyclability and limiting reactor fouling while in theory retaining some of the uniformity of the environment around the active metal center possessed by homogeneous molecular catalysis.[1] This uniformity of chemical environment has led to supported catalysts being termed "well-defined".[2] Nevertheless, immobilized catalysts can retain the original or display different reactivity[3] than

their otherwise analogous soluble molecular congeners due to differences in the local environment created by the support.[4] In part, the difficulty in characterizing these systems arises from the measurement challenge of characterizing the reactivity distributions that are obscured by ensemble averaging in traditional bulk measurements.

Herein, we describe optical and SEM microscopy studies of the interparticle and intraparticle reactivity heterogeneity of single resin beads[5–19] of a supported molecular Grubbs–Hoveyda-type ruthenium metathesis catalyst[2] during the polymerization of norbornene (eq 1). This supported catalyst system was chosen for studies due to its commercial availability and the industrial importance of polynorbornene produced by ruthenium-catalyzed ring-opening metathesis polymerization.[20] We also examine an ongoing mechanistic debate over the nature of the initiation distribution of the homogeneous version of this catalyst.[21–25] This distribution is obscured by ensemble averaging in traditional measurements, and in this vein, we highlight both the potential and the limitations of using single-particle techniques to address this question via supported versions of the catalyst.

Polymerization of norbornene by this catalyst is complete in about an hour at ambient temperature with a starting concentration of 1.4 M monomer and 0.08 mol % Ru. Given this short reaction time under mild conditions and low catalyst loading, the catalyst misleadingly appears efficient and already optimized when examined on this bulk reaction scale.

In this system, ruthenium carbene catalysts are supported on proprietary resin beads of approximately ~125 μm in diameter and, at 0.5 mmol/g loading of ruthenium, contain approximately 10^{15} potentially active "well-defined" molecular metal catalyst complexes per resin support bead. We show the surprising result that in these large systems of 10^{15} chemically well-

defined[2] complexes, the traditional ensemble-averaged reactivity data obscures an underlying tremendous distribution of catalytic reactivity[26–29] and potential for catalyst optimization.

The major findings of these studies are: 1) over 70% of the support beads are fully inactive to the detection limits of the methods and lack active sites that contribute significantly to the generation of the polynorbornene; 2) on the active beads, the majority of polymer forms at only a small number of locations; 3) the ruthenium is more evenly distributed across and within a catalyst bead than is distributed the catalytic reactivity; 4) polymer morphology is influenced by its growth from individual locations; and 5) this microscale, heterogeneous spatial reactivity suggests an untapped potential for increasing catalyst efficiency in this commercial system which was previously unrecognized. Tapping into this potential lead to improving the catalytic efficiency by mechanically pressing the beads to deform them prior to the reaction.

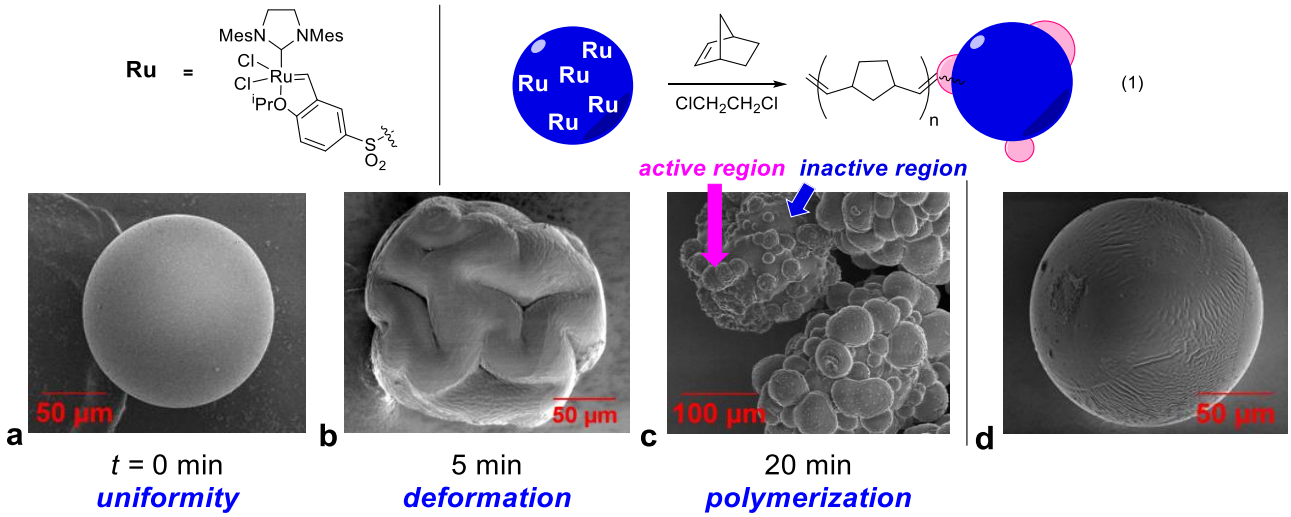

Figure 2.1. Distinct time regimes of reactivity, shown by SEM images obtained at different time points in the polymerization reaction. **a.** Uniformity. Image of the bead at 0 min showing the homogeneity of the bead surface. **b.** Deformation and dimpling of beads that was observed only in the presence of DCE and monomer. **c.** Polymerization from specific locations while others remained inactive; polymerization observed as hemispherical protrusions on the surface of the bead at 20 min as a moderately active bead (upper left) and a highly active bead (lower right). **d.** Control: representative catalyst bead in the presence of DCE solvent but in the absence of monomer does not show the dimpling or deformation that occurs in the presence of monomer.

a.

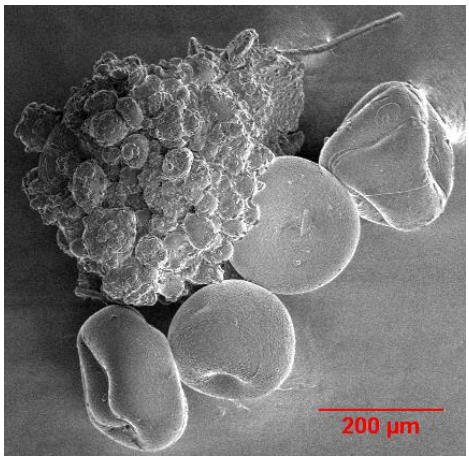

b.

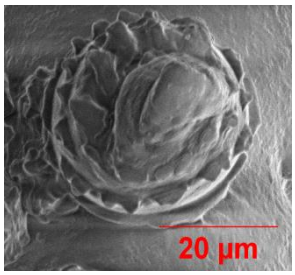

c.

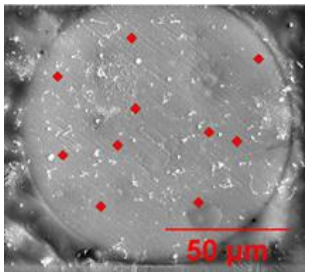

Figure 2.2. Distribution of catalytic activity and locations of catalysts. **a.** Most beads are catalytically inactive. Between multiple beads at t = 20 min; one bead is highly reactive, four show little or no reactivity. **b.** Nascent polymer morphology arises from individual active loci: on one bead, a single hemispherical polymer growth on one bead at high magnification, showing the regular repeating features on the micron and submicron scale. **c.** EDS measurements on the cross-sectioned interior of a catalyst bead; measurement locations in the bead interior are marked with red diamonds. Regions were selected at random and have no distinguishing features.

Results and Discussion

Scanning Electron Microscopy. SEM studies revealed three distinct catalytic time regimes. First, at t = 0 min, the resin-supported catalyst beads were uniformly sized, uniformly spherical, and nearly featureless (t = 0 min; Figure 2.1a). This SEM micrograph was obtained on a sample of the beads as received directly from the manufacturer without exposure to solvent or monomer.

The second regime was observed after addition of 1,2-dichloroethane (DCE), an efficient solvent for olefin metathesis,[30] and norbornene monomer initiated the polymerization reaction. This catalysis produced a divergence of the topology of the beads that was uniquely discernible by microscopy techniques; beads exposed to DCE in the absence of monomer did not show a similar topology divergence (Figure 2.1d). An initial deformation period consistent with an induction

period involving the support[31] lasted ~5 min, during which all of the beads dimpled and deformed as detected by SEM (Figure 2.1b). More than half of all beads stalled at this deformation stage and did not progress to the third stage.

The third regime occurred after 5 min, wherein only some of the dimpled beads then exhibited spatially heterogeneous catalytic polymerization reactivity (20 min; Figure 2.1c). During this time regime, polymerization occurred from less than half of the beads and only from specific loci on those active beads, demonstrating both interparticle and intraparticle reactivity heterogeneity. The polynorbornene produced in this system, confirmed by Raman spectroscopy,[32] was sufficiently insoluble to remain attached to the beads during the full course of the polymerization reaction; this polymer growth was observed as hemispherical protrusions on the surface of the beads by SEM. The location of the regions growing polynorbornene pinpointed the loci of catalytic reactivity.

Polymer Morphology. With the microscopy-generated understanding that the final bulk polymer was synthesized by a small number of active loci, we next examined the morphology of the polynorborene formed at these individual loci. The morphology of polymers influences their useful properties, such as optical transparency, conductivity, and thermal stability, and depends strongly on the nature of the catalyst support.[4] In most cases, the morphology of the nascent polymer displayed a defined repeating pattern (Figure 2.2b); this pattern was a spiral of well-defined ridges with repeating units of ~3 μm. This pattern spread to longer distances with increased polymer growth (e.g., compare Figure 2.1c of larger polymer with Figure 2.2b of smaller polymer).

Catalyst Activity. A major finding of this study is that more than half of all the resin support beads are inactive and do not contribute significantly to the growth of polymer; these are the inactive beads that stalled after the deformation time regime. Specifically, at 20 min, some beads

showed high activity, visible as a large number of individual polymerization sites, while others showed lower activity (both a lower number of active sites and smaller growth at each site) or no activity (Figure 2.2a). All beads showed deformation, however. A representative sample of beads showing this interparticle heterogeneity is shown in Figure 2.2a, wherein one highly active bead is covered in polymer originating from multiple reactive loci, but four neighboring beads show little to no polymerization reactivity but do show the signature deformation that occurs in the presence of both monomer and solvent.

We considered three mechanistic explanations for this spatially heterogeneous polymerization activity (Figure 2.3): 1) The listed 0.5 mmol/g ruthenium loading of the commercial resin was erroneous; a much lower actual loading could account for the small number of active sites. 2) The catalyst was concentrated in a small number of locations within the support; this could explain why polymerization occurred at a countable number of locations. 3) A small number of ruthenium centers displayed high activity, while the majority displayed no activity or activity too low to detect by SEM.

Energy-dispersive X-ray Spectroscopy. Single-particle microscopy techniques permitted differentiation between these three mechanistic possibilities. Examination of a flat, cross-sectioned slice of the interior of a catalyst bead with energy-dispersive X-ray spectroscopy (EDS) at multiple random measurement locations established that the ruthenium was uniformly loaded throughout the beads rather than localized at specific sites. With 10 measured locations, the concentration of Ru was 5.3 ± 0.3 weight % (Figure 2.2c). This small standard deviation and average loading are both consistent with the listed loading of the commercial sample and with uniform loading at each measurement location. Thus, the ruthenium was distributed more uniformly throughout the support than was the catalytic reactivity.

PIXE elemental analysis of an ensemble of beads indicated a Ru concentration of 2.36 ± 0.02 weight %. The origin of the discrepancy between ruthenium loadings measured by PIXE and by EDS is unclear; however, both measurements indicate a similar order of magnitude for the ruthenium loading.

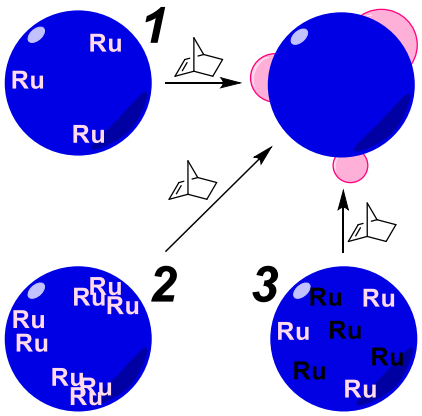

Figure 2.3. Three mechanistic possibilities for spatially nonuniform polymerization. (1) The manufacturer's stated loading was higher than the actual loading of catalyst throughout the support. (2) The catalyst was loaded only at specific sites throughout the support rather than uniformly. (3) The catalyst was uniformly loaded throughout the support, but only specific sites were active during catalysis.

This data revealed that the ensemble rate of polymerization came from a small number of active ruthenium sites while the majority of ruthenium did not contribute significantly to the measured ensemble rate (mechanistic option 3, Figure 2.3). These active sites could be individual ruthenium complexes, or they could be clusters of neighboring sites that become mutually activated as the growing polymer deforms the material and exposes additional ruthenium complexes to monomer, similar to how the hydraulic force of the growing polypropylene in the polymerization of propene by silica-supported metallocene catalysts cracks the rigid silica support and exposes neighboring catalyst centers to monomer and thus generates additional neighboring active sites.[1]

We also considered the possibility that the catalyst itself could be poorly initiating chemically, leading to catalysis originating from a small number of complexes. This suggestion

has been raised as part of a long-standing debate on distribution of initiation rates for Grubbs–Hoveyda catalysts,[21–25] the distribution of which is obscured by traditional ensemble measurements. While providing an early picture of nonensemble-averaged reactivity in this system, the current data remains insufficient to identify if the overall distribution is purely from a physical effect of the support or if it also includes this debated chemical component. The primary measurement challenge that remains in this supported system is the deconvolution of the physical and chemical effects. The nonzero contribution of physical effects were confirmed through later experiments that probed the effect mechanical bead deformation on reaction yields (vida supra).

In Operando Microscopy. Although SEM provided exceptional spatial resolution, it required removal of samples from the reaction vessel and subsequent drying, raising the possibility of artifacts. We therefore next examined if the spatial reactivity heterogeneity was also present under reaction conditions in the presence of solvent and monomer by using in operando optical microscopy. This in operando method had the advantage of following the behavior of the catalyst system through time without removal of the sample from the reaction vessel, albeit with the disadvantage of decreased spatial resolution compared to SEM.

In this in operando experiment, the catalyst beads were loaded into a modified reaction vial with a glass coverslip bottom, permitting imaging of the reaction by transmitted light microscopy. Toluene, a reported solvent[25] for efficient olefin metathesis, was selected to allow for easier optical imaging, and also to examine if the catalytic spatial reactivity heterogeneity was present in this second solvent as well.

Images were obtained first at $t = 0$ min and then continuously at video rate upon addition of solvent and monomer. Polymer growing in real time on individual beads could be detected as light grey translucent regions growing on dark black beads. Figure 2.4 shows a representative

image of a bead obtained with optical microscopy at t = 10 min. The polymer growth was not spherically uniform on these beads, but instead occurred at specific positions on the surface. The spatial reactivity distribution observed during in operando experiments therefore mirrored that observed previously by SEM.

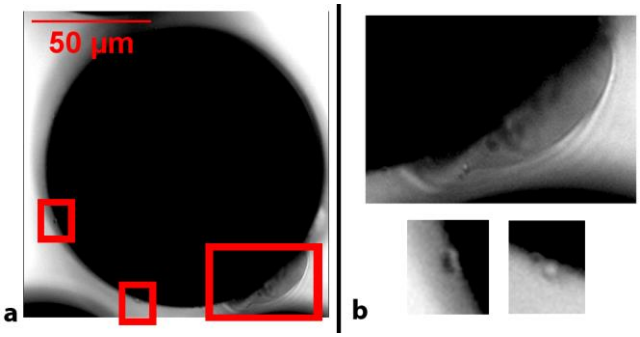

Figure 2.4. Representative in operando optical microscopy images of distribution of catalytic activity. **a.** Image showing highly active and less active polymerization regions on the same black resin bead at t = 10 min. Polymer is visible as light grey translucent regions. **b.** Three expansions corresponding to the three red boxed-in regions of the image on the left.

Furthermore, over half of the beads did not show detectable polymer growth at 20 min by optical microscopy. Specifically, as measured over nine experiments with a total set size of $13\bar{0}$ beads (averaging 14.4 beads per observation), 28 ± 8% of the beads showed observable polymerization catalysis at t = 20 min. The remainder of the beads, which appeared as black spheres without the visible growth regions (see Experimental for example; Figure 2.7), correspond to the less active (or inactive) beads detected by SEM (Figure 2.2a). Thus, the interparticle reactivity heterogeneity observed in DCE also was retained in toluene and under reaction conditions.

Concrete Suggestion for Improved Catalyst Efficiency. The previously discussed EDS data revealed an indiscriminate manufacturing process wherein the molecular ruthenium complexes were located uniformly throughout the support bead rather than only on its surface. This location data suggested that the challenge is to increase the number of sites becoming active in order to

increase the catalytic efficiency, rather than increase the rate of polymerization from already active sites.

We hypothesized that mechanically pressing the catalyst beads prior to the catalytic reaction could result in faster entry into the third time regime of polymerization by "pre-deforming" the beads such that the 5 min induction/deformation period would be diminished; this process could generate a greater surface area which would expose more catalytic centers to monomer because the ruthenium complexes were evenly distributed throughout the beads.

Mechanical pressing created fissures in the beads, but otherwise left the beads mostly intact (Figure 2.5). These pressed beads displayed substantially higher catalytic efficiency in ensemble studies (Figure 2.6), as measured by polymer conversion per unit of time via ^{1}H NMR spectroscopy. The comparison at 5 min shows a 5x increase in polynorbornene conversion (11 ± 1% unpressed, 51 ± 16% pressed), and at 10 min shows a 3x increase (27 ± 4% unpressed, 90 ± 2% pressed). These results demonstrate a strategy for successful catalyst improvement that retains the original desired properties/size range of the commercial supported catalyst; this strategy was derived from knowledge of the stages of the reaction and of the location of the ruthenium obtained by single-particle microscopy studies.

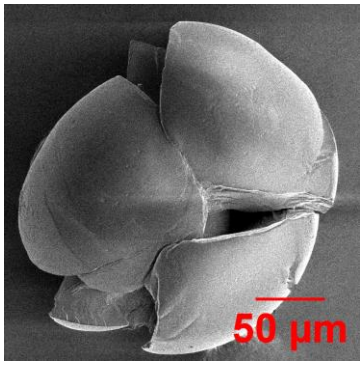

Figure 2.5. SEM micrograph of a mechanically pressed bead. Fissures in support are evident; support retains similar size and does not fragment into significantly smaller pieces.

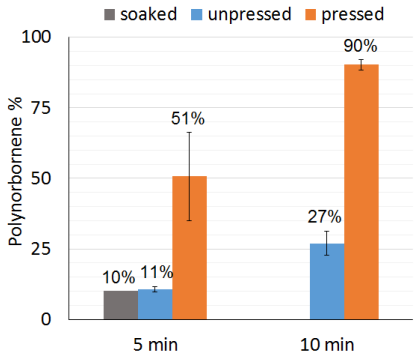

Figure 2.6. ^{1}H NMR spectroscopy of beads giving polynorbornene yield. Increase in polynorbornene yield with pressed support beads (orange) compared to unpressed support beads as received from manufacturer (blue) measured via ^{1}H NMR spectroscopy relative to an internal standard. Control reaction with presoaking shows no similar increase (grey), consistent with heterogeneous catalysis rather than homogeneous catalysis by leached ruthenium.

Control Reactions. In order to probe if the active catalysts in this system were, indeed, heterogeneous supported molecular ruthenium complexes, or if they were homogenous ruthenium complexes that had leached into solution, a series of control experiments were performed.

A first control experiment with presoaking the intact support was performed. Specifically, the support was presoaked for 20 min in the reaction solvent in the absence of norbornene. Then, norbornene was added. This system generated the same conversion to polynorbornene at 5 min (10%; grey bar, Figure 2.6) as was generated without the presoak (11 ± 1%, blue bar). Thus, the presoak, which would provide additional time for leaching, did not result in additional conversion to polymer. When taken together with the observation of polymers attached to the support by both SEM and optical microscopy, this set of experiments is consistent with the catalytic activity coming from the supported complex rather than leached molecular species in solution.

Further, this first control experiment established that the swelling of resin in DCE was insufficient to increase the generation of polynorbornene. These beads that soaked in solvent for 20 min in the absence of norbornene showed swelling as detected by a larger bead diameter (but no deformation or dimpling) by SEM (Figure 2.1d). We considered the possibility that this swelling would be an alternative route to increasing the effective surface area of this supported

catalyst; however, in this system no such rate increase was correlated to the swelling, and the presoaked beads generated polynorbornene in similar conversion to beads that were not presoaked. Thus, in this system, mechanical pressing provided the specific successful strategy for increasing the catalytic efficiency.

A second control experiment wherein the soaking solvent was removed from the beads via pipet after 10 min of soaking was examined. This process produced a sample of clear soaking liquid without any visible beads; however, pieces of supported catalyst smaller than visible detection may have remained, especially in the pressed-bead system (although most pressed beads retained similar sizes). After separation of the soaking solvent and the beads, the soaking solvent was added to norbornene monomer. The same experiment was conducted using the pressed beads, in order to probe if pressing the beads may have resulted in enhanced ruthenium leaching into solution that was responsible for the increase in conversion observed upon pressing. The ^{1}H NMR spectroscopy yields of polynorbornene using the intact and pressed bead soaking solvents were 2.1 ± 0.3% and 5.0 ± 0.6% respectively. These data indicated an upper limit to a homogeneous catalysis component of 2% out of the total intact bead 11% polymer yield and 5% out of the total pressed bead polymer yield of 51%.

Conclusion

The observations from SEM, EDS, and optical microscopy highlight the starkly contrasting pictures of reactivity available from ensemble averaged data and from single-bead nonaveraged data in this catalytic system: The ensemble averaged data gives the appearance of an efficient catalyst system that generates polymer in full conversion in about an hour at ambient temperature, whereas in contrast, the single-bead, nonaveraged data available from microscopy techniques

provides evidence of an inefficient catalyst system wherein the majority of molecular ruthenium complexes do not contribute to overall catalytic reactivity. This revised picture of reactivity indicates a substantial potential for increased catalytic efficiency in this commercial system, which was partially tapped by pre-deforming the beads. Similar potentials for increased catalytic efficiency are likely also present in other catalytic systems that are currently described by ensemble data.[5]

Experimental

I. General Information

All reagents and solvents were used as received from their commercial suppliers. Norbornene (Acros Chemicals) was used as the monomer for all experiments. Spectrophotometric grade toluene (Alfa Aesar) was used for microscopy studies, and reagent grade 1,2-dichloroethane (Alfa Aesar) was used for scanning electron microscopy (SEM) studies. The resin-supported ruthenium catalyst was purchased from Strem Chemicals, Inc. and used as received. Mesitylene (Alfa Aesar) was used as an internal standard for the NMR measurements. Ultra-pure water with >18 MΩ resistance and total organic content of <5 ppb was obtained from a Milli-Q Gradient A10 water purifier (Millipore, Billerica, MA) using a Q-Gard 2 purification pack and a Quantum EX Ultrapure Organex cartridge.

II. Bench-Scale Experiments

Experiment 1. Solvent screening for ambient light microscopy. The ruthenium catalyst (2.0 mg, 1.0×10^{-3} mmol Ru, calculated from the stated loading of 0.5 mmol Ru/g support) was added to 0.5 mL of different solvents, including dichloromethane, 1,2-dichloroethane (DCE),

chloroform, toluene, and heptane. Due to the microscope setup, toluene was chosen because the beads sank to the bottom for ease in measurement.

Experiment 2. Polymerization of norbornene for SEM images. Norbornene (15.0 mg, 0.159 mmol) dissolved in 0.5 mL DCE was added to the supported ruthenium catalyst (1.4 mg, 7.0×10^{-4} mmol Ru). This mixture was stirred. Catalyst beads were removed from the original solution at intervals of t = 5, 10, and 20 min, and the removed beads were washed in a separate vial containing DCE before SEM characterization.

Experiment 3. Generation of bulk-scale polynorbornene for characterization. Norbornene (160. mg, 1.70 mmol) dissolved in 0.5 mL DCE was added to the supported ruthenium catalyst (2.0 mg, 1.0×10^{-3} mmol Ru). The mixture was stirred. Reaction occurred for 15 min, resulting in bulk polymer production. In order to avoid potential contamination by the resin support material, a sample of product polymer was cut off the resin with a spatula. This slice of product polymer was analyzed by Raman spectroscopy.

Experiment 4. Polymerization of norbornene for quantitative NMR measurements. The samples were prepared as described below. Conversions are reported relative to mesitylene internal standard, calculated based on the amount of residual norbornene. The ^{1}H NMR spectroscopy signals of mesitylene at 6.79 ppm and norbornene at 5.99 ppm were used for integration from single-scan ^{1}H NMR spectra.

a) *Beads as received from manufacturer.* Norbornene (67.6 mg, 0.718 mmol) and mesitylene (45.0 µL, 0.324 mmol) were dissolved in 0.5 mL DCE-d_4 and added to a glass reaction vial containing the supported ruthenium catalyst (1.1 mg, 5.5×10^{-4} mmol Ru) and a stir bar. The mixture was stirred. After t = 5 min or t = 10 min, 0.1 mL of the solution was taken out and added

to 0.2 mL of $CDCl_3$, followed by analysis by ^1H NMR spectroscopy. This process was repeated in triplicate. The conversion of polynorbornene was 11 ± 1% after 5 min of reaction and 27 ± 4% after 10 min of reaction.

b) *Pressed beads.* The supported ruthenium catalyst was pressed with a hammer for 5 min. Norbornene (67.6 mg, 0.718 mmol) and mesitylene (45.0 µL, 0.324 mmol) were dissolved in 0.5 mL DCE-d_4 and added to a glass reaction vial containing the supported ruthenium catalyst (1.1 mg, 5.5×10^{-4} mmol Ru) and a stir bar. After t = 5 min or t = 10 min, 0.1 mL of the solution was taken out and added to 0.2 mL of $CDCl_3$ followed by analysis by ^1H NMR spectroscopy. This process was repeated in triplicate. The calculated polynorbornene conversion was 51 ± 16% after 5 min of reaction and 90 ± 2% after 10 min of reaction.

c) *Soaked beads.* DCE-d_4 (0.2 mL) was added to a glass reaction vial containing the supported ruthenium catalyst (1.1 mg, 5.5×10^{-4} mmol Ru) and a stir bar. The beads were allowed to soak for 20 min. A solution of norbornene (67.6 mg, 0.718 mmol) and mesitylene (45.0 µL, 0.324 mmol) in 0.3 mL DCE-d_4 then was added to the catalyst. After 5 min of stirring, 0.1 mL of the solution was taken out and added to 0.2 mL of $CDCl_3$ followed by analysis by ^1H NMR spectroscopy. The yield of polynorbornene after 5 min of reaction was 10%. This conversion was within one standard deviation of nonsoaked beads.

III. Construction of Reaction Cells for Microscopy

Glass coverslips (25 × 25 mm, No. 1.5, VWR Scientific) with a thickness of 0.17 mm were cleaned by sonication in 20 mL of a 0.6% solution of Hellmanex Detergent (Fisher Chemical) in MilliQ water for 60 min and then rinsed sequentially with MilliQ water and spectrophotometric grade ethanol six times. The rinsed coverslips were dried with compressed air, then placed on

aluminum foil and further dried in an oven at 115 °C for 10 to 20 min. Coverslips were either stored covered or used immediately after drying.

Hollow glass cylinders were formed by cutting the ends from glass reaction vials (Short Form Style, VWR Scientific). The cylinders were rinsed thoroughly with MilliQ water and spectrophotometric grade ethanol and dried in an oven at 115 °C for 20 to 30 min before use.

To assemble the reaction cells, the cleaned and dried hollow vials were attached to the cleaned coverslips by applying epoxy (Devcon) to the outside base of the tubes, then covered and stored overnight before use.

IV. Microscopy and General Parameters

Imaging was performed with an inverted microscope (IX71, Olympus Corporation) and an oil-immersion objective with a 1.45 numerical aperture. Samples were imaged with a C9100-13 CCD camera (Hamamatsu Photonics). The CCD chip was a back-thinned electron multiplication type with an effective 512×512 array of pixels. Focus was changed with a *z*-axis controller (MS-2000, Applied Scientific Instruments, Inc.). The SlideBook software (Intelligent Imaging) was set to acquire continuous images with 100 ms per frame. Images were viewed in ImageJ (NIH, available at http://rsbweb.nih.gov/ij/).

Scanning electron microscopy (SEM) was accomplished by using a FEI Quanta 3D FEG Dual Beam (FEI Company) in the Laboratory for Electron and X-ray Instrumentation (LEXI) at the University of California, Irvine. Samples were imaged on carbon tape at 1.0 kV energy, 43 pA current, and pressures lower than 8×10^{-5} mbar using the xTm software (FEI Company) with XJ

Charts (XJ Technologies). Images were collected at varying magnifications with a 1024×943 pixel resolution.

Energy-dispersive X-ray spectroscopy (EDS) was performed on the FEI Quanta 3D using the Oxford EDS Detector for Quanta 3D (Oxford Instruments) in the LEXI facilities. Samples were imaged as prepared with 30.0 kV energy and 43 pA current at pressures below 8×10^{-5} mbar. Samples were viewed using the xTm software, and after images were selected, data was collected and interpreted using the INCA software (v. 4.15, Oxford Instruments Analytical Limited).

V. Image Acquisition of Norbornene Polymerization via In-Operando Microscopy

Norbornene (10.0 mg, 0.106 mmol) was dissolved in 0.5 mL toluene and added to the supported ruthenium catalyst (1.2 mg, 6.0×10^{-4} mmol Ru). This sample was placed into a premade reaction vial (Section III) and then imaged (Section IV). The light source for these experiments was the ambient room light. Images were taken at t = 5, 10, and 20 min; beyond 20 min, observations were complicated by extensive polymer growth. Beads that exhibited translucent polymer growth were counted as "active" at a certain time point. Beads that did not exhibit translucent growth were counted as "inactive."

Table 2.1. Calculated data for active and inactive beads using in operando microscopy.

	Active Beads	Total Beads	% Active
	4	13	31%
	4	16	25%
	5	16	31%
	4	11	36%
	7	17	41%
	4	14	29%
	3	15	20%
	3	14	21%
	2	14	14%
Average	4	14.4	28%
Standard Deviation			7.9

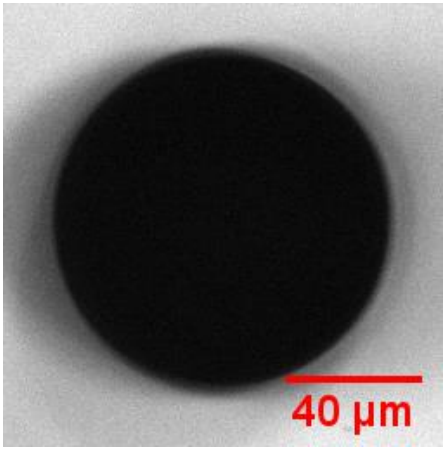

Figure 2.7. In operando microscopy image of an inactive catalyst bead at t = 20 min.

VI. Elemental Data: Sample Preparation, Full Spectrum Map, Kα Truncated Region, and Average Weight, Atomic Percentages and PIXE Data

A sample of the supported ruthenium catalyst was added to an epoxy resin, which was left to harden overnight. The resin was subjected to polishing, which exposed the interior of the beads. The sample was sputter-coated with iridium metal to provide conductivity during EDS measurements.

The elemental composition was examined by EDS in the interior of one catalyst bead at 10 different sites (Table 2.2). The primary diagnostic peak for ruthenium was observed at Kα = 19.15 kV, in accordance with the literature report.[33]

Proton-induced x-ray emission (PIXE) was also obtained from Elemental Analysis, Inc., which also revealed the presence of Ru at the previous Kα line.

Table 2.2. Weight and atomic percent of atoms in the supported ruthenium catalyst by EDS and by PIXE.

Element	**Weight % by EDS**	**Atomic % by EDS**	**Weight % by PIXE**
Carbon	66.54 ± 0.92	79.54 ± 0.60	75.17
Oxygen	16.80 ± 0.48	15.07 ± 0.47	17.88
Phosphorus	1.11 ± 0.05	0.52 ± 0.03	0.097 ± 0.003
Sulfur	3.67 ± 0.25	1.64 ± 0.12	1.84 ± 0.02
Chlorine	5.54 ± 0.18	2.24 ± 0.09	2.15 ± 0.03
Copper	1.02 ± 0.08	0.23 ± 0.02	0.508 ± 0.005
Ruthenium	5.34 ± 0.34	0.76 ± 0.05	2.36 ± 0.02

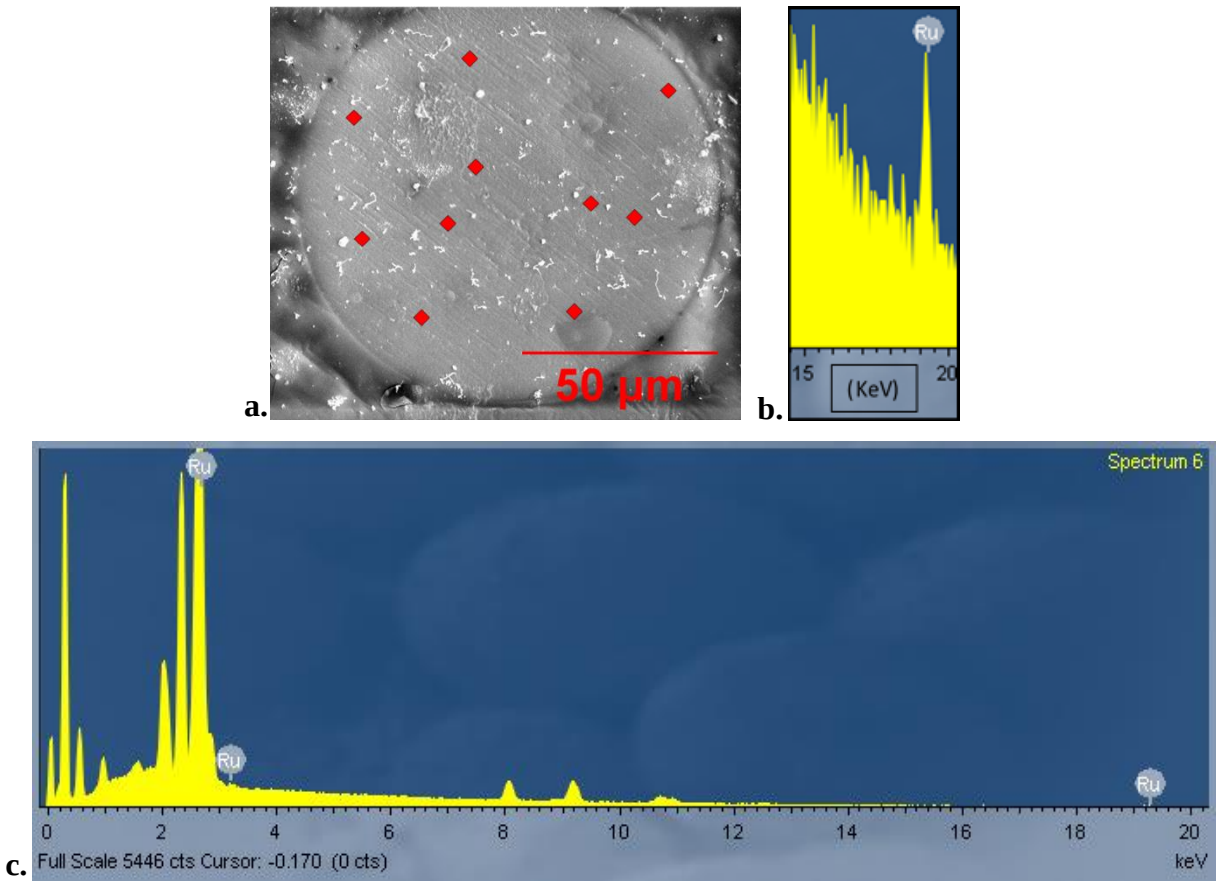

Figure 2.8. EDS data of catalyst beads. **a.** The interior of the supported ruthenium catalyst with marked regions where EDS data was taken. **b.** The truncated region of the EDS spectrum of the supported ruthenium catalyst to show the Kα peak of ruthenium. **c**. The full EDS spectrum of the supported ruthenium catalyst.

VII. Microscopy Control Experiments for Assignment of Polynorbornene Growth from the Supported Ruthenium Catalyst

A series of control experiments were performed to determine if the growth coming from the beads was polynorbornene. These experiments were consistent with the assignment of the growth from the beads as polynorbornene.

Control Experiment 1: *Metathesis catalyst observed by optical microscopy in absence of norbornene monomer*. Toluene (0.5 mL) was added to the supported ruthenium catalyst (1.5 mg, 7.5×10^{-4} mmol Ru) in the absence of norbornene. No polymer was observed coming from the

catalyst beads with in operando microscopy, nor did the beads deform in any way to generate the previous observations.

Control Experiment 2: Solution of norbornene in toluene observed by optical microscopy in absence of supported ruthenium catalyst. Norbornene (20.5 mg, 0.218 mmol) was dissolved in 0.5 mL toluene in the absence of the supported ruthenium catalyst. No polymer was observed being generated in solution with in operando microscopy, nor was any monomer observed precipitating out of solution.

Control Experiment 3: SEM of supported ruthenium catalyst as received. Beads were observed at t = 0 min without placing the beads in any solvent or any solution containing norbornene. No rosettes or other surface deformations were observed on the surface of the beads; rather, the surface looked essentially featureless.

Control Experiment 4: SEM of solid norbornene. A sample of norbornene observed by SEM did not have similar topology or the same rosette pattern (i.e. Figure 2.1c) seen on beads with polymer.

Control Experiment 5: NMR yield using presoak solution from intact beads. The supported ruthenium catalyst (1.1 mg, 5.5×10^{-4} mmol Ru) was soaked in 0.25 mL DCE-d_4 for 10 min. Norbornene (67.4 mg, 0.716 mmol) and mesitylene (45.0 µL, 0.324 mmol) were dissolved in 0.25 mL DCE-d_4 and added to a glass reaction vial with a stir bar. A syringe was used to remove 0.1 mL of solution used to presoak the supported ruthenium catalyst, ensuring removal of all visible catalyst beads, which was added to the solution containing norbornene and mesitylene. The solution was stirred. After t = 5 min, 0.1 mL of the solution was taken out and added to 0.2 mL of $CDCl_3$ followed by analysis by ^{1}H NMR spectroscopy. This process was repeated in triplicate. The calculated polynorbornene conversion was 2.0 ± 0.3% after 5 min of reaction.

Control Experiment 6: NMR yield using presoak solution from pressed beads. The supported ruthenium catalyst was pressed with a hammer for 5 min. The catalyst (1.0 mg, 5.0×10^{-4} mmol Ru) was soaked in 0.25 mL DCE-d_4 for 10 min. Norbornene (67.5 mg, 0.717 mmol) and mesitylene (45.0 μL, 0.324 mmol) were dissolved in 0.25 mL DCE-d_4 and added to a glass reaction vial with a stir bar. A syringe was used to remove 0.1 mL of solution used to presoak the supported ruthenium catalyst, ensuring removal of all visible pieces of catalyst, which was added to the solution containing norbornene and mesitylene. The solution was stirred. After t = 5 min, 0.1 mL of the solution was taken out and added to 0.2 mL of $CDCl_3$ followed by analysis by ^1H NMR spectroscopy. This process was repeated in triplicate. The calculated polynorbornene conversion was 5.0 ± 0.6% after 5 min of reaction.

VIII. Characterization of Polymerization Products

Raman spectroscopy data was collected on an InVivo Renishaw Raman Microscope, courtesy of the Laser Spectroscopy Facility at the University of California, Irvine. After polymer was grown in bulk for 15 min (Section II), the bead was removed from solution. A beam of wavelength 532 nm was focused on the edge of the unwashed polymer attached to the bead, to avoid contamination with the resin interior. The diagnostic C=C stretch of polynorbornene[32] (Figure 2.9) came in at 1664 cm^{-1} in contrast to that of norbornene[32] at 1550 cm^{-1}.

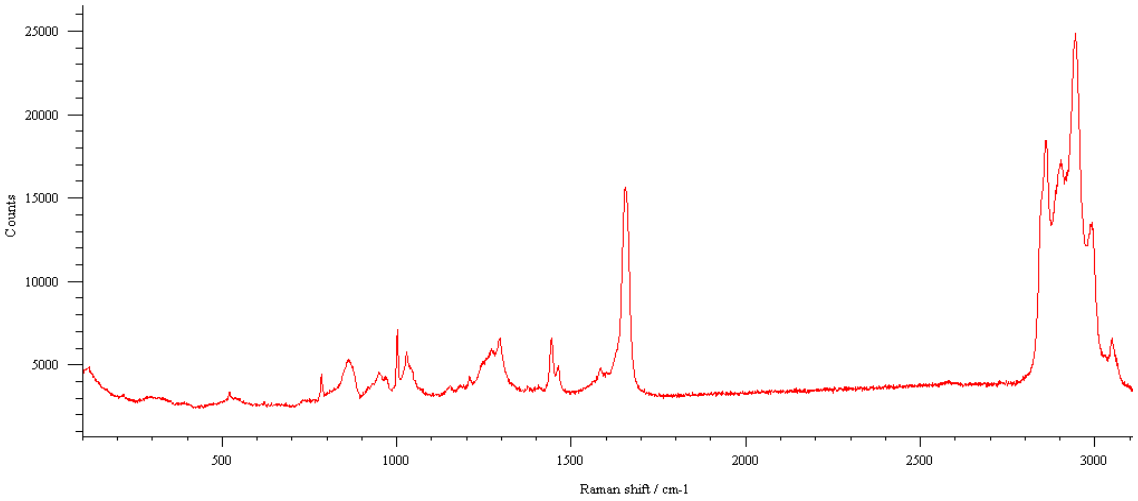

Figure 2.9. Raman spectrum of polynorbornene. Data obtained from reaction with catalyst beads at t = 20 min.

IX. Large-Scale Images from Main Text

The images from the main text (Figure 2.1a-c) are placed in this section for reference, to provide easier views of the hemispherical protrusions and the surface of the beads not participating in polymerization.

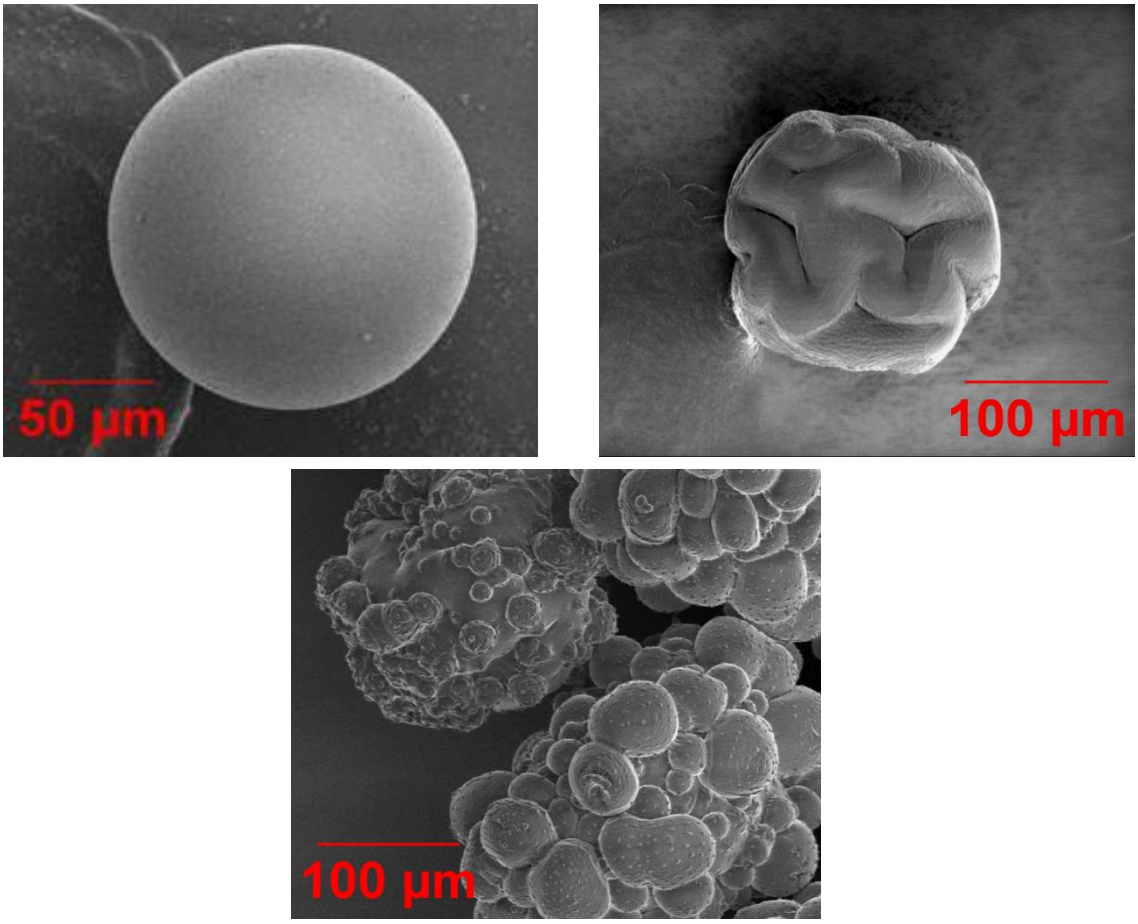

Figure 2.10. Large-scale Figure 2.1.a-c.

References

(1) Fink, G.; Steinmetz, B.; Zechlin, J.; Przybyla, C.; Tesche, B. *Chem. Rev.* **2000**, *100*, 1377–1390.
(2) Buchmeiser, M. R. *Chem. Rev.* **2009**, *109*, 303–321.
(3) Parlett, C. M. A.; Bruce, D. W.; Hondow, N. S.; Lee, A. F.; Wilson, K. *ACS Catal.* **2011**, *1*, 636–640.
(4) Goretzki, R.; Fink, G.; Tesche, B.; Steinmetz, B.; Rieger, R.; Uzick, W. *J. Polym. Sci., Part A: Polym. Chem.* **1999**, *37*, 677–682.
(5) Buurmans, I. L. C.; Weckhuysen, B. M. *Nat. Chem.* **2012**, *4*, 873–886.
(6) De Smit, E.; Swart, I.; Creemer, J. F.; Karunakaran, C.; Bertwistel, D.; Zandbergen, H. W.; de Groot, F. M. F.; Weckhuysen, B. M. *Angew. Chem. Int. Ed.* **2009**, *48*, 3632–3636.
(7) Kox, M. H. F.; Stavitski, E.; Groen, J. C.; Pérez-Ramíre, J.; Kapteijn, F.; Weckhuysen, B. M. *Chem. Eur. J.* **2008**, *14*, 1718–1725.
(8) Roeffaers, M. B. J.; Sels, B. F.; Uji-i, H.; De Schryver, F. C.; Jacobs, P. A.; De Vos, D. E.; Hofkens, J. *Nature* **2006**, *439*, 572–575.
(9) De Cremer, G.; Bartholomeeusen, E.; Pescarmona, P. P.; Lin, K.; De Vos, D. E.; Hofkens, J.; Roeffaers, M. B. J.; Sels, B. F. *Catal. Today* **2010**, *157*, 236–242.

(10) Fast, A.; Esfandiari, N. M.; Blum, S. A. *ACS Catal.* **2013**, *3*, 2150–2153.
(11) Hensle, E. M.; Blum, S. A. *J. Am. Chem. Soc.* **2013**, *135*, 12324–12328.
(12) Esfandiari, N. M.; Blum, S. A. *J. Am. Chem. Soc.* **2011**, *133*, 18145–18147.
(13) Cordes, T.; Blum, S. A. *Nat. Chem.* **2013**, *5*, 993–999.
(14) Blum, S. A. *Phys. Chem. Chem. Phys.* **2014**, *16*, 16333–16339.
(15) Esfandiari, N. M.; Wang, Y.; Bass, J. Y.; Blum. S. A. *Inorg. Chem.* **2011**, *50*, 9201–9203.
(16) Zhou, X.; Choudhary, E.; Andoy, N. M.; Zou, N.; Chen, P. *ACS Catal.* **2013**, *3*, 1448–1453.
(17) Andoy, N. M.; Zhou, X.; Choudhary, E.; Shen, H.; Chen, P. *J. Am. Chem. Soc.* **2013**, *135*, 1845–1852.
(18) Chen, P.; Zhou, X.; Andoy, N. M.; Han, K.-S.; Choudhary, E.; Zou, N.; Chen, G.; Shen, H. *Chem. Soc. Rev.* **2014**, *43*, 1107–1117.
(19) Flier, B. M. I.; Baier, M.; Huber, J.; Müllen, K.; Mecking, S.; Zumbusch, A.; Wöll, D. *Phys. Chem. Chem. Phys.* **2011**, *13*, 1770–1775.
(20) Ohm, R.; Stein, C. In *Encyclopedia of Chemical Technology*, 3rd ed.; Grayson, M., Ed.; Wiley-Interscience: New York, **1982**.
(21) Vorfalt, T.; Wannowius, K.-J.; Thiel, V.; Plenio, H. *Chem. Eur. J.* **2010**, *16*, 12312–12315.
(22) Gessler, S.; Randl, S.; Blechert, S. *Tetrahedron Lett.* **2000**, *41*, 9973–9976.
(23) Thiel, V.; Hendann, M.; Wannowius, K.-J.; Plenio, H. *J. Am. Chem. Soc.* **2012**, *134*, 1104–1114.
(24) Núñez-Zarur, F.; Solans-Monfort, X.; Pleixats, R.; Rodríguez-Santiago, L.; Sodupe, M. *Chem. Eur. J.* **2013**, *19*, 14553–14565.
(25) Bates, J. M.; Lummiss, J. A. M.; Bailey, G. A.; Fogg, D. E. *ACS Catal.* **2014**, *4*, 2387–2394.
(26) For examples of catalytic reactivity distributions attributed to physical/diffusion heterogeneities, see: refs. 5 and 7. For examples of catalytic reactivity distributions attributed to different chemical species/chemical environments, see: refs. 16, 17, 22, 23, and 24.
(27) Zhong, L.; Lee, M.-Y.; Liu, Z.; Wanglee, Y.-J.; Lui, B.; Scott, S. L. *J. Catal.* **2012**, *293*, 1–12.
(28) Tominaga, H; Kiyoshi, M.; Nagai, M. *Chem. Eng. Sci.* **2007**, *62*, 5368–5373.
(29) Barabanov, A. A.; Bukatov, G. D.; Zakharov, V. A.; Semikolenova, N. V.; Mikenas, T. B.; Echevskaja, L. G.; Matsko, M. A. *Macromol. Chem. Phys.* **2006**, *207*, 1368–1375.
(30) Bielawski, C. W.; Benite, D.; Morita, T.; Grubbs, R. H. *Macromolecules* **2001**, *34*, 8610–8618.
(31) Chung, C. K.; Grubbs, R. H. *Org. Lett.* **2008**, *10*, 2693–2696.
(32) De Clerq, B.; Smellinckx, T.; Hugelier, C.; Maes, N.; Verpoort, F. *Appl. Spectrosc.* **2001**, *55*, 1564–1567.
(33) Deslattes, R. D.; Kessler, E. G., Jr.; Indelicato, P.; de Billy, L.; Lindroth, E.; Anton, J. *Rev. Mod. Phys.* **2003**, *75*, 35–99.

Chapter 3

Contributions to Understanding the Mechanistic Role of LiCl in Generating Soluble Organozinc Reagents

Abstract: Employment of a fluorophore-tagged alkyl probe permitted detection of persistent surface intermediates during its direct insertion reaction to commercially available zinc powder. A postdoctoral scholar in the laboratory, Dr. Chao Feng, determined that these surface intermediates were transformed by lithium chloride, leading to the assignment of the mechanistic role of lithium chloride as solubilization of these otherwise persistent surface organometallic intermediates. Subensemble microscopy studies enabled the characterization of the temperature dependence/qualitative barrier of the direct insertion step independently from the multiple chemical and physical steps in the overall reaction. For these studies, I synthesized an aryl iodide probe, which Dr. Feng found did not insert at room temperature; subsequently, I used it at elevated temperatures, and I performed energy-dispersive X-ray spectroscopy (EDS) measurements. These EDS measurements of the elemental composition of the surface of the zinc powder determined that lithium chloride does not remove surface oxides. Pretreatment of the surface with TMSCl, however, effects partial removal of surface oxides within the two hour pre-treatment time previously reported in the empirically optimized synthetic procedure. These studies were reported in two publications, a communication in *J. Am. Chem. Soc.* and a full paper in *Organometallics*, for which I am third and second author, respectively.

Introduction

The direct insertion of organohalides into commercial metal powders would be the most efficient route for the preparation of several organometallic reagents and catalysts. Due to the recalcitrance of many commercial metal powders toward direct insertion, however, such synthetic reactions are not generally employed across much of the periodic table. Preparation of finely divided metal powders for immediate use by in situ reduction of metal halides enables direct insertion reactions with some metals, in exchange for loss of convenience (e.g., with Rieke zinc[1] and calcium[2]). Transformative recent advances by Knochel in the direct insertion of organohalides to commercial zinc,[3] manganese,[4] aluminum,[5] and indium[6] powders in the presence of lithium chloride and/or transition metal catalysts[4] have provided functional-group tolerant access to new reagents, yet the mechanistic roles of these additives in enabling the direct insertion reactions are not well understood.[7]

A recent report from our laboratory described the detection of intermediates on the surface of zinc in the direct insertion of alkyl iodide **3a** to commercial zinc powder[8] (eq 1) using a highly sensitive subensemble in operando fluorescence microscopy technique[9–27]. These surface intermediates are released into solution upon addition of lithium chloride. This observation led to the assignment of the mechanistic role for lithium chloride as the solubilization of otherwise persistent surface organometallic intermediates. Expanded studies of this system are described herein with the goal of further understanding the role of lithium chloride. These studies include temperature dependent studies and examination of the effect of additives on the zinc surface elemental composition by EDS.

The sensitivity of the technique towards detection of small quantities of intermediates enabled determination of the relative reaction barriers of C–I oxidative addition step and complex

dissociation steps separately. These determinations provided qualitative data on structure–reactivity effects on the oxidative addition step separately from the dissociation step. Determination of structure–reactivity relationships on the rates of individual steps in multistep reactions is a long-standing challenge in reaction optimization, especially in the field of organometallic chemistry wherein intermediates often do not build up to the quantities needed for detection by traditional analytical techniques.[28] This fluorescence microscopy approach therefore has potential for broader application in additional systems by enabling direct observation of previously unobserved intermediates and the structure–reactivity relationships of their formation and downstream reaction steps.

Results and Discussion

Reaction of fluorophore-tagged organoiodide **3b** in THF with commercial zinc powder was examined in the presence and absence of lithium chloride, similar to the studies performed by Dr. Feng previously with **3a**. Three mechanistic possibilities were considered for the role of lithium chloride in the formation of soluble organozinc reagents from alkyl iodides and zinc powder: 1) lithium chloride cleans oxides from the surface of the zinc powder[29] before coordination or reaction of the alkyl iodide (similar to the role of I_2 to activate magnesium metal in Grignard reagent formation); 2) lithium chloride solubilizes surface organozinc reagents after oxidative addition, thus producing the solution-phase reagent and exposing the zinc surface to another molecule of alkyl iodide; 3) lithium chloride accelerates oxidative addition as suggested previously through calculations[30].

Probes **3a** and **3b** were designed such that the green BODIPY fluorophore was sufficiently removed electronically and spatially from the reactive carbon–iodide bond so as to serve as a

spectator in the reaction and to avoid potential quenching from the zinc surface and electronic or steric interference with the insertion reaction. As previously reported by our laboratory,[8] reaction of **3a** produces surface species oxidative addition product **3c**, the chemical and physical behavior of which is then examined using in operando fluorescence microscopy. Treatment of these surface species with lithium chloride leads to transformation into solution-phase material **3e**, resulting in disappearance of the fluorescent signal from the surface of the zinc.

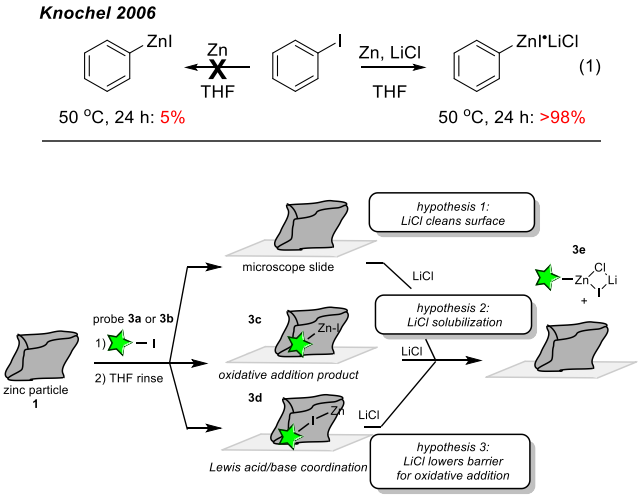

Figure 3.1. Experiment schematic of LiCl-mediated organozinc studies.

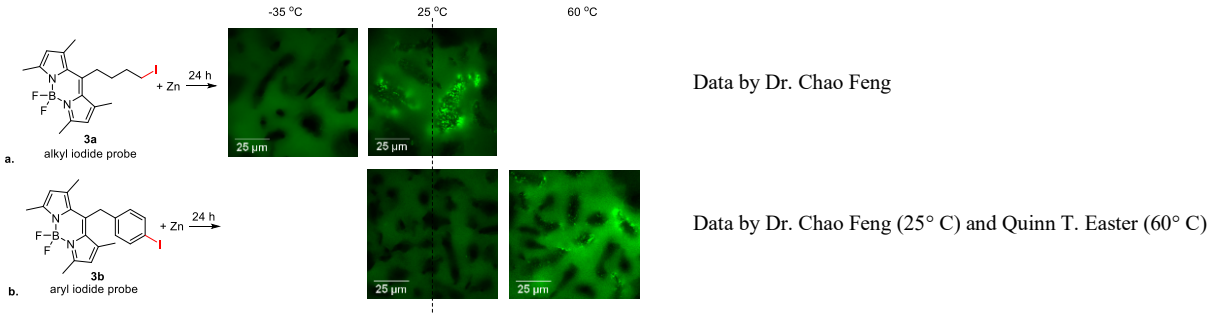

Figure 3.2. Temperature-reactivity studies of organoiodide insertion to zinc metal. The temperature dependence on the degree of reactivity is consistent with oxidative addition barriers.

*Temperature dependence of direct insertion and assignment of surface structure **3c**.* In order to differentiate between structures **3c** (oxidative addition, Figure 3.1) and **3d** (Lewis acid/Lewis base coordination, Figure 3.1), an aryl iodide probe (**3b**) was explored and compared in side-by-side experiments. Probe **3b** contained an sp^2 carbon–iodide bond, which was expected to have a higher barrier towards oxidative addition than the sp^3 carbon-iodide bond of probe **3a**. Aryl iodide compounds that lack electron-withdrawing groups are reported to be significantly less reactive towards direct insertion of zinc, requiring 50 °C rather than ambient temperature for reaction.[3]

Thus, if oxidative addition accounted for the structure on the surface of the zinc then employment of probe **3b** should result in no (or less) product as seen by no (or less) green fluorescent spots on the surface of the zinc. Probe **3b**, however, contains similar iodide nonbonding electrons like those in probe **3a**. Thus, if simple coordination accounted for the species on the surface of the zinc, employment of probe **3b** should result in similar levels of product and thus similar levels of bright green signal on the surface of the zinc particles. In a set of experiments at 25 °C reported in the initial communication,[8] comparison of both probes at 25 °C clearly showed the absence of surface reaction with the aryl iodide probe **3b** in contrast to the high levels of bright green signal on the surface of the zinc with probe **3a**. This result was consistent with the bright green spots arising from oxidative addition. Thus, the surface species were assigned as direct insertion product **3c**, consistent with hypothesis 2.

The temperature-dependent studies are further consistent with the assignment of the surface material as oxidative addition intermediate **3c**. Specifically, reduction of the temperature to –35 °C prevented reactivity with alkyl probe **3a**. Imaging data in Figure 3.2a collected by Dr. Chao Feng showed a complete lack of detectable bright green spots on the surface of the zinc; instead, the

zinc particles remained dark. Lewis acid/Lewis base complexation, in contrast, which avoids breaking the C–I bond, should have a lower barrier than oxidative addition and would plausibly not display such a marked temperature dependence. Similarly, in experiments that I performed, increasing the temperature to 60 °C was sufficient to overcome a higher reaction barrier and lead to reactivity of aryl probe **3b**, as seen by the presence of green material on the surface of the zinc after reaction at this higher temperature (Figure 3.2b), consistent with the aforementioned report[3] of generation of the soluble arylzinc species at 50 °C.

*Assignment of the surface species **3c** as an intermediate in the lithium chloride mediated generation of solution organozinc reagents*. Next, I investigated if the surface material constituted intermediates in the lithium chloride assisted synthesis of soluble organozinc reagents. Studies of salt addition were first disclosed in the original communication:[8] Addition of lithium chloride to **3c** resulted in removal of **3c** from the surface, as seen by the lack of green spots on the surface of the zinc at t = 600 s after addition (Figure 3.3a).

The ability of lithium chloride to transform the surface species from the aryl iodide probe **3b** is consistent with assignment of these species as intermediates in the lithium chloride-assisted generation of soluble organozinc reagents[8]. These results, together with previous results from Dr. Chao Feng, established a mechanistic role for lithium chloride in the generation of soluble organozinc reagents: to remove otherwise persistent surface intermediates through solubilization of **3c**.

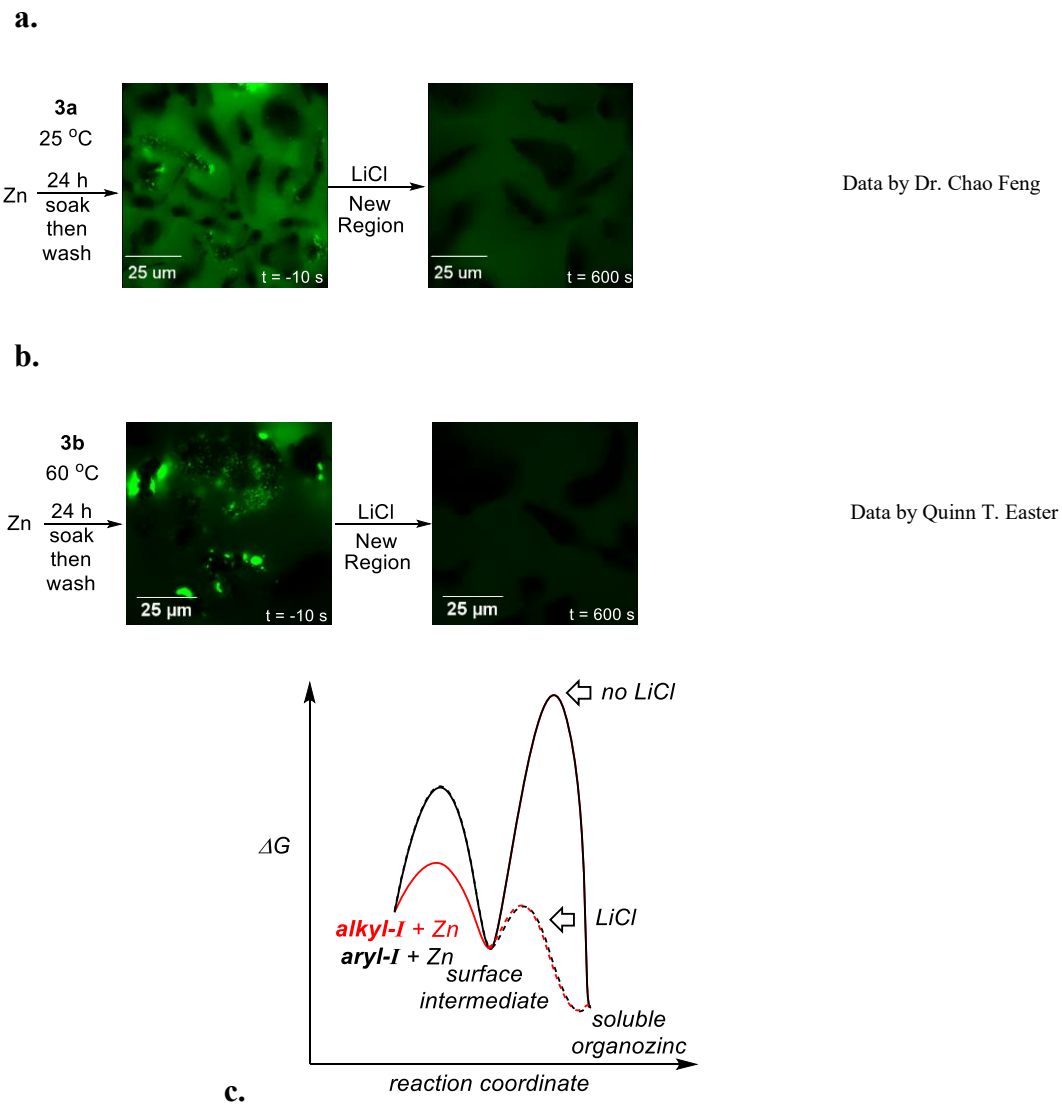

Figure 3.3. a. The addition of LiCl to a Zn sample in THF previously prepared from alkyl iodide **3a** at ambient temperature. Negative times indicate the time before addition of the salt. **b.** The addition of LiCl to a Zn sample in THF previously prepared from aryl iodide **3b** at 60 °C. **c.** Relative barriers of direct insertion and solubilization showing change in rate-determining step in the presence and absence of LiCl.

A change in rate-determining step upon addition of LiCl. Taken together, the lithium chloride addition studies and the comparison of the oxidative addition temperatures for surface reaction with alkyl iodide **3a** and aryl iodide **3b** permit mapping of the relative barriers of the oxidative addition step and solubilization step separately (Figure 3.3c). These separate measurements of single steps were previously obscured by the multiple chemical and physical

changes and the previous analytical inability to detect the small quantities of intermediates that occur during the overall synthetic reaction shown in eq 1.

For ease of comparison of relative reaction barriers, the energies of the starting materials, intermediates, and products were arbitrarily set as identical in the separate reactions of **3a** and **3b**. The data suggests that lithium chloride need not be involved in the oxidative addition steps. Thus, in this system, alkyl and aryl iodides undergo oxidative addition to commercial zinc at 25 ºC and 60 ºC, respectively. In the absence of lithium chloride, the subsequent barriers to solubilization are higher than either of the barriers towards oxidative addition, leading to rate-determining solubilization and persistent intermediate **3c**. In the presence of lithium chloride, however, intermediate **3c** derived from both probes is rapidly removed from the surface at 25 ºC through a low-barrier solubilization step, and oxidative addition becomes rate determining. The current experiments do not address the relative barriers of solubilization of alkyl-derived **3c** and aryl-derived **3c**, only that these barriers are both lower than the corresponding oxidative addition reactions. Thus, in the presence of lithium chloride, the different overall reaction rates for sp^3 and sp^2 organoiodides in the synthetic system reflect the different rates of oxidative addition, with the reported sp^2 aryl iodide requiring higher temperatures to overcome a higher oxidative addition barrier.

Effect of LiCl and TMSCl Additives on Surface Oxide Composition. The observation that lithium chloride transformed the surface intermediates per hypothesis 2 did not rule out that it may also have additional mechanistic roles. To examine if lithium chloride was capable of removing oxides from the surface (hypothesis 1), I examined the elemental composition of the surface via EDS before and after the addition of lithium chloride. Specifically, the molar ratio of zinc to oxygen was examined at 10 different locations spanning measurements at multiple locations on

the surfaces of two or three particles per sample. The heat-treated zinc particles, from the same supplier and the same mesh as in the reported synthetic procedure from Knochel,[3] contained 92.5 ± 6.2 mol % Zn and 7.5 ± 6.2 mol % O (Table 3.1). Thus, the surface of these particles was composed of significant quantities of oxide. The high standard deviation in each number reflected the substantial variation in surface oxide quantities at different locations on the same particle and between different particles, establishing the high heterogeneity of the surface composition of the commercial sample of zinc powder.

Table 3.1. Effect of Additives on Surface Oxide Composition

mol %	as received	LiCl, 2 h	TMSCl, 30 min	TMSCl, 2 h
Zn	92.5 ± 6.2	92.2 ± 4.9	95.7 ± 2.6	96.6 ± 3.7
O	7.5 ± 6.2	7.8 ± 4.9	4.3 ± 2.6	3.4 ± 3.7

Addition of lithium chloride in THF followed by a 2 h soaking time did not result in a measurable decrease in the oxide quantity (Table 3.1), ruling out an additional role for lithium chloride in also cleaning the surface (i.e., ruling out hypothesis 1). The effect of a second additive, TMSCl, was also examined. In the synthetic procedure, the zinc particles are treated for 2 h with TMSCl prior to addition of the alkyl iodide substrate.[3] In contrast to the lithium chloride treatment, treatment with TMSCl affected a gradual decrease in the surface oxygen composition as seen at 30 min and at 2 h. Interestingly, after 2 h detectible oxide remained at some locations on the surface but not at others (i.e., the remaining oxide was below the detection limit of the instrument at some locations with 100% Zn and 0% O). This heterogeneous oxide distribution may contribute along with defect distributions[29] to the observed nonuniform distribution of oxidative addition on the zinc surface by alkyl and aryl iodide probes **3a** and **3b** in Figures 2–5; the imaging data in these figures was acquired after a 2 h treatment with TMSCl, identical to the published synthetic procedure. Taken together, the data from these studies suggests the possibility of improving the

efficiency of the synthetic reaction via increasing the effective concentration of reactive zinc surface for rate-determining oxidative addition by better removal of the surface oxide layer (e.g., by increasing the concentration of TMSCl used in the pre-cleaning step or by increasing the duration of this step).

Conclusion

Subsensemble fluorescence microscopy experiments with up to single-molecule sensitivity permitted interrogation of the mechanistic role of lithium chloride in the direct insertion of alkyl and aryl iodides into commercial zinc power. This technique enabled the assignment of the mechanistic role of lithium chloride as solubilization of otherwise persistent alkyl and aryl zinc intermediates on the surface of the zinc via affecting a change of the rate determining step from solubilization (in the absence of LiCl) to oxidative addition (in the presence of LiCl). These assignments provide full mechanistic insight to the field of additive-assisted direct insertion into commercial metal powders, an area of research that is currently progressing empirically.

An advantage of this technique is the ability to detect and determine the reactivity of intermediates that are present in quantity significantly lower than needed for traditional ensemble analytical techniques. The broader significance of this measurement is the demonstration of subensemble fluorescence microscopy to enable structure–reactivity and mechanistic determination on individual isolated steps in multistep synthetic reactions, including cases in which intermediates are present in sufficiently low quantities as to be undetectable by traditional ensemble techniques—an ability that addresses a longstanding analytical challenge in mechanism-based reaction design and synthetic method improvement.

Experimental

General methods. All manipulations were carried out under a nitrogen atmosphere in dried glassware unless otherwise noted. All chemicals were used as received from commercial sources unless otherwise noted. THF was dried by passage through an alumina column under argon pressure on a Seca Solvent System (Glass Contour). Zinc powder (99.9%) was purchased from Strem and dried in vacuo while applying heat from a heat gun for ca. 30 min. Trimethylsilyl chloride was purified by stirring over CaH_2 for 24 h and was then vacuum transferred. Flash chromatography was conducted using a Teledyne Isco Combiflash Rf 200 Automated Flash Chromatography System. All proton and carbon nuclear magnetic resonance (^1H and ^{13}C NMR) spectra were recorded on a Bruker DRX-500 spectrometer outfitted with a cryoprobe. All coupling constants were measured in Hertz (Hz). Chemical shifts were reported in ppm and referenced to residual protiated solvent peak (δ_H = 7.26 ppm for $CDCl_3$ in ^1H NMR spectroscopy experiments; δ_C = 77.16 ppm for $CDCl_3$ in ^{13}C NMR spectroscopy experiments). High-resolution mass spectrometry data were obtained at the University of California, Irvine.

Microscopy and image acquisition. Imaging was performed with an IX71 inverted microscope (Olympus Corporation) and an oil-immersion objective with a 1.49 numerical aperture. Samples were illuminated with the 488 nm line of an Ar/Kr ion laser (Coherent Inc.) set to 25 mW. Illumination was done under conditions of EPI. Samples were imaged with a C9100-13 electron multiplier CCD camera (Hamamatsu Photonics). The CCD chip was a back-thinned electron multiplication type with an effective 512 × 512 array of pixels.

Construction of reaction cells. Reaction cells were constructed from a 1 dram vial by cutting of the bottom of the vials and adhering it to the prepared glass coverslip with Devcon 5

Minute® Epoxy. The epoxy was allowed to cure for 1 h. The glass reaction cells were then dried under dynamic vacuum for 12 h before being brought into the glovebox.

*Synthesis of aryl iodide probe **3b**.*

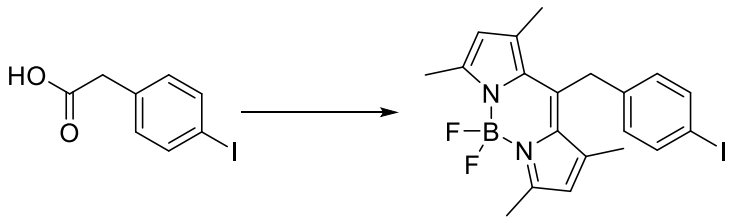

3b

An oven-dried 100 mL round bottom flask was charged with 4-iodophenylacetic acid (400. mg, 1.53 mmol) and a stirbar, capped with a septum, and placed under a dynamic nitrogen atmosphere. Dry CH_2Cl_2 (30 mL), DMF (used as received, 0.010 mL, 0.013 mmol) were added to dissolve the solid, and the solution was stirred. Oxalyl chloride (0.144 mL, 1.68 mmol) was added dropwise over 1 min via syringe to the solution, resulting in a slow evolution of gas. After stirring the solution at room temperature for 1 h, the solution was concentrated in vacuo via rotary evaporation to yield a pale yellow oily solid, then further concentrated via a high vacuum line for 1 h to remove excess oxalyl chloride.

The resulting acid chloride was redissolved in dry CH_2Cl_2 (25 mL). Phosphorus oxychloride (0.157 mL, 1.68 mmol) was added via syringe through a septum to this solution, followed by the addition of 2,4-dimethylpyrrole (0.394 mL, 3.83 mmol) dropwise via syringe over 1 min. The septum was removed, and a reflux condenser, equipped with a septum and under dynamic nitrogen, was immediately fitted onto the flask. The solution was stirred and heated at reflux for 5 h. After cooling to room temperature, the solution was concentrated in vacuo, layered with hexanes (70 mL) to remove impurities, and stored overnight at –35 °C. After decanting the hexanes, the remaining residue was subjected to high vacuum for 1 h before being dissolved in dry

toluene (25 mL). This solution was then treated with 1,8-diazabicyclo[5.4.0]undec-7-ene (0.342 mL, 2.30 mmol) and stirred at 80 °C for 1 h. Boron trifluoride dimethyletherate (0.188 mL, 2.05 mmol) was added to the solution via syringe, and the mixture was stirred at 80 °C for 1 h, resulting in a deep red solution. The solution was cooled to room temperature and washed with water (3 × 50 mL) and brine (3 × 50 mL). The organic layer was dried over magnesium sulfate, filtered with filter paper, and concentrated in vacuo to yield a dark red solid. The resulting solid was first purified by silica gel flash column chromatography using an elution of 50% CH_2Cl_2 in hexanes (R_f = 0.53). Because ultrapure material was desired, two column fractions were chosen from the resulting chromatography purification and concentrated in vacuo separately, yielding brightly colored red-orange solids.

The fraction that eluted from the column first was separately triturated twice with ethyl acetate (2 × 5 mL) to remove any impurities from the sample. Removal of the organic layer left intensely colored red-orange solid **3b** (16.2 mg, 1.9%). ^{1}H NMR ($CDCl_3$, 500 MHz): δ 7.61 (d, J = 8.3 Hz, 2H), 6.93 (d, J = 8.2 Hz, 6.03 (s, 2H), 4.31 (s, 2H), 2.55 (s, 6H), 2.16 (s, 6H). HRMS (ESI+) m/z calcd. for $C_{20}H_{20}N_2BF_2I$ ([M+Na]+) 487.0634, found 487.0642.

The fraction that eluted from the column second was separately triturated twice with ethyl acetate (2 × 5 mL) to remove any impurities from the sample. Removal of the organic layer left intensely colored red-orange solid **3b** (21.2 mg, 2.5%). Analysis of the ^{1}H NMR spectrum of this sample indicated that 3.2% of an unknown impurity remained after trituration. This sample was analytically pure; however, the other sample did not contain this impurity. Therefore, the first sample was used for microscopy experiments. ^{1}H NMR ($CDCl_3$, 500 MHz): δ 7.61 (d, *J* = 8.3 Hz, 2H), 6.93 (d, *J* = 8.2 Hz, 6.03 (s, 2H), 4.31 (s, 2H), 2.55 (s, 6H), 2.16 (s, 6H). 13C NMR (CDCl3,

126 MHz): δ 155.1, 141.2, 139.8, 138.1, 136.5, 132.5, 129.8, 121.9, 92.1, 33.1, 16.1, 14.6. HRMS (ESI+) m/z calcd. for $C_{20}H_{20}N_2BF_2I$ ([M+Na]+) 487.0634, found 487.0642.

The combined yield of these two samples of **3b** was 37.4 mg (4.4%).

*Reaction of zinc with aryl iodide probe **3b**.* In a nitrogen filled glove box, zinc particles (77.4 mg, 1.18 mmol) were weighed out into a 1 dram scintillation vial. To this vial was added THF (1.0 mL) via syringe, followed by 1 drop of TMSCl. The vial was capped and the solution was allowed to stand for 2 h. Following the 2 h period, the THF was removed from the vial via syringe. The particles were washed with 2 × 2 mL THF portions added via syringe. In a separate 1 dram vial, probe **3b** (1.0 mg, 0.0022 mmol) was weighed out and dissolved in 1.0 mL THF. This afforded a solution of 2.2 mM **3b**, 30 drops of which were then added to the Zn particles. The vial was capped and heated to 60 ºC for 24 h. After 24 h, the residual solution was removed, and the Zn particles were washed with 3 × 2 mL portions of THF added via syringe. The particles were agitated with 3.0 mL THF, and one third of this agitated solution was added to a microscope reaction vial. In salt addition experiments, lithium chloride (8.2 mg, 0.19 mmol) was added to a glass salt pocket; this salt pocket was gently placed inside the microscope reaction vial. The vial was capped, removed from the glove box carefully without shaking, and taken directly to the microscope.

The cells were imaged for 11 min each. Zinc particles with fluorescent signals were found and kept in focus. After imaging the reaction cell for 40 s and observing the surface bound intermediate, the salt was added by inverting the cell and gently shaking the cell, this was repeated three times. After putting the cell back onto the microscope, zinc particles were found and brought into focus at 100 s after the salt addition and these particles were kept in focus until 540 s after the

addition, after which the stage was moved to find new zinc particles that had not yet been exposed to laser illumination at 600 s.

Surface elemental composition determination via EDS. Heat-treated[3] but otherwise used as received from manufacturer: In a nitrogen-filled glove box, Zn was added to a 1 dram vial. This vial was capped and brought out of the glove box for imaging. To prepare the sample for imaging, the Zn was scraped out of the vial using a spatula and placed on carbon tape mounted on a metal stand.

Treated with LiCl: In a nitrogen-filled glove box, heat-treated Zn[3] (74.8 mg, 1.14 mmol) was weighed out into a 1 dram vial. THF (1.0 mL) was added to the vial via syringe. In a separate 1 dram vial, LiCl (8.2 mg, 0.19 mmol) was weighed out and added to the Zn/THF vial with a spatula. The vial was capped and agitated, and the solution was allowed to stand for 2 h. After the 2 h period, the THF was syringed out of the vial, and the particles were washed with 2 x 2 mL portions of THF, added via syringe. The vial was then capped and taken out of the glove box. To prepare the sample for imaging, the Zn particles were scraped out of the vial using a spatula and placed on carbon tape mounted on a metal stand.

Treated with TMSCl: In a nitrogen-filled glove box, heat-treated Zn[3] (79.1 mg, 1.21 mmol) was weighed out into a 1 dram vial. THF (1.0 mL) was added to the vial via syringe, followed by 1 drop of TMSCl. The vial was capped, and the solution was allowed to stand for 30 min or 2 h. Following this 30 min or 2 h period, THF was syringed out of the vial, and the particles were washed with 2 x 2 mL THF portions added via syringe. The vial was capped and taken for imaging the sample. To prepare the sample for imaging, the Zn particles were scraped out of the vial using a spatula and placed on carbon tape mounted on a metal stand.

Scanning electron microscopy (SEM) was accomplished by using a FEI Quanta 3D FEG Dual Beam (FEI Company) in the Laboratory for Electron and X-ray Instrumentation (LEXI) at the University of California, Irvine. Samples were imaged on carbon tape at 1.0 kV energy, 43 pA current, and pressures lower than 8×10^{-5} mbar using the xTm software (FEI Company) with XJ Charts (XJ Technologies). Images were collected at varying magnifications with a 1024×943 pixel resolution. Energy-dispersive X-ray spectroscopy (EDS) was performed on the FEI Quanta 3D using the Oxford EDS Detector for Quanta 3D (Oxford Instruments) in the LEXI facilities. Samples were imaged as prepared with 20.0 kV energy and 43 pA current at pressures below 8×10^{-5} mbar. Samples were viewed using the xTm software, and after images were selected, data was collected and interpreted using the INCA software (v. 4.15, Oxford Instruments Analytical Limited). The Zn Kα lines were measured at 8.60 and 9.60 keV, the Zn Lα line was measured at 1.1 keV, and the O Kα line was measured at 0.62 keV.[31]

References

(1) Rieke, R. D.; Li, P. T.; Burns, T. P.; Uhm, S. T. *J. Org. Chem.* **1981**, *46*, 4323–4324.
(2) Wu, T.-C.; Xiong, H.; Rieke, R. D. *J. Org. Chem.* **1990**, *55*, 5045–5051.
(3) Krasovskiy, A.; Malakohov, V.; Gavryushin, A.; Knochel, P. *Angew. Chem. Int. Ed.* **2006**, *45*, 6040–6044.
(4) Peng, Z.; Knochel, P. *Org. Lett.* **2011**, *13*, 3198–3201.
(5) Bluemke, T.; Chen, Y.-H.; Peng, Z.; Knochel, P. *Nat. Chem.* **2010**, *2*, 313–318.
(6) Shen, Z. L.; Knochel, P. *Chem. Eur. J.* **2015**, *21*, 7061–7065.
(7) Koszinowski, K.; Boehrer, P. *Organometallics* **2009**, *28*, 771–779.
(8) Feng, C.; Cunningham, D. W.; Easter, Q. T.; Blum, S. A. *J. Am. Chem. Soc.* **2016**, *138*, 11156–11159.
(9) Hensle, E. M.; Blum, S. A. *J. Am. Chem. Soc.* **2013**, *135*, 12324–12328.
(10) Esfandiari, N. M.; Blum, S. A. *J. Am. Chem. Soc.* **2011**, *133*, 18145–18147.
(11) Ng. J. D.; Upadhyay, S. P.; Marquard, A. N.; Lupo, K. M.; Hinton, D. A.; Padilla, N. A.; Bates, D. M.; Goldsmith, R. H. *J. Am. Chem. Soc.* **2016**, *138*, 3876–3883.
(12) Cordes, T.; Blum, S. A. *Nat. Chem.* **2013**, *5*, 993–999.
(13) Blum, S. A. *Phys. Chem. Chem. Phys.* **2014**, *16*, 16333–16339.
(14) Chen, P.; Zhou, X.; Shen, H.; Andoy, N. M.; Choudhary, E.; Han, K.-S.; Liu, G.; Meng, W. *Chem. Soc. Rev.* **2010**, *39*, 4560–4570.
(15) Roeffaers, M. B. J.; Sels, B. F.; Uji-i, H.; De Schryver, F. C.; Jacobs, P. A.; De Vos, D. E.; Hofkens, J. *Nature* **2006**, *439*, 572–575.

(16) Esfandiari, N. M.; Wang, Y.; Bass, J. Y.; Cornell, T. P.; Otte, D. A. L.; Cheng, M. H.; Hemminger, J. C.; Mcintire, T. M.; Mandelshtam, V. A.; Blum, S. A. *J. Am. Chem. Soc.* **2010**, *132*, 15167–15169.
(17) Shen, H.; Zhou, X.; Zou, N.; Chen, P. *J. Phys. Chem. C* **2014**, *118*, 26902–26911.
(18) Esfandiari, N. M.; Wang, Y.; Bass, J. Y.; Blum, S. A. *Inorg. Chem.* **2011**, *50*, 9201–9203.
(19) Kubarev, A.V.; Janssen, K. P. F.; Roeffaers, M. B. J. *ChemCatChem* **2015**, *7*, 3646–3650.
(20) Sambur, J. B.; Chen, T. Y.; Choudhary, E.; Chen, G. Q.; Nissen, E. J.; Thomas, E. M.; Zou, N. M.; Chen, P. *Nature* **2016**, *530*, 77–80.
(21) Esfandiari, N. M.; Wang, Y.; Mcintire, T. M.; Blum, S. A. *Organometallics* **2010**, *30*, 2901–2907.
(22) Decan, M. R.; Impellizzeri, S.; Marin, M. L.; Scaiano, J. C. *Nat. Commun.* **2014**; DOI: 10.1038/ncomms5612.
(23) Sambur, J. B.; Chen, P. *J. Phys. Chem. C* **2016**, *120*, 20668–20676.
(24) Ristanović, Z.; Kerssens, M. M.; Kubarev, A. V.; Hendriks, F. C.; Dedecker, P.; Hofkens, J.; Roeffaers, M. B. J.; Weckhuysen, B. M. *Angew. Chem. Int. Ed.* **2015**, *54*, 1836–1840.
(25) Ristanović, Z.; Hofmann, J. P.; De Cremer, G.; Kubarev, A. V.; Tohnke, M.; Meirer, F.; Hofkens, J.; Roeffaers, M. B. J.; Weckhuysen, B. M. *J. Am. Chem. Soc.* **2015**, *137*, 6559–6568.
(26) Wang, N.; Tachikawa, T.; Majima, T. *Chem. Sci.* **2011**, *2*, 891–900.
(27) Easter, Q. T.; Trauschke, V.; Blum, S. A. *ACS Catal*. **2015**, *5*, 2290–2295.
(28) For an example, see: Romero, P. E.; Piers, W. E. *J. Am. Chem. Soc.* **2005**, *127*, 5032–5033.
(29) Porter, F. C. Corrosion Resistance of Zinc and Zinc Alloys; CRC Press: Boca Raton, FL, 1994; p 121.
(30) Liu, C.-Y.; Wang, X.; Furuyama, T.; Yasuike, S.; Muranaka, A.; Morokuma, K.; Uchiyama, M. *Chem. Eur. J.* **2010**, *16*, 1780–1784.
(31) Deslattes, R. D.; Kessler, E. G., Jr.; Indelicato, P.; de Billy, L.; Lindroth, E.; Anton, J. *Rev. Mod. Phys.* **2003**, *75*, 35–99.

Chapter 4

Single Turnover at Molecular Polymerization Catalysts Reveals Spatiotemporally Resolved Reactions

Abstract: Multiple active individual molecular ruthenium catalysts were pinpointed within growing polynorbornene, revealing reaction dynamics and location information that is unavailable through traditional ensemble experiments. These experiments are the first single-turnover fluorescence microscopy imaging at any molecular catalyst and achieve the detection of individual monomer reactions at an industrially important molecular ruthenium ring-opening polymerization (ROMP) catalyst under synthetically relevant catalytic conditions (e.g., unmodified industrial catalyst, ambient pressure, condensed phase, ~0.03 M monomer). These results further establish the key fundamentals of this imaging technique for characterizing the reactivity and location of active molecular catalysts even when they are the minor components.

Introduction

Catalysis is a multibillion-dollar world-wide industry, but the determination of the phase and local environment of active catalysts is a long-standing analytical challenge.[1,2] This is especially true in reactions at the homogenous/heterogeneous interface where the (unknown) phase and locations of the active catalyst can have a profound effect on its local environment and thus reactivity and selectivity. Herein we employ fluorescence microscopy to monitor single-monomer insertion reactions at individual molecular catalysts under synthetically relevant conditions. Resultant imaging data revealed phase-[3,4] and spatiotemporally resolved individual active molecular ruthenium catalysts within growing polymers for the first time, thereby providing

information that is unavailable through traditional ensemble techniques. The industrially important[5] monomer norbornene and catalyst **4a** were selected for initial studies. Catalyst **4a** is inactive when phosphine is coordinated;[6] thus, the presence of ruthenium does not imply catalytic activity.

Although well-known in biological systems,[7,8] zeolite,[9–16] and nanoparticle catalysis,[17–21] this is the first example where single-molecule fluorescence microscopy has been used to visualize single-turnover events with a molecular catalyst.[3–40] Given that molecular catalysts make up a significant portion of all catalysis, imaging turnover in these systems at the single-molecule level holds great potential to reveal information on reactivity hidden by ensemble averaging, similar to what has been achieved with biological, zeolite, and nanoparticle systems[7–21].

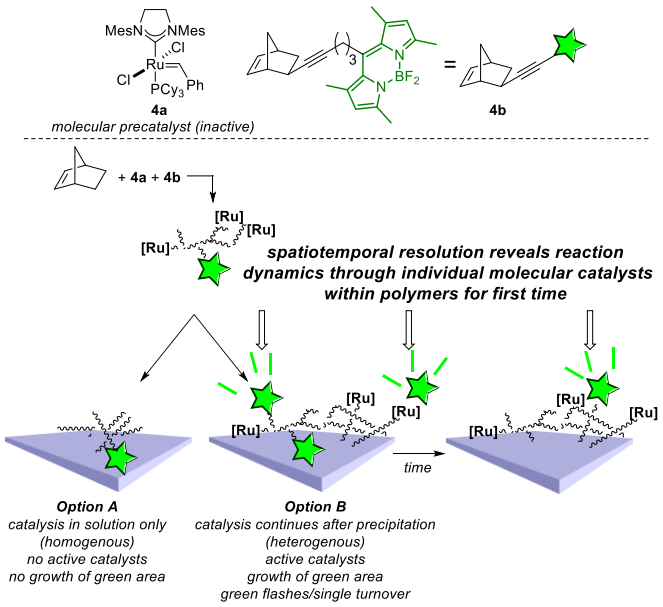

Figure 4.1. Experiment schematic to locate active molecular catalysts with spatiotemporal resolution. Mes = 2,4,6-trimethylphenyl. Squiggly lines represent polymers.

The added challenge with molecular catalysts is their small size means they diffuse rapidly

in solution, precluding imaging. Methods based on stoichiometric reactions of molecular species chemically tethered to glass to reduce their motion and make them sufficiently stationary for imaging have not yet yielded catalytic turnover. In contrast, we demonstrate a strategy (Figure 4.1) that uses unmodified catalyst **4a**, which is widely employed in industrial syntheses of polymers,[6] pharmaceutical candidates,[41] and complex molecules.[42] No tethering to an artificial surface,[27–29,32,38–40] which may alter its reactivity,[31] is necessary. Instead, the experiments herein harness the changing solubility and large size of growing polymers in a precipitation polymerization reaction to aid in imaging individual active molecular catalysts; such catalysts, derived from **4a**, within precipitated polymers were sufficiently stationary for successful imaging of single ROMP reactions. Unlike AFM techniques that study individual catalyst sites, this technique does not require atomically smooth model surfaces.[14]

Results and Discussion

This study was enabled by probe **4b**, which contained a norbornene/alkyne reactive group capable of catalytic incorporation into the growing polymer via ROMP or enyne metathesis.[43] The reactive group was tethered via a carbon spacer to a green BODIPY fluorophore. Probe **4b** was designed so the fluorophore was intentionally separated from the reactive unit; thus, incorporation of probe **4b** into the growing polymer would not affect its fluorescence.

The key imaging concept was that the majority of monomer **4b** remained in solution diffusing rapidly and was therefore not detected in total internal reflectance fluorescence (TIRF) mode. Only when probe **4b** reacted with active catalyst within a precipitated polymer did its diffusion become slowed,[17] resulting in its imaging as a bright green point flash. If precipitated polymers contained active catalysts, incorporation of probe **4b** by ROMP would therefore create

a single flash at a polymer-containing location on the surface that was previously dark (Figure 4.1, Option B). If, in contrast, the precipitated polymer did not contain active catalysts, no incorporation of tagged monomer would occur and no flashes would be observed (Figure 4.1, Option A). Importantly, this strategy would image only the behavior from active ruthenium catalysts, because inactive ruthenium would not incorporate monomer or produce a fluorescence signal.

The strategy to resolve the signals of individual chemical reactions was to dope a small amount of probe **4b** into a sample of mostly untagged monomer. In this way, the fluorescence signal from chemical incorporation of individual probe molecules could be resolved, since untagged monomers comprising most of the sample were dark. Specifically, probe **4b** was added to the reaction at 2×10^{-13} M with 2.6×10^{-2} M untagged monomer in heptane, leading to an ultimate ratio of tagged:untagged monomer of $1:1.3 \times 10^{11}$. Therefore, 1 in 130 billion monomers was labeled with a tag. The polymer formed under these conditions had similar physical and chemical properties to the untagged polymer, such that addition of the probe was not expected to produce physical or chemical artifacts. Thus, except for 1 in 10^{11} monomers carrying a fluorophore tag, the experimental conditions mirror those of the synthesis, and a model system was not needed.

Probe **4b** was doped into polymerization reactions with norbornene. Examination of this sample from t = 2–33 min showed a dynamic image, with multiple flashes occurring across the image. A representative subset of this field of view is shown in Figure 4.2 (see Experimental for data showing widespread activity). Each frame showed only a few green signals; thus, a composite image provided a straightforward way to assess the locations of all signals in the sample. Figure 4.2a shows a composite image of this activity from t = 7–11 min. The locations of the green-fluorescing precipitated polynorbornene on the coverslip surface are easily determined by

summing multiple resolvable individual events in a composite polymerization image. These precipitated polymers are likely aggregates rather than single strands[26] (giving rise to a range of shapes). These aggregates are likely derived from many separate ruthenium catalysts,[26] and may thus contain multiple ruthenium complexes per precipitated particle. GPC analysis confirmed polymer presence at t = 7 min (M_n = 50000 g/mol, PDI = 2.01).

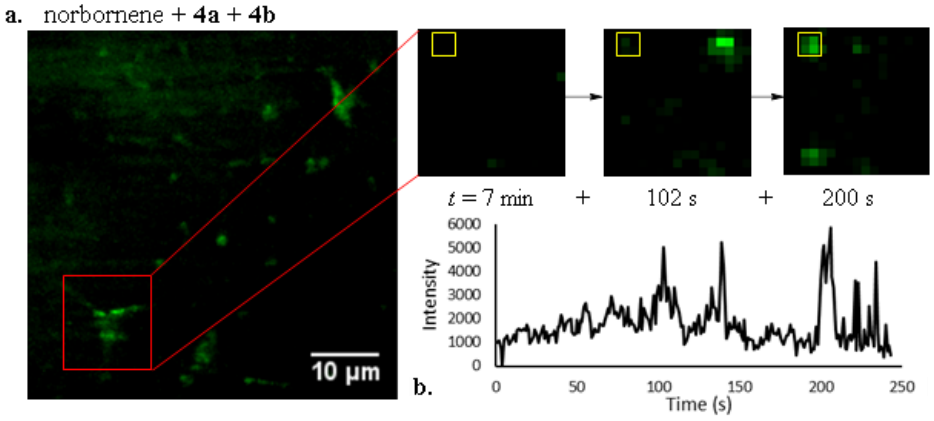

Figure 4.2. Reaction of norbornene, catalyst **4a**, and probe **4b** at 0.2 pM. **a.** Composite image made from the sum of all signal over time of reaction of norbornene, with catalyst **4a** and probe **4b**. Precipitated polynorbornene is visible as bright green features on the surface of the glass. These polymers exhibited catalytic activity, evidenced by bright green quantized flashes at specific time points, corresponding to single monomer reactions of **4b** (in expansions). **b.** Intensity vs. time trace of region within yellow box; reactions with individual molecules of **4b** are observable as peaks.

Conditions were chosen for initial experiments wherein the photobleaching of a tagged monomer was faster than its incorporation, thus leading to the disappearance of the signal shortly after incorporation. Examination of the intensity vs. time traces of 534 x 534 nm^2 regions showed that many of these flashes corresponded to the quantized, stepwise incorporation and photobleaching events that are the well-established fingerprints of single molecules[33]. Figure 4.2b shows an example time trace corresponding to the region inside the yellow box. Given the low concentration of the fluorophore, these multiple events likely do not occur at the same ruthenium complex. Variability in the 3-dimensional locations of active ruthenium within precipitated

polymer aggregates likely contributes to the observed variation in intensity per event (see full time course movie in Experimental).

Chemical poisons that successfully halt other ruthenium-catalyzed olefin metathesis reactions are reported to be insufficient to stop norbornene ROMP.[44] Thus, we turned to control experiments to determine the origin of the fluorescence in the precipitated polymer system. Probe **4c**, which did not contain a metathesis unit, showed no incorporation of fluorescence into polynorbornene under otherwise identical conditions. Similarly, a control experiment in the absence of catalyst **4a** showed no polymer formation (see movies in Experimental). Thus, the signal was chemically specific to both norbornene and catalyst **4a**. Therefore, the quantized fluorescent signals in Figure 4.2b were attributed to individual chemical ROMP reactions at single catalytic ruthenium centers in precipitated polynorbornene (Figure 4.1, Option B).

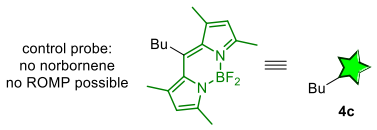

If active ruthenium was present in the polymer, it should be present even if the mother liquor was removed. To examine this hypothesis, a modified experimental protocol was next performed (Figure 4.3). In this modified experiment, untagged monomer was added to catalyst **4a** in the absence of fluorophore probe. At t = 5 min, the surfaces of the microscope coverslips were dark, as expected in the absence of fluorophore. At t = 5 min, the mother liquor was removed, and probe **4b** was added to residual precipitated polymers at a concentration of 2×10^{-13} M; fresh catalyst **4a** may still be present in this solution given that its limited solubility precludes complete withdrawal during removal of the mother liquor.

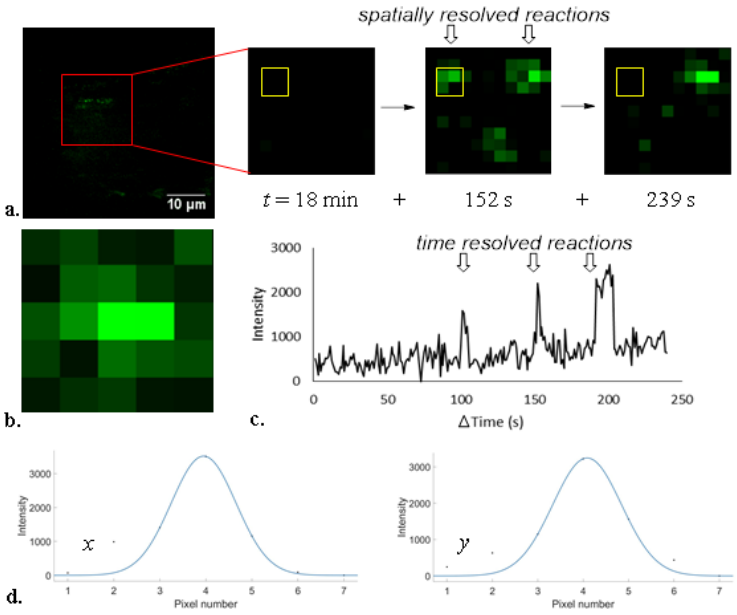

Figure 4.3. Spatiotemporal resolution of catalytic activity at molecular catalysts in precipitated polymers using probe **4b** at 1 pM. **a.** Single chemical reactions with probe **4b** in preformed precipitated polynorbornene. **b.** Enlargement of individual chemical events; Δt = 200 s. Each pixel corresponds to 267 x 267 nm^2. **c.** Intensity vs. time trace of 534 x 534 nm^2 region in yellow box in part *a*. Peaks correspond to individual chemical reactions with probe **4b**. **d.** Fitting of 2D point spread functions of the signal in **b.**, along the x and y axes.

Spatiotemporally resolved chemical reactions were observed between single monomers and the polymers that had previously precipitated and that were previously dark (Figure 4.3c, stepwise increases; see Experimental for full time course movie). These observations pinpoint the location of individual active ruthenium complexes operating within the precipitated polymers, corresponding to Option B in Figure 4.1, since probe **4b** was not present until after precipitation.[29] 2D point spread functions of these signals showed them to be consistent with single-molecule detection, demonstrating suitable spatial resolution for future applications of this superresolution technique (example, Figure 4.3d; see Experimental for details).

When performing an experiment wherein only a small fraction of all of the material is observed (e.g., ~1 in 130 billion norbornene monomers), it is important to consider if the observed reaction is representative of the overall reaction. To examine this point, the experiment was

performed at a higher ratio of tagged-to-untagged norbornene, which was achieved by increasing the concentration of **4b** by 1000x, to 2 x 10^{-10} M, such that bulk behavior of the sample could be compared to that observed at the single-turnover level. Under these conditions, polynorbornene incorporated probe **4b** while growing in solution, seen as fluorescent green polymer aggregates precipitating from solution (Figure 4.4a, polynorbornene, t = 1 min after mixing). These aggregates continued to incorporate **4b** after precipitation (Figure 4.4a; examples in yellow boxes). Under these conditions, incorporation of tagged monomer was sufficiently fast that individual catalytic reactions could not be resolved, seen as the absence of clear quantized increases in the intensity vs. time traces (representative example, Figure 4.4a; additional examples are given in Experimental).

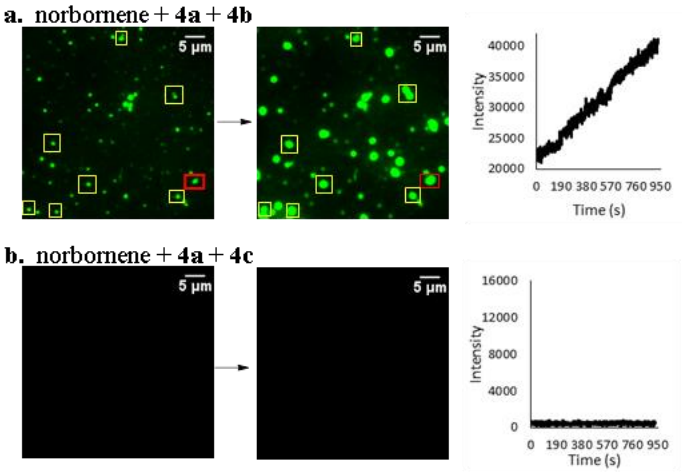

Figure 4.4. The rate of insertion of probe **4b** at 0.2 nM into polynorbornene is faster than photobleaching. **a.** Precipitated polynorbornene, identifiable as bright green features, grew brighter and bigger. **b.** Precipitated polynorbornene with control probe **4c** remained dark and featureless.

A control experiment with probe **4c** and norbornene under otherwise identical conditions showed no incorporation of fluorophore into polynorbornene either in solution or within the precipitated polymers, further confirming the chemical specificity of the incorporation processes (Figure 4.4b; see Experimental for the full timecourse movie). This also confirmed that the

behavior detected at the single-molecule level was representative of general catalytic polymerization behavior.

Conclusion

In conclusion, single-turnover detection at individual molecular catalysts was achieved for the first time with fluorescence microscopy, thereby revealing active catalysts within growing polymers with spatiotemporal resolution, information unavailable through traditional ensemble techniques. These experiments lay the groundwork for superresolution and temporally resolved rate studies of catalytic reactions. Given the global importance of molecular polymerization catalysis and molecular catalysis generally, we anticipate that this technique will see additional applications. More broadly, these studies establish key foundations for determining, under synthetically relevant conditions, missing information on the location and reactivity of molecular active catalysts that is currently hidden by less-sensitive analytical techniques.

Experimental

I. General Information

All reagents and solvents were used as received from commercial sources unless otherwise noted. Analytical thin layer chromatography (TLC) was performed using Merck F_{250} plates and visualized under UV irradiation at 254 nm. Flash chromatography was conducted using a Teledyne Isco Combiflash® Rf 200 Automatic Flash Chromatography System, and Teledyne Isco Redisep® 35–70 μm silica gel. Spectrophotometric grade heptane (OmniSolv) was used for all microscopy studies. Catalyst **1** (Grubbs Catalyst, 2nd Generation) was purchased from Sigma-Aldrich. Ultra-pure water with >18 MΩ resistance and total organic content of <5 ppb was obtained from a

Milli-Q Gradient A10 water purifier (Millipore, Billerica, MA) using a Q-Gard 2 purification pack and a Quantum EX Ultrapure Organex cartridge. All proton and carbon nuclear magnetic resonance (^{1}H and ^{13}C NMR) spectra were recorded on a Bruker DRX-500 spectrometer outfitted with a cryoprobe. All coupling constants were measured in Hertz (Hz). Chemical shifts were reported in ppm and referenced to residual protiated solvent peak (δ_H = 7.26 ppm for $CDCl_3$ in ^{1}H NMR spectroscopy experiments; δ_C = 77.16 ppm for $CDCl_3$ in ^{13}C NMR spectroscopy experiments). High-resolution mass spectrometry data were obtained at the University of California, Irvine.

II. Construction of Reaction Cells and Preparation of Coverslips for Microscopy

Glass coverslips (25 × 25 mm, No. 1.5, VWR Scientific) with a thickness of 0.17 mm were cleaned by sonication in 20 mL of a 0.6% solution of Hellmanex Detergent (Fisher Chemical) in MilliQ water for 60 min and then rinsed sequentially with MilliQ water and spectrophotometric grade ethanol six times. The rinsed coverslips were dried with compressed air, then placed on aluminum foil and further dried in an oven at 115 °C for 10 to 20 min. Coverslips were either stored covered in aluminum foil or used immediately after drying.

Bottomless vials were formed by cutting the ends from glass reaction vials (Short Form Style, VWR Scientific). The resulting cylinders were rinsed thoroughly with MilliQ water and spectrophotometric grade ethanol and dried in an oven at 115 °C for 20 to 30 min before use.

To assemble the reaction cells, the cleaned and dried hollow bottomless vials were attached to the cleaned coverslips by applying epoxy (Devcon) to the outside base of the tubes, then the assembled tubes were covered with aluminum foil and stored overnight or longer before use in microscopy experiments.

III. Microscopy Parameters

All microscopy imaging was performed with an inverted microscope (IX71, Olympus Corporation) and an oil-immersion, 60x objective with a 1.45 numerical aperture. Samples were imaged with a C9100-13 CCD camera (Hamamatsu Photonics). Fluorescence microscopy samples were illuminated with the 488 nm line obtained from a Ar/Kr ion laser (Coherent Inc.) set to 1.00 W. The CCD chip was a back-thinned electron multiplication type with an effective 512 × 512 array of pixels. The cell size was 16 μm, which with the 60x objective resulted in each pixel in the acquired images representing an area of approximately 270 × 270 nm. The focus was changed with a *z*-axis controller (MS-2000, Applied Scientific Instruments, Inc.). All images were acquired in total internal reflection fluorescence (TIRF).[27] The SlideBook 6.0 software (Intelligent Imaging) was set to acquire images every 1 s with 300 ms exposure to the 488 nm line per frame. Images were viewed in ImageJ (NIH, available at http://rsbweb.nih.gov/ij/).

The minimum, maximum, and gamma values in SlideBook were changed according to the fluorescence microscopy experimental parameters but held constant for all controls and repetitions of data (Section VI and Section IX). When probes **4b** and **4c** (Section IV) were added at t = 0 min at a final concentration of 0.2 nM, the values were initially set to min = 2500, max = 25000, and gamma = 2.5. When probes **4b** and **4c** were added at t = 0 min at a final concentration of 0.2 pM, the values were initially set to min = 7000, max = 17232, and gamma = 1.9. Finally, when probe **4b** was added at t = 5 min at a final concentration of 1 pM, the values were set to min = 4000, max = 6000, and gamma = 2.5. For clarity and comparison, both the raw data microscopy images and the images adjusted according to the above parameters have been added to Experimental (vide infra). All microscopy images were cropped to 48 × 48 μm^2. Further cropping was done to resolve single molecules in Figure 4.2 (4.25 × 4.25 μm^2) and Figure 4.3 (2.75 × 2.75 μm^2). When probes

4b and **4c** (Section IV) were added at t = 0 min at a final concentration of 0.2 nM or 0.2 pM, the exposure rate was set to 100 ms, and image capture was set to 1 s.

In ImageJ, green color was added to the videos obtained from Slidebook. For videos where probes **4b** and **4c** were added at 0.2 pM, and the video where probe **4b** was added at 1 pM, the gamma was set to 2.00, and the brightness was initially set to 75, then reset to 75.

IV. Synthetic Procedures

a) *Synthesis of norbornene alkyne ester **4d**.*[45]

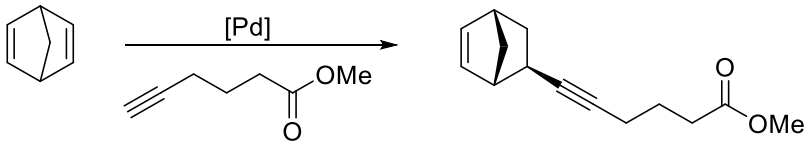

4d

In a nitrogen glove box, a 100 mL round-bottom flask was equipped with a stir bar. Both the flask and stir bar had been heated in an oven and placed under vacuum in the antechamber overnight before pumping into the box. The Herrmann-Beller palladium catalyst (211 mg, 0.225 mmol) was weighed out into this flask, which was then capped with a rubber septum and brought out of the box. The flask was blanketed under static N_2 through a Schlenk line, and to this flask was then added 20 mL dichloroethane (DCE) via syringe. Separately, norbornadiene (1.84 mL, 18.0 mmol) and the alkyne ester (1.14 mL, 9.00 mmol) were dissolved in 60 mL DCE; after dissolution, the solution was transferred to the solution of the catalyst in DCE. This mixture was heated at 55 °C for 16 h under N_2. After 16 h, the reaction was cooled to room temperature and concentrated in vacuo to give a yellow–brown oil. Column chromatography using 5% ethyl acetate in hexanes (R_f = 0.55) gave 939 mg (47.5%) of light yellow oil **4d**. ^{1}H NMR (500 MHz, $CDCl_3$) δ: 5.97 (dd, J = 3.0 Hz, 1H), 5.93 (dd, J = 3.0 Hz, 1H), 3.60 (s, 3H), 2.80 (s, 1H),

2.76 (s, 1H), 2.38 (m, 2H), 2.15 (m, 2H), 2.01 (dd, *J* = 2.0 Hz, 1H), 1.75 (m, 2H), 1.56 (m, 1H), 1.48 (m, 1H), 1.38 (m, 1H), 1.33 (m, 1H). ^{13}C NMR (500 MHz, $CDCl_3$) δ: 173.9, 137.2, 135.4, 86.2, 78.5, 51.6, 49.4, 46.7, 41.9, 34.9, 32.9, 28.9, 24.4, 18.4. HRMS (CI+) *m/z* calcd. for $C_{14}H_{18}O_2$ ($[M]^+$) 218.1307, found 218.9856.

b) *Synthesis of norbornene carboxylic acid **4e**.*

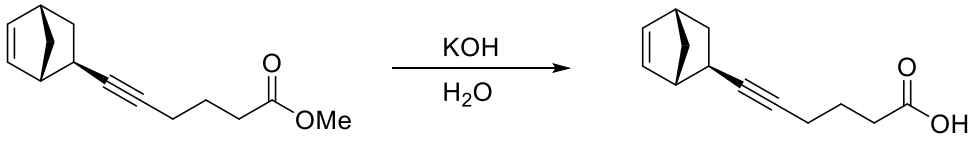

4d **4e**

Potassium hydroxide (797 mg, 14.2 mmol) was added to a round bottom flask and dissolved in deionized water (15.2 mL), affording a 1.0 M solution of KOH in water. Methanol (15.2 mL) was then added to the solution, followed by ester **4d**. The reaction was stirred open to air for 24 h. When the reaction was over, hydrochloric acid (40. mL, 1.0 M) was added to the flask, which immediately resulted in a precipitate. The solution was extracted with 3×30 mL dichloromethane. The organic layer was dried over magnesium sulfate, filtered and concentrated in vacuo to give a viscous light yellow oil. This oil was concentrated overnight under high vacuum on a Schlenk line to give 704 mg (80.4 %) of carboxylic acid **4e**. ^{1}H NMR (500 MHz, $CDCl_3$) δ: 6.04 (dd, *J* = 2.9 Hz, 1H), 6.00 (dd, *J* = 2.9 Hz, 1H), 3.67 (s, 1H), 2.87 (s, 1H), 2.84 (s, 1H), 2.43 (t, *J* = 7.5 Hz, 2H), 2.24 (t, *J* = 2.2 Hz, 2H), 2.08 (ddd, *J* = 2.0 Hz, 1H), 1.80 (m, 1H), 1.59 (m, 1H), 1.55 (m, 1H), 1.44 (m, 2H). ^{13}C NMR (500 MHz, $CDCl_3$) δ: 180.2, 137.2, 135.4, 86.4, 78.3, 49.3, 46.7, 41.9, 34.9, 32.9, 28.9, 24.0, 18.3. HRMS (ES+) *m/z* calcd. for $C_{13}H_{15}N_2$ ($[M–H+2Na]^+$) 249.0867, found 249.0866.

c) *Synthesis of norbornene BODIPY probe molecule **4b**.*

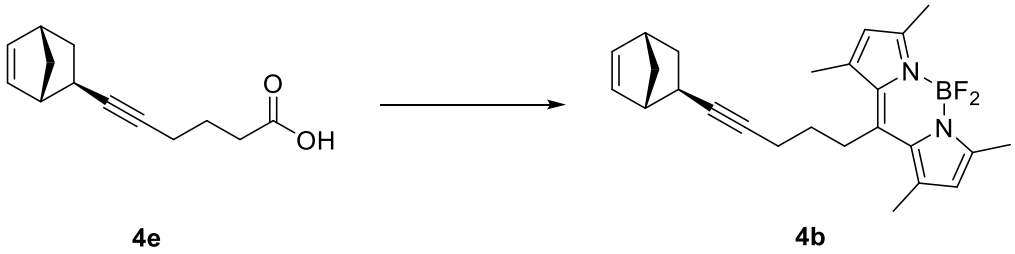

4e **4b**

An oven-dried 100 mL round bottom flask was charged with **4e** (704 mg, 3.45 mmol) and a stir bar, capped with a septum, and placed under a dynamic nitrogen atmosphere. Dry CH_2Cl_2 (25 mL) and DMF (used as received, 0.010 mL, 0.013 mmol) were added to dissolve **4e**, and the solution was stirred. Oxalyl chloride (0.326 mL, 3.80 mmol) was added dropwise over 1 min via syringe to the solution, resulting in a slow evolution of gas. After stirring the solution at room temperature for 1 h, the solution was concentrated in vacuo via rotary evaporation to yield a pale yellow oil, then further concentrated via a high vacuum line for 1 h to remove excess oxalyl chloride.

Using Schlenk techniques, the resulting acid chloride was redissolved in dry CH_2Cl_2 (25 mL). Phosphorus oxychloride (0.355 mL, 3.80 mmol) was added via syringe through a septum to this solution, followed by the addition of 2,4-dimethylpyrrole (0.889 mL, 8.63 mmol) dropwise via syringe over 1 min. The septum was removed, and a reflux condenser, equipped with a septum and under dynamic nitrogen, was immediately fitted onto the flask. The solution was stirred and heated at reflux for 3 h. After cooling to room temperature, the solution was concentrated in vacuo, layered with hexanes (70 mL) to remove impurities, and stored overnight at –35 °C. After decanting the hexanes, the remaining residue was concentrated under high vacuum for 1 h before being dissolved in dry toluene (30 mL). This solution was then treated with 1,8-diazabicyclo[5.4.0]undec-7-ene (0.772 mL, 5.18 mmol) and stirred at 80 °C for 1 h. Boron

trifluoride dimethyletherate (0.425 mL, 4.62 mmol) was added to the solution via syringe, and the mixture was stirred at 80 °C for 1 h, resulting in a deep red solution. The solution was cooled to room temperature and washed with water (3 × 50 mL) and brine (3 × 50 mL). The organic layer was dried over sodium sulfate, filtered with filter paper, and concentrated in vacuo to yield a deep-colored red–green liquid. The resulting liquid was purified by silica gel flash column chromatography using an elution of 50% CH_2Cl_2 in hexanes (R_f = 0.35) and concentrated in vacuo to give a bright orange solid. The compound was then repurified using the same purification method, followed by removal of the volatiles under high vacuum overnight to give 145 mg (10.3%) of **4b** as an intensely colored bright orange solid. ^{1}H NMR (500 MHz, $CDCl_3$) δ: 6.03 (m, 4H), 3.07 (m, 2H), 2.90 (s, 1H), 2.85 (s, 1H), 2.51 (s, 6H), 2.45 (s, 6H), 2.39 (m, 2H), 2.11 (dd, *J* = 2.4 Hz, 1H), 1.79 (m, 2H), 1.61 (m, 1H), 1.53 (m, 1H), 1.46 (m, 2H). ^{13}C NMR (500 MHz, $CDCl_3$) δ: 154.0, 145.9, 140.4, 137.3, 135.3, 131.5, 121.7, 86.7, 78.2, 49.2, 46.8, 41.9, 34.7, 30.8, 28.9, 27.7, 19.6, 16.7, 14.5. HRMS (ES+) *m/z* calcd. for $C_{25}H_{29}N_2BF_2N_2$ ($[M+Na]^+$) 429.2294, found 429.2310.

Following the initial purification of probe **4b**, pentane was added to the sample, which was then triturated, followed by removal of the volatiles under high vacuum overnight. Analytically pure probe **4b** was thus obtained. The two samples produced identical results by microscopy.

d) *Synthesis of control probe **4c**.*

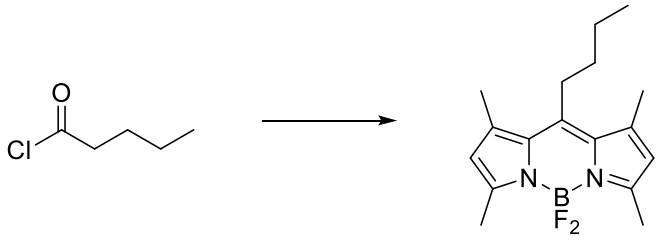

4c

Our group has previously synthesized control probe **4c**, the characterization data[27] of which is reproduced here for convenience and clarity. ^{1}H NMR (500 MHz, $CDCl_3$) δ: 6.05 (s, 2H), 2.96–2.90 (m, 2H), 2.51 (s, 6H), 2.41 (s, 6H), 1.66–1.58 (m, 2H), 1.52 (sextet, J = 8 Hz, 2H), 0.99 (t, J = 8 Hz, 3H). ^{13}C NMR (126 MHz, $CDCl_3$) δ: 153.8, 146.9, 140.4, 131.6, 121.7, 33.9, 28.2, 23.6, 14.6 (t, $J_{C–F}$ = 3 Hz), 13.9. HRMS (ESI+) *m/z* calcd. for $C_{17}H_{23}N_2BF_2$ ($[M+Na]^+$) 327.1823, found 327.1819.

V. Quantum Yield of Norbornene BODIPY Probe **4b**.

Probe **4b** (0.5 mg, 1×10^{-3} mmol) was weighed into a 20 mL glass vial. Spectrophotometric grade heptane (1.0 mL) was added to the vial via syringe, and the solution was sonicated for 1 h to fully dissolve the compound. This afforded a solution of 1×10^{-3} M **4b** in heptane, which was green-orange in appearance. Serial dilution using this 1×10^{-3} M stock solution, a 10 µL gastight syringe (Hamilton Company), and heptane allowed for the preparation of 0.5 µM **4b** in spectrophotometric heptane, which was faintly green in appearance.

To prepare **4b** for fluorescence measurements, drops of the 0.5 µM solution were added via plastic pipette to cuvettes, then filled to the indicated line with spectrophotometric grade heptane. The first cuvette contained 1 drop of the 0.5 µM solution of **4b**, the second contained

2 drops of the 0.5 µM solution, the third contained 3 drops of the 0.5 µM solution, the fourth contained 4 drops of the 0.5 µM solution, and the fifth contained 5 drops of the 0.5 µM solution. All resulting solutions were clear and colorless.

After zeroing the spectrophotometer, the absorption and excitation/emission spectra were recorded for each cuvette, with λ_{ex} = 488 nm and λ_{em} = 508 nm. A plot of the integrated emission vs. absorbance was generated, yielding a linear graph of the data (Figure 4.5). Fluorescein in 0.1 M NaOH (Φ=0.925) and Rhodamine 6G in EtOH (Φ=0.95) were used as standards.[25,46] The quantum yield of probe **4b** in heptane is Φ = 0.53.

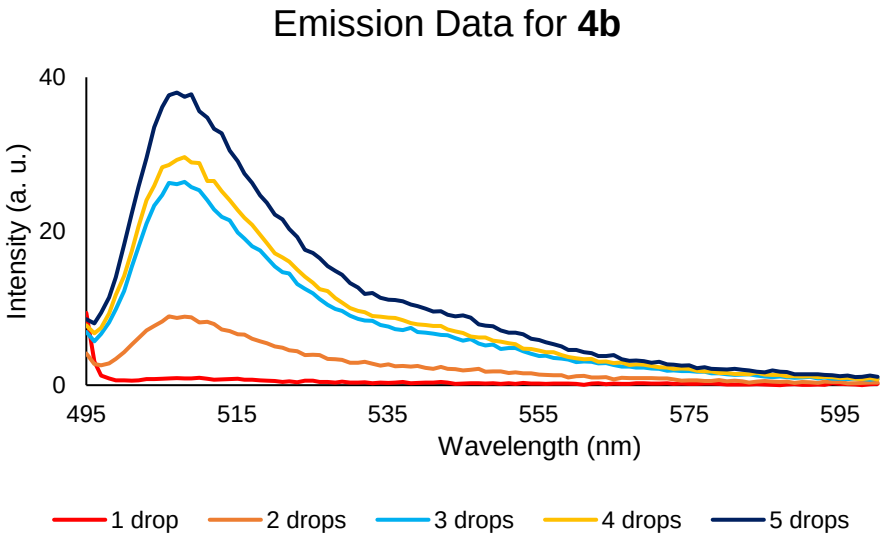

a.

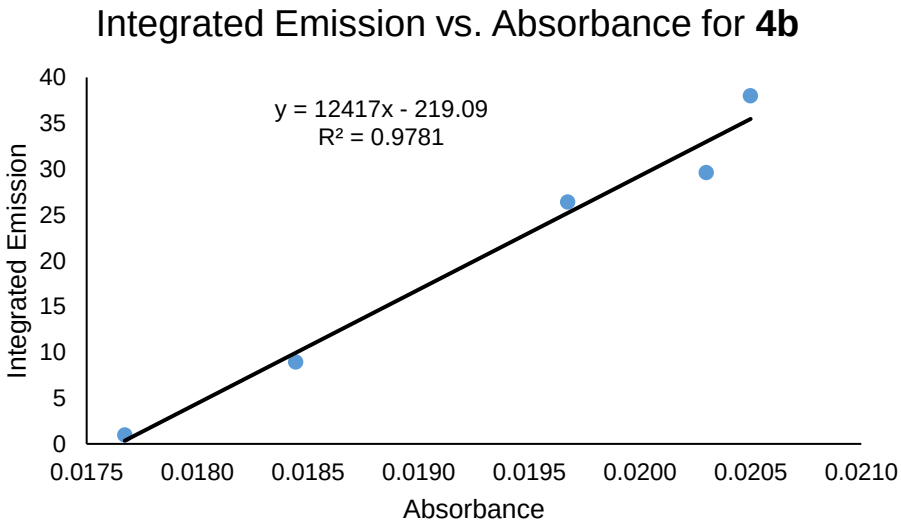

b.

Figure 4.5. **a.** Emission vs. wavelength and **b.** integrated emission vs. absorbance plots of **4b** in heptane.

VI. Sample Preparation

a) *Experiment 1. Preparation of catalyst **4a** for fluorescence microscopy*. In a nitrogen filled glove box, catalyst **4a** (1.5 mg, 1.8×10^{-3} mmol) was weighed out into a 1 dram vial, which was then capped and brought out of the box. Spectrophotometric grade heptane (1.0 mL) was added to the vial via syringe. The resulting mixture was gently swirled, then transferred via the same syringe to a prepared microscopy reaction vial. The solution was a light pink due to some dissolved catalyst, but much of the catalyst remained insoluble and settled on the bottom of the microscope coverslip inside the reaction vial. The microscopy vial was placed on the microscope, and the top of the coverslip was brought into focus, using room light and catalyst crystals to focus.

b) *Experiment 3. Preparation of solutions containing monomer **4b** for microscopy*. Monomer **4b** (0.5 mg, 1×10^{-3} mmol) was weighed into a 20 mL glass vial. Spectrophotometric grade heptane (1.0 mL) was added to the vial via syringe, and the solution was sonicated for 1 h to fully dissolve the compound. This afforded a solution of 1×10^{-3} M **4b** in heptane, which was green-orange in appearance. Serial dilution using this 1×10^{-3} M stock solution, a 10 µL gastight syringe (Hamilton Company), and heptane allowed for the preparation of 1 nM and 1 pM solutions of **4b** in heptane. The solutions prepared via serial dilution were clear and colorless in appearance.

VII. Image Acquisition of Polymerization Activity Involving 4b via In Operando Fluorescence Microscopy

*a) Experiment 1. Co-addition of commercial norbornene and **4b** at 0.2 nM.* In a 1 dram vial, norbornene (0.6 mg, 6×10^{-6} mol) was weighed out and dissolved in a solution of 1 nM **4b** in heptane (0.25 mL, 3×10^{-13} mol), added via syringe. This solution was taken up into the same syringe, then added all at once to the mixture of catalyst **4a** in heptane prepared according to the

process described in Section VI, yielding a final solution volume of 1.25 mL. The resultant concentration of norbornene was 0.015 M, and the resultant concentration of probe **4b** was 0.2 nM. Immediately after the solution was added, the sample was focused in TIRF, and video acquisition of the sample began (Section III). The stage was not moved after the sample was focused on the coverslip.

As soon as the video acquisition of the sample began and the sample was focused in TIRF, bright green round polymer spheres were immediately visible on the surface of the glass coverslip. Over time, more of these green spheres precipitated out of solution. The size of these spheres varied, though those that precipitated out of solution at later time points were generally larger than those that precipitated at earlier time points (Figure 4.6).

On the surface of the coverslip, which was observed 1 min after addition of the monomer solution to catalyst **4a**, some polymers that had previously precipitated out of solution increased in diameter as time progressed. It was further noticed that these polymers also became brighter as they increased in diameter. Time trace data of these locations revealed a fluorescence intensity increase consistent with the insertion of **4b** into the growing polymer (examples, Figure 4.6; 19 additional examples, Figure 4.7. The abrupt increase, when present, corresponds to the initial precipitation event. The increase in brightness after this precipitation event denotes continued polymerization after precipitation). Individual insertion events were not resolved at this higher probe concentration.

Raw Data

a.

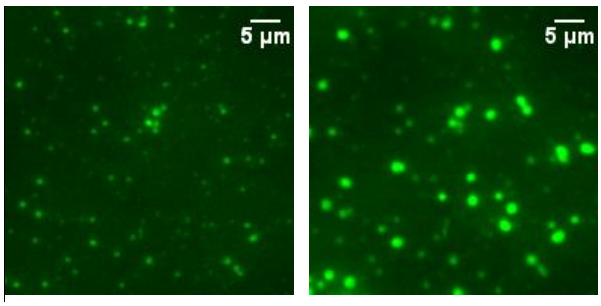

Standardized min/max/gamma adjusted data

b.

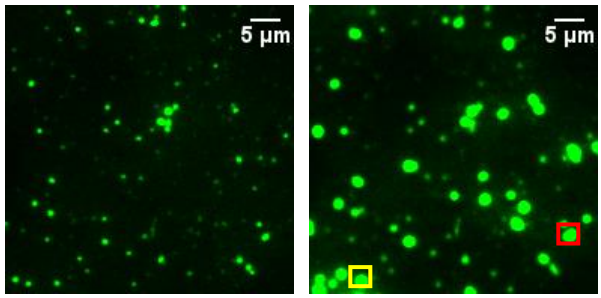

c.

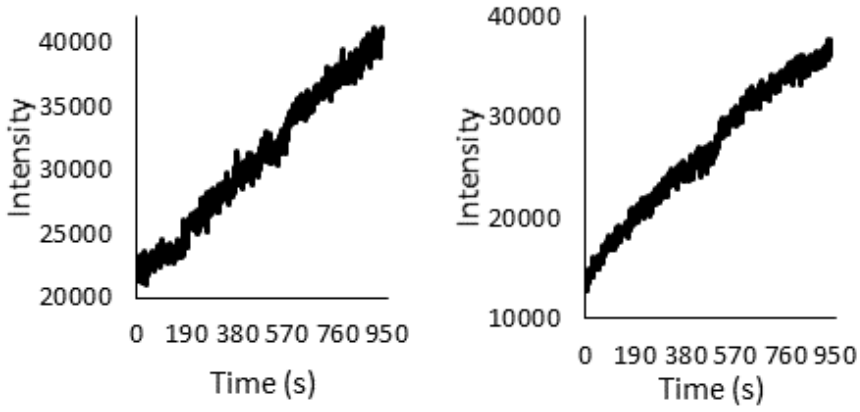

Figure 4.6. Raw and standardized data showing incorporation of **4b** at 0.2 nM by molecular catalysts into polynorbornene. **a.** raw data images and **b.** images set at standard minimum/maximum/gamma values (Section III) of polymerization of norbornene and **4b** (at 0.2 nM) at t = 1 min (a & b, left image) and 15 min 50 s (a & b, right image). **c.** Time trace data examples of representative areas of polymerization. The time trace on the left corresponds to the area in the red box, and the time trace on the right corresponds to the area in the yellow box.

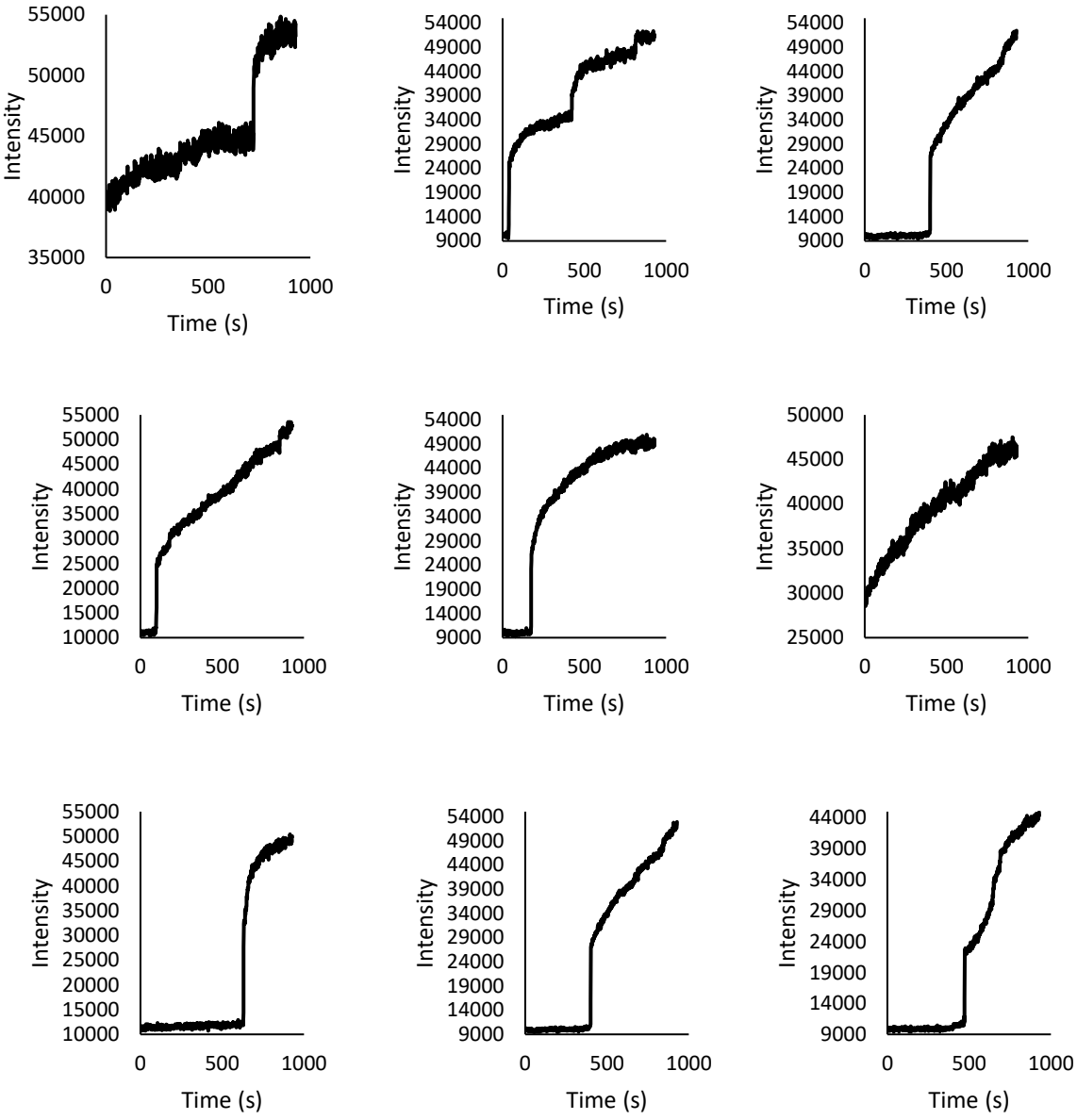
Intensity
Time (s)
55000
50000
45000
40000
35000
54000
49000
44000
39000
34000
29000
24000
19000
14000
9000
50000
45000
40000
35000
30000
25000
20000
15000
10000
0
500
1000

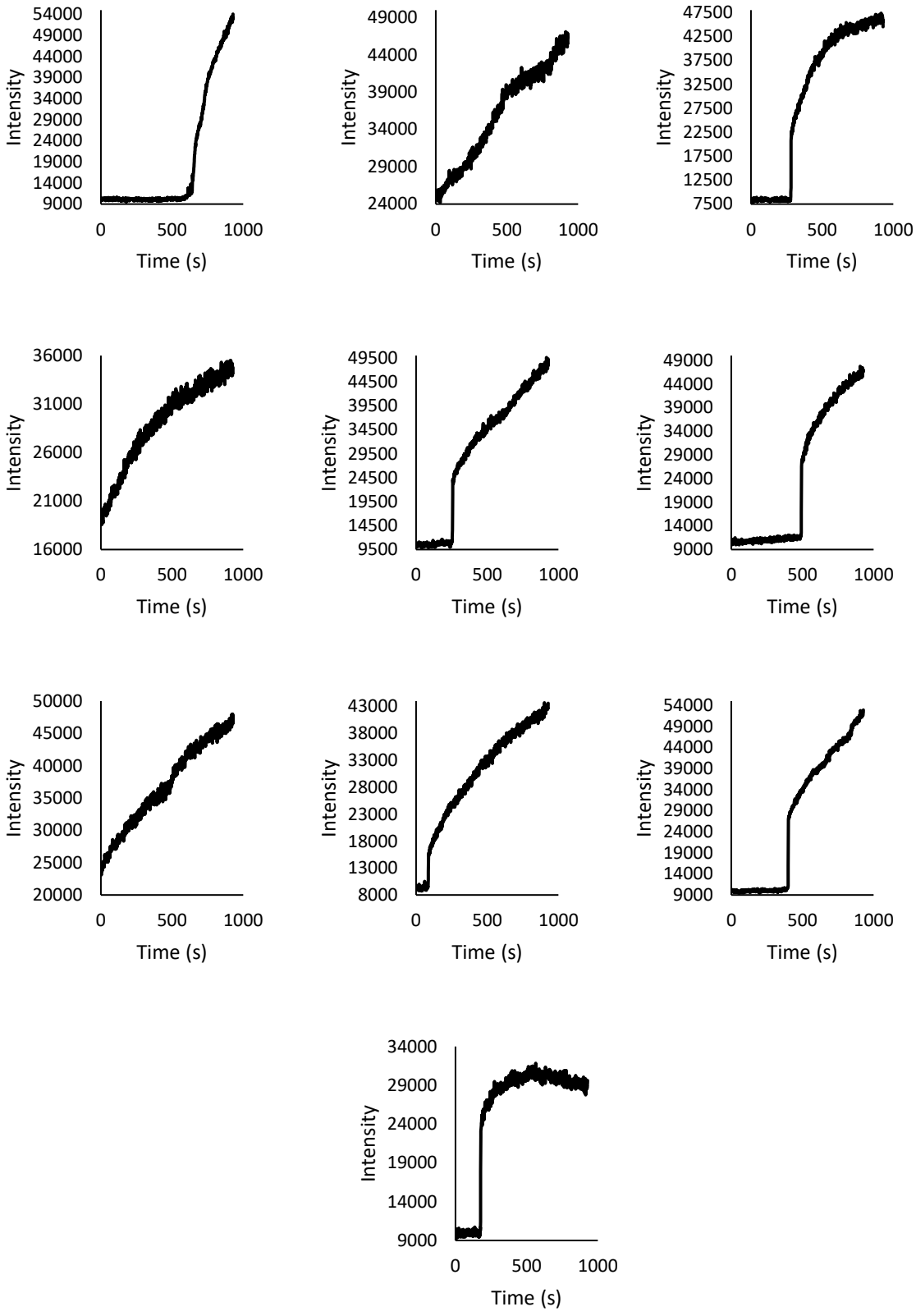

Figure 4.7. Additional examples of polymerization of norbornene and probe **4b** at 0.2 nM.

b) *Experiment 2. Co-addition of commercial norbornene and **4b** at 0.2 pM.* In a 1 dram vial, norbornene (3.0 mg, 3.2×10^{-5} mol) was weighed out and dissolved in a solution of 1 pM **4b** in heptane (0.25 mL, 3×10^{-16} mol), added via syringe. This solution was taken up into the same syringe, then added all at once to the mixture of catalyst **4a** in heptane prepared according to the process described in Section V, yielding a final solution volume of 1.25 mL. The resultant concentration of norbornene was 0.026 M, and the resultant concentration of probe **4b** was 0.2 pM. Immediately after the solution was added, the sample was focused in TIRF, and video acquisition of the sample began. The stage was not moved once the sample was focused on the coverslip.

As soon as the video acquisition of the sample began and the sample was focused in TIRF, polymer regions with some green regions were visible on the surface of the glass coverslip (Figure 4.8). These regions were much dimmer than those generated using 0.2 nM **4b**, and they were no longer exclusively spherical. As time progressed, some polymers that had previously precipitated out of solution showed bright green flickering events, while others became brighter green. The flickering events became more pronounced at $t \approx 7$ min, and multiple polymers had these resolvable flickering events. When time trace data of some of these flickering regions was analyzed, quantized fluorescence intensity increases were visible, some of which lasted for multiple frames, before the corresponding quantized fluorescence intensity decreases occurred. These quantized events are consistent with the detection of single fluorophores.[33] Thus, individual chemical reaction events of **4b** within the growing polymer were observed.

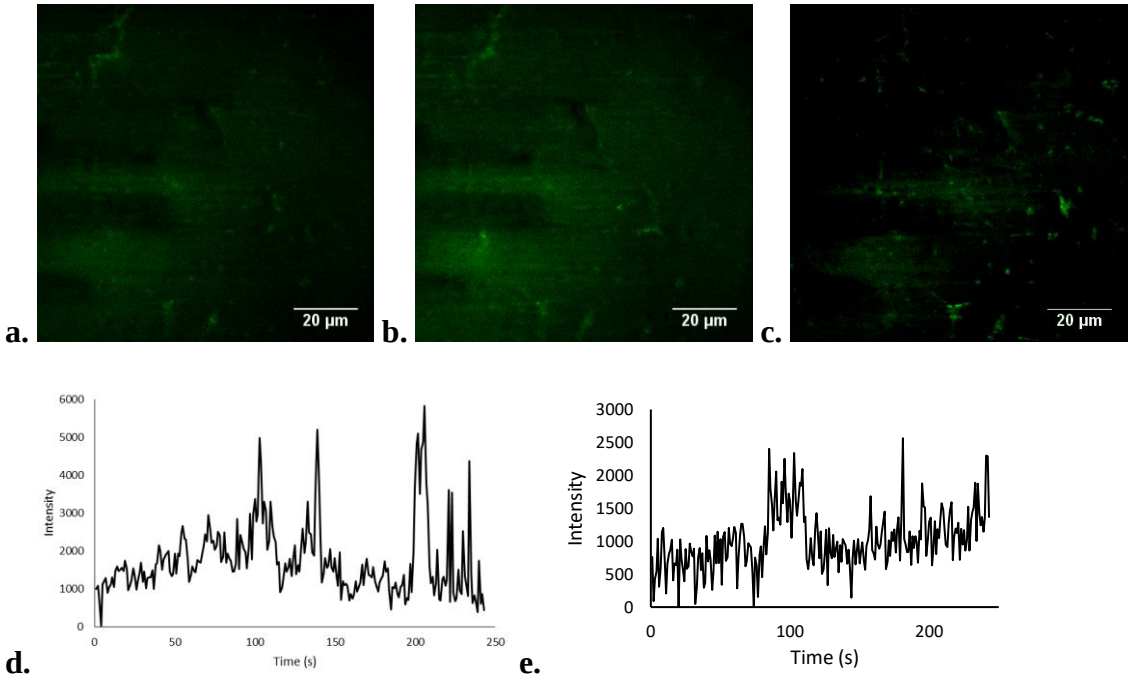

Figure 4.8. Widespread incorporation of **4b** at 0.2 pM by molecular catalysts into polynorbornene. **a.** initial, **b.** final, and **c.** composite full screen images of polymerization of norbornene with **4b** (at 1 pM) at t = 7 min (**a.**) and t = 12 min (**b.**). **d.** time trace data of a representative area of polymerization. **e.** additional example of representative area of polymerization.

At t = 28 min, the sample was moved to a new region on the surface of the coverslip. Video acquisition of this region showed green previously precipitated polymers distributed across the coverslip surface (Figure 4.9). As time progressed in the video acquisition, these polymers exhibited bright green flashes across their surfaces. These bright green flashes are consistent with individual insertion events of **4b** into the polymers.

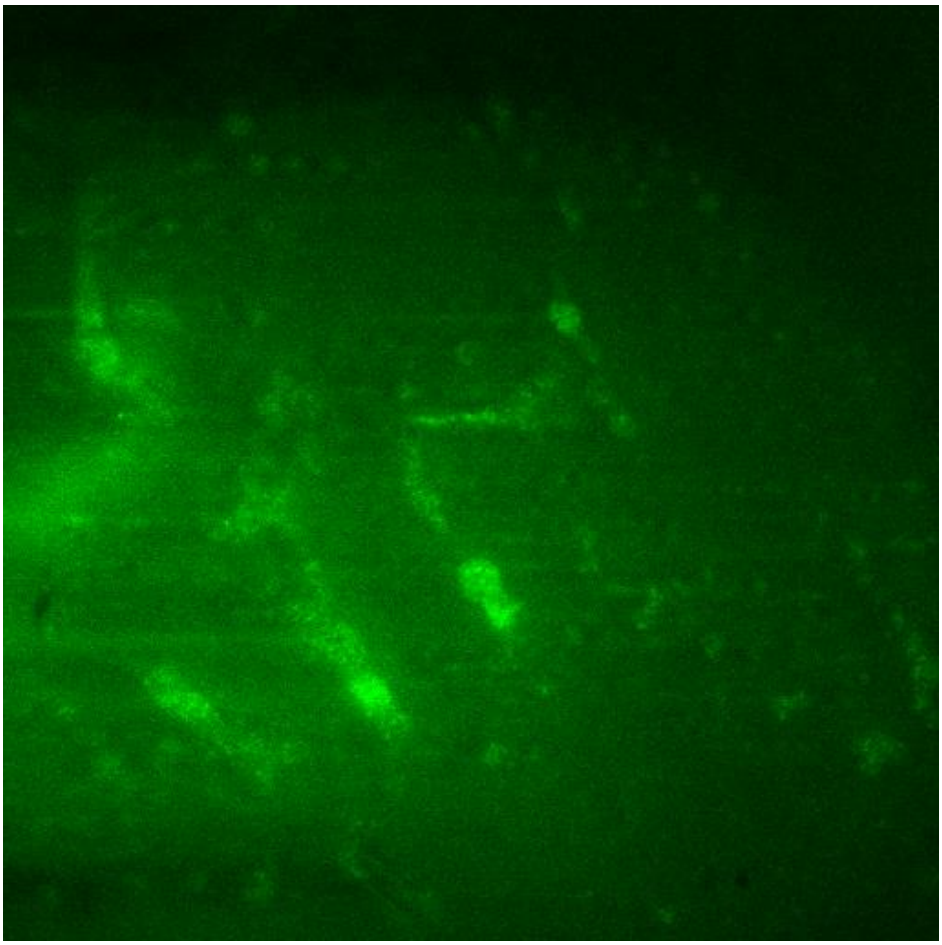

Figure 4.9. Full-frame image of polymers with incorporated probe **4b** at 0.2 pM at t = 28 min. Size = 137 μm x 137 μm^2. This image is representative of the widespread fluorescent green polymers across the sample surface.

c) *Experiment 3. Addition of commercial norbornene, then fluorophore-tagged **4b** at 1 pM.*

Norbornene (3.0 mg, 3.2×10^{-2} mmol) was weighed out into a 1 dram vial and dissolved in spectrophotometric heptane (0.25 mL), added via syringe. The resultant concentration of norbornene following this addition was 0.026 M. The same syringe was used to transfer the resulting solution to the mixture of catalyst **4a** in heptane (Section V), yielding a final solution volume of 1.25 mL. After 5 min, the solution containing any unreacted monomer was removed, leaving the precipitated polymer on the surface of the coverslip. To the reaction vial and precipitated polymer was added a solution of 1 pM **4b** in heptane (0.25 mL, 3×10^{-16} mol);

following this addition, the sample was focused in TIRF, and video acquisition of the sample began (Section III) after t = 6 min. The stage was not moved once the sample was focused on the coverslip.

When video capture began at t = 0, initially the surface of the coverslip was dark with no discernible features. Time t = 0 for the video acquisition and time trace analysis is defined as 13 min after addition of **4b** to precipitated polymer. As time progressed, some regions on the surface displayed flickering activity, which was seen at various time points (Figure 4.10). These polymers never became as bright as polymers when 0.2 nM solutions of **4b** were used, or when 0.2 pM solutions of **4b** were added at the beginning of the reaction. This reaction with **4b** was allowed to progress until t = 17 min after the addition of **4b**. Time trace data showed quantized fluorescence intensity increases, some of which lasted for multiple frames, before the corresponding quantized fluorescence intensity decreases occurred. These quantized events are consistent with the well-established fingerprints of single molecules.[33]

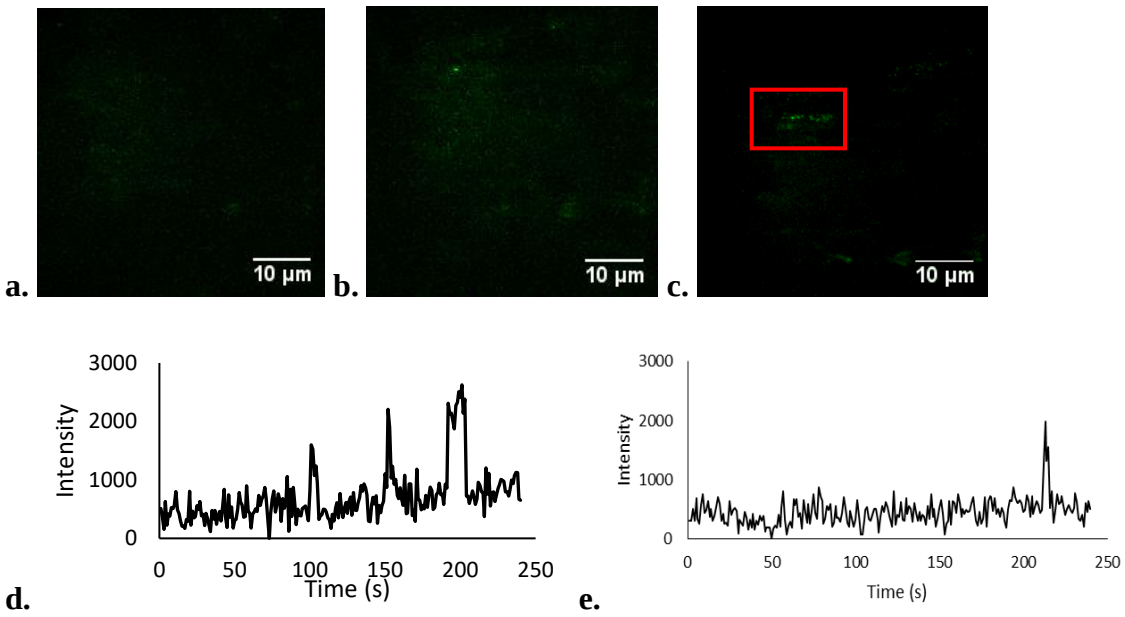

Figure 4.10. Spatiotemporal resolution of incorporation of **4b** at 1 pM by molecular catalysts into polynorbornene. **a.** initial (t = 13 min), **b.** final (t = 17 min), and **c.** composite images of addition of **4b** at 1 pM to precipitated polynorbornene polymers. **d.** time trace of representative area. **e.** second time trace of representative area.

VIII. Gel Permeation Chromatography (GPC) of Polynorbornene

In a nitrogen-filled glove box, catalyst **4a** (1.5 mg, 0.0018 mmol) was weighed out into a pre-tared 1 dram vial. The vial was capped and brought out of the glove box, and to this vial was added spectrophotometric grade heptane (1.0 mL) via syringe. In a separate 1 dram vial, norbornene (3.0 mg, 0.032 mmol) was weighed out and dissolved in spectrophotometric grade heptane (0.25 mL), added via syringe. The second syringe was used to transfer the norbornene solution to the vial containing catalyst **4a** and heptane, and the ROMP reaction was allowed to proceed for 7 min. At 7 min, the mother liquor containing solvent & unreacted monomer was removed from the reaction vial, leaving behind a visible polymer film. To the residual polymer was added dry THF (1.0 mL) via syringe, resulting in an emulsion. This emulsion was then sonicated for 25 min to solubilize all polynorbornene. The resulting solution was filtered through a 0.2 μm PTFE syringe prior to GPC analysis (Figure 4.11), using polystyrene as calibration. M_n = 49976 g/mol. PDI = 2.01.

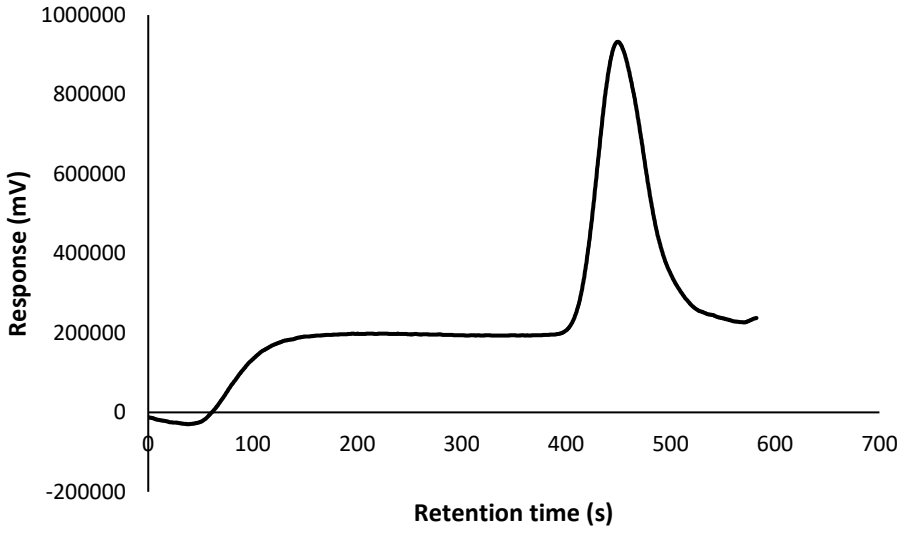

Figure 4.11. Response vs. retention time graph of polynorbornene polymers in THF.

IX. MATLAB Analysis of Full Width at Half Maximum

The modeling program MATLAB was used to analyze the spatial localization and resolution of chemical events with probe **4b** (Section VIIc) by determining the full width at half maximum (fwhm) of the peaks. Signals from a 7 × 7 pixel region were plotted separately in the x- and y-directions, with least absolute resolution (LAR) applied to the peaks[47]. Figure 4.12 shows data and analysis from three example signals. Given the multiple overlapping events from multiple ruthenium catalysts, some signals overlap partially with other signals offset in the *x* or or *y* directions. The fwhm of the peaks were 2.04 ± 0.04 and 2.92 ± 0.56 pixels for the *x*- and *y*-directions, respectively, for the three examples below. These values were compared to single molecule signals of a standard sample of fluorescein recorded on the same microscope (Figure 4.13). The fwhm of fluorescein peaks were found to be 2.40 ± 0.32 and 2.90 ± 0.36 pixels for the *x*- and *y*-directions, respectively. This comparison shows similar point spread functions for the events with probe **4b** and single molecules of a standard sample of fluorescein and is thus further consistent with the detection of single molecule events from probe **4b**.

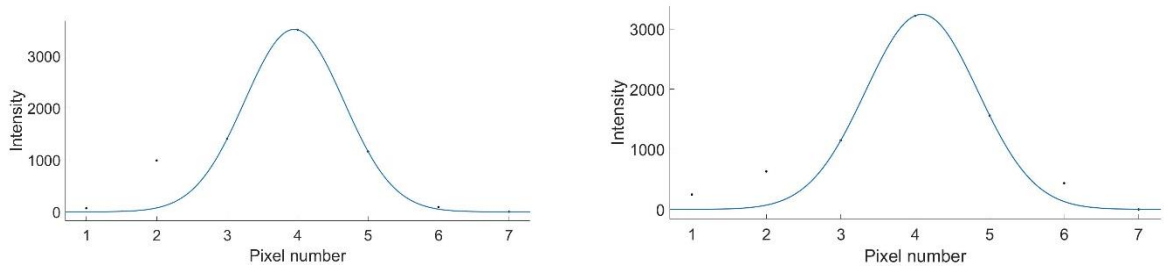

a. x-axis (1) y-axis (1)

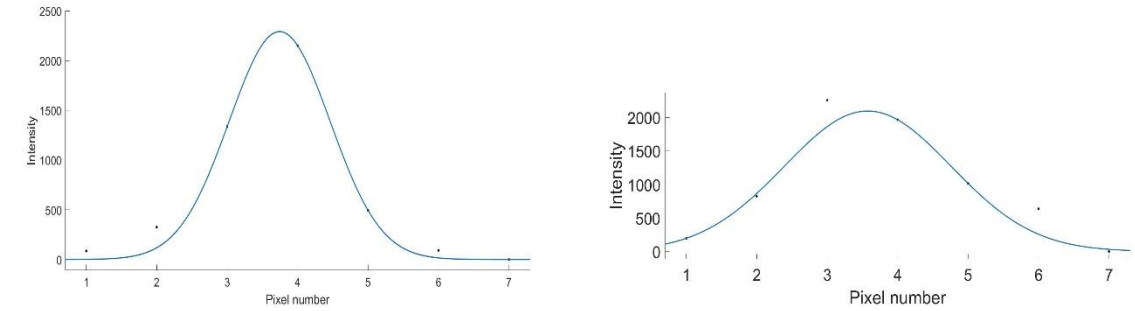

b. x-axis (2) y-axis (2)

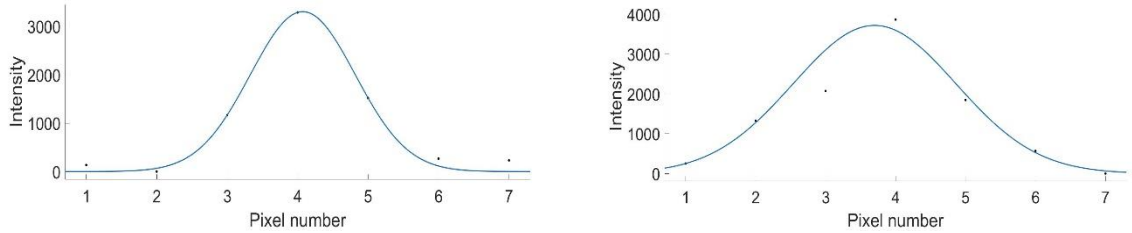

c. x-axis (3) y-axis (3)

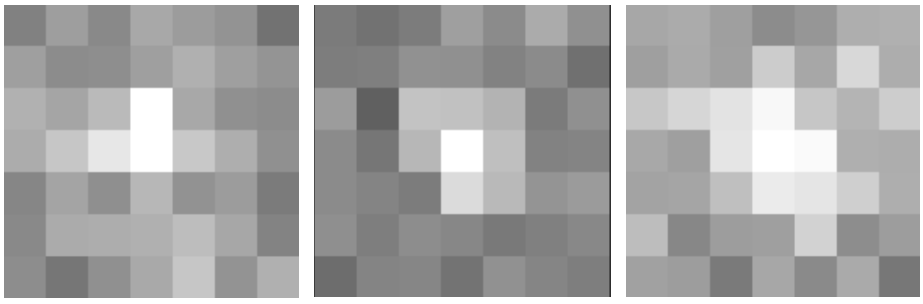

d. (1) (2) (3)

Figure 4.12. MATLAB fitting of single molecules of probe **4b**. **a.-c.** Fitting of fluorescence intensity of single reactions of probe **4b** in the *x* and *y* direction of 7 × 7 pixel sizes, corresponding to width of 1.82 × 1.82 μm^2. **d.** images of pixels fitted in **a.-c.**

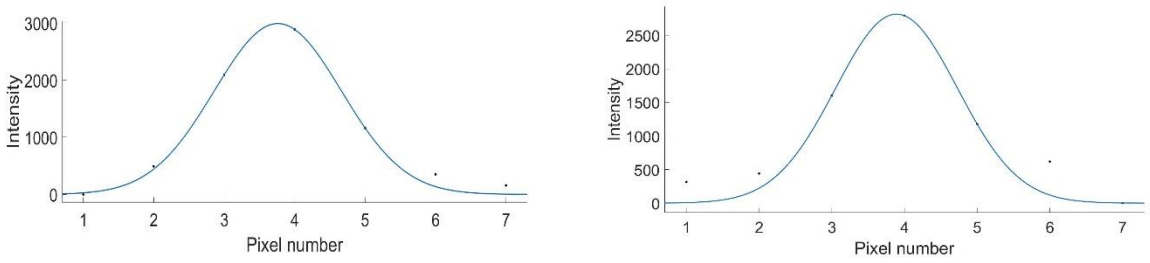

a. x-axis y-axis

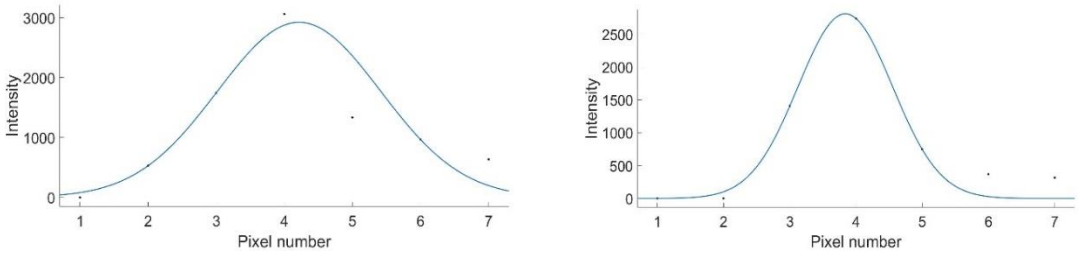

b. x-axis (2) y-axis (2)

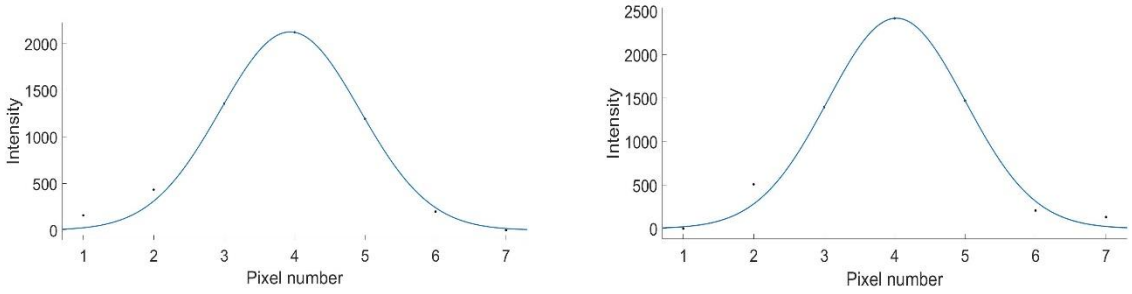

c. x-axis (3) y-axis (3)

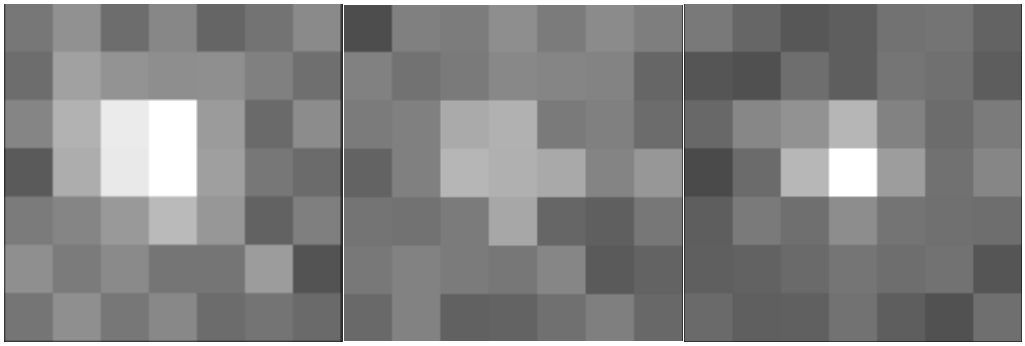

d. (1) (2) (3)

Figure 4.13. MATLAB fitting of single molecules of fluorescein. **a.-c.** Fitting of fluorescence intensity of fluorescein single molecules in the *x* and *y* direction of 7 × 7 pixel sizes, corresponding to width of 1.82 × 1.82 μm^2. **d.** images of pixels fitted in **a.-c.**

X. Control Experiments for Assignment of Fluorescent Regions as Products of Ring-Opening Metathesis Polymerization

a) *Experiment 1. Use of probe **4c** in place of **4b** at 0.2 nM.* Alkyl control probe **4c** (0.5 mg, 1×10^{-3} mmol) was weighed out into a 20 mL glass vial. Spectrophotometric grade heptane (1.0 mL) was added to the vial via syringe, and the solution was sonicated for 1 h to fully dissolve the compound. This afforded a solution of 1×10^{-3} M **4c** in heptane, which was green-orange in appearance. Serial dilution using this 1×10^{-3} M stock solution, a 10 μL gastight syringe (Hamilton Company), and heptane allowed for the preparation of 1 nM **4**c in heptane, which was a clear colorless solution. Probe **4c** has no norbornene unit and therefore cannot participate in ROMP reactions with catalyst **4a**.

In a 1 dram vial, norbornene (0.6 mg, 6×10^{-6} mol) was weighed out and dissolved in a solution of 1 nM **4c** in heptane (0.25 mL, 3×10^{-13} mol), added via syringe. This solution was taken up into the same syringe, then added all at once to the mixture of catalyst **4a** in heptane prepared according to the process described in Section V, yielding a final solution volume of 1.25 mL. The resultant concentration of norbornene was 0.015 M, and the resultant concentration of probe **4c** was 0.2 nM. Immediately after the solution was added, the sample was focused in TIRF, and video acquisition of the sample began (Section III). The stage was not moved after the sample was focused on the coverslip.

On the surface of the coverslip, no fluorescent green regions were observed (Figure 4.14). Therefore, the growth of the fluorescent green polymer is due to chemical incorporation of **4b** into the polymer chain, and is not due to physical uptake of any probes into the polymer.

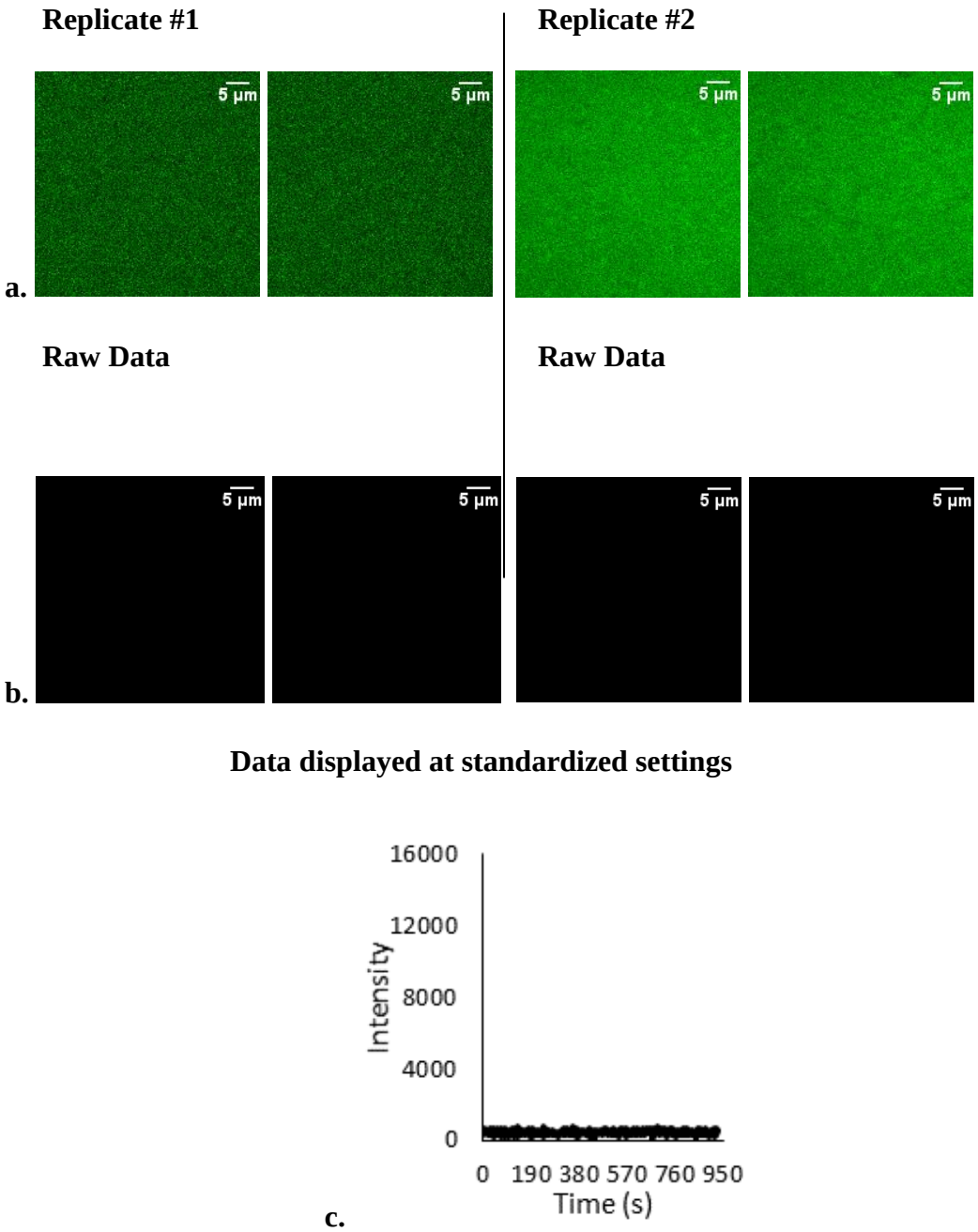

Figure 4.14. Control experiment using probe **4c** in place of **4b** at 0.2 nM. **a.** raw data images and **b.** images set at standard minimum/maximum/gamma values (Section III) of polymerization of norbornene in the presence of **4c** (at 1.0 nM) at t = 1 min (a & b, left image) and 15 min 50 s (a & b, right image). A second run with the same experimental conditions is shown to the right of the vertical line, with data treated identically. **c.** time trace graph of representative area in the images.

b) *Experiment 2. Addition of **4b** to solution in the absence of catalyst **4a**.* A solution of 1 pM **4b** in spectrophotometric grade heptane was prepared (Section V). This solution (0.25 mL)

was added to a microscope reaction vial (Section II) and imaged (Section III). This experimental setup was chosen to determine if the growth of the fluorescent green regions was due to precipitation from solution of probe **4b** in specific locations on the surface of the glass coverslip or due to polymerization. No fluorescent green regions were observed at t = 11 min from the surface of the glass coverslip, where tagged polynorbornene polymers would ordinarily be visible (Figure 4.15). Therefore, the growth of the fluorescent green regions in other data was attributed to ROMP of **4b** at active catalyst centers in the polymers.

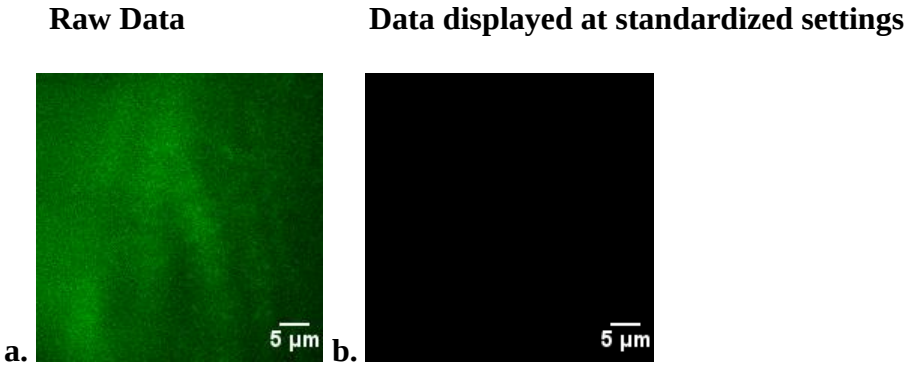

Figure 4.15. Control experiment using probe **4b** in the absence of **4a**. **a.** raw and **b.** images of **4b** displayed at standardized conditions (Section III) in spectrophotometric grade heptane in the absence of catalyst **4a**.

c) *Experiment 3. Use of probe **4c** in place of **4b** at 0.2 pM.* A solution of **4c** in spectrophotometric grade heptane was prepared according to the same process as the 1 nM solution, with an extra dilution to afford 1 pM **4c** in heptane. In a 1 dram vial, norbornene (3.0 mg, 3.2×10^{-5} mol) was weighed out and dissolved in a solution of 1 pM **4c** in heptane (0.25 mL, 3×10^{-16} mol), added via syringe. This solution was taken up into the same syringe, then added all at once to the mixture of catalyst **4a** in heptane prepared according to the process described in Section V, yielding a final solution volume of 1.25 mL. The resultant concentration of norbornene was 0.026 M, and the resultant concentration of probe **4c** was 0.2 pM.

Holding the experimental conditions the same as when **4b** was used, including moving the microscope coverslip to a new region at t = 28 min, no flickering events were observed at any precipitated polymers, nor was there any observable increase in bright green fluorescence intensity (Figure 4.16 at initial and final time point images, Figure 4.17 at t = 28 min). Thus, chemical reaction of the norbornene unit of **4b** is responsible for the intensity increase and growth of the polymer on the surface of the coverslip that was observed in previous data.

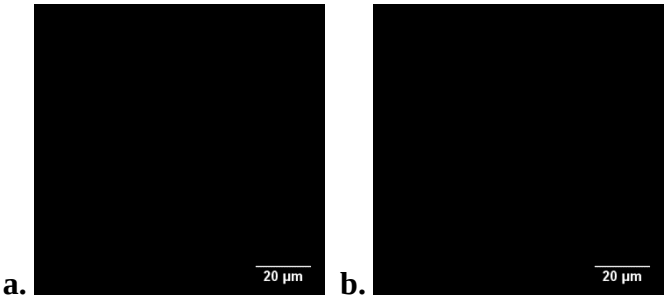

Figure 4.16. Control experiment using probe **4c** in place of **4b** at 0.2 pM. **a.** initial (t = 7 min) and **b.** final (t = 11 min) time point images of the polymerization of norbornene in the presence of **4c** at 0.2 pM, displayed under standardized conditions (Section III).

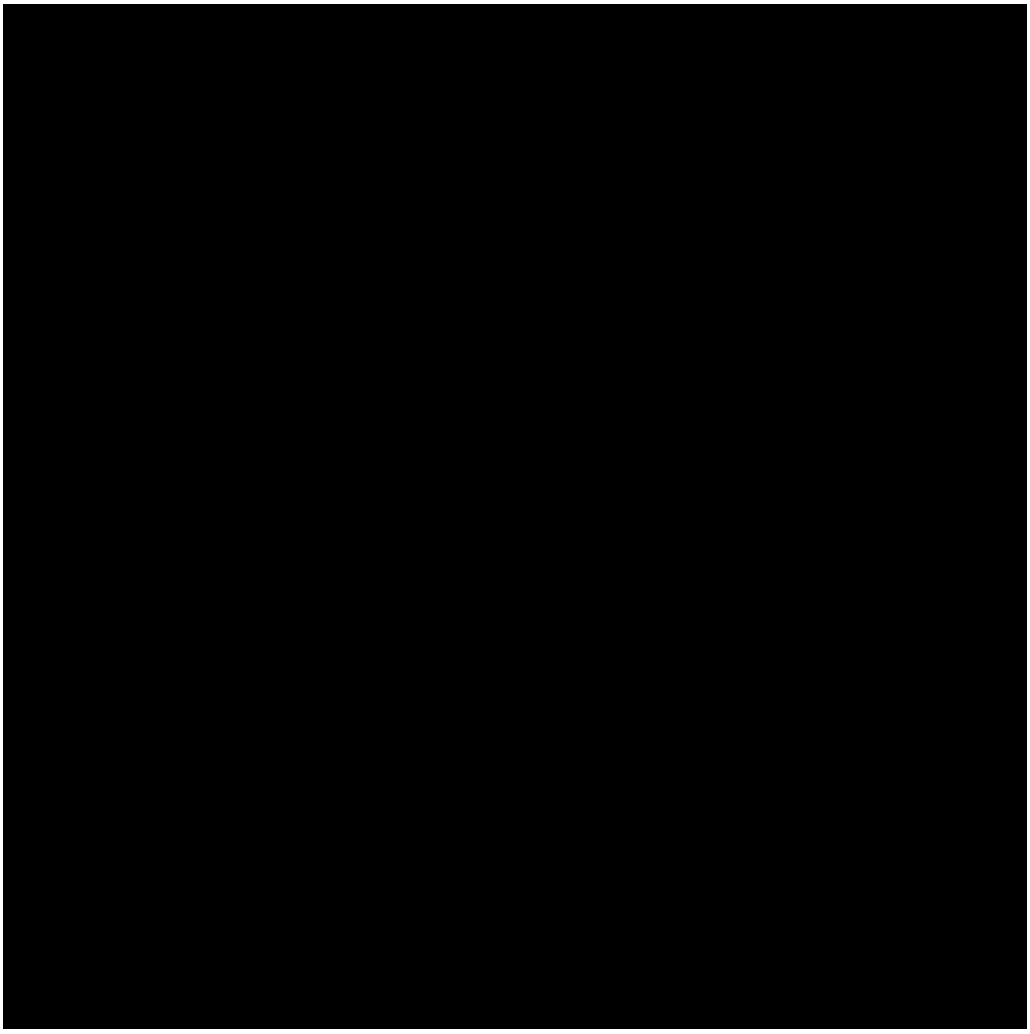

Figure 4.17. Full-frame (137 μm x 137 μm^2) image of polymerization reaction with control probe **4c** at 0.2 pM at *t* = 28 min. This image is representative of the widespread lack of incorporation of fluorescent probe across the slide.

References

(1) Hartwig, J. F. *Organotransition Metal Chemistry: From Bonding to Catalysis*. University Science Books: Sausalito, **2010**, pp. 547–549.
(2) Crabtree, R. H. *The Organometallic Chemistry of the Transition Metals*, 5th ed.; John Wiley & Sons, Inc.: Hoboken, **2009**, p. 380.
(3) Esfandiari, N. M.; Blum, S. A. *J. Am. Chem. Soc.* **2011**, *133*, 18145**–**18147.
(4) Hodgson, G. K.; Impellizzeri, S.; Scaiano, J. C. *Chem. Sci.* **2016**, *7*, 1314–1321.
(5) Mol, J. C. *J. Mol. Catal. A: Chem*. **2004**, *213*, 39–45.
(6) Bielawski, C. W.; Grubbs, R. H. *Angew. Chem. Int. Ed.* **2000**, *39*, 2903–2906.
(7) Weiss, S. *Science* **1999**, *283*, 1676–1683.
(8) Tian, H.; Fürstenberg, A.; Huber, T. *Chem. Rev.* **2017**, *117*, 186–245.
(9) Roeffaers, M. B. J.; Sels, B. F.; Uji-i, H.; De Schryver, F. C.; Jacobs, P. A.; De Vos, D. E.; Hofkens, J. *Nature* **2006**, *439*, 572**–**575.

(10) Roeffaers, M. B. J.; De Cremer, G.; Libeert, J.; Ameloot, R.; Dedecker, P.; Bons, A.-J.; Bückins, M.; Martens, J. A.; Sels, B. F.; De Vos, D. E.; Hofkens, J. *Angew. Chem. Int. Ed.* **2009**, *48*, 9285–9289.
(11) Kubarev, A. V.; Janssen, K. P. F.; Roeffaers, M. B. J. *ChemCatChem* **2015**, *7*, 3646–3650.
(12) Ristanović, Z.; Hofmann, J. P.; De Cremer, G.; Kubarev, A. V.; Rohnke, M.; Meirer, F.; Hofkens, J.; Roeffaers, M. B. J.; Weckhuysen, B. M. *J. Am. Chem. Soc.* **2015**, *137*, 6559–6568.
(13)Weckhuysen, B. M. *Angew. Chem. Int. Ed.* **2009**, *48*, 4910**–**4943.
(14) Buurmans, I. L. C.; Weckhuysen, B. M. *Nat. Chem.* **2012**, *4*, 873–886.
(15) Ristanović, Z.; Kubarev, A. V.; Hofkens, J.; Roeffaers, M. B. J.; Weckhuysen, B. M. *J. Am. Chem. Soc.* **2016**, *138*, 13586–13596.
(16) Ristanović, Z.; Kerssens, M. M.; Kubarev, A. V.; Hendriks, F. C.; Dedecker, P.; Hofkens, J.; Roeffaers, M. B. J.; Weckhuysen, B. M. *Angew. Chem. Int. Ed.* **2015**, *54*, 1836–1840.
(17) Wöll, D.; Uji-i, H.; Schnitzler, T.; Hotta, J.; Dedecker, P.; Herrmann, A.; De Schryver, F. C.; Müllen, K.; Hofkens, J. *Angew. Chem. Int. Ed.* **2008**, *47*, 783–787.
(18) Sambur, J. B.; Chen, T.-Y.; Choudhary, E.; Chen, G.; Nissen, E. J.; Thomas, E. M.; Zou, N.; Chen, P. *Nature* **2016**, *530*, 77–80.
(19) Chen, P.; Zhou, X.; Andoy, N. M.; Han, K.-S.; Choudhary, E.; Zou, N.; Chen, G.; Shen, H. *Chem. Soc. Rev.* **2014**, *43*, 1107**–**1117.
(20) Andoy, N. M.; Zhou, X.; Choudhary, E.; Shen, H.; Chen, P. *J. Am. Chem. Soc.* **2013**, *135*, 1845–1852.
(21) Zhou, X.; Xu, W.; Liu, G.; Panda, D.; Chen, P. *J. Am. Chem. Soc.* **2009**, *132*, 138–146.
(22) Blum, S. A. *Phys. Chem. Chem. Phys.* **2014**, *16*, 16333**–**16339.
(23) Cordes, T.; Blum, S. A. *Nat. Chem.* **2013**, *5*, 993–999.
(24) Feng, C.; Cunningham, D. W.; Easter, Q. T.; Blum, S. A. *J. Am. Chem. Soc.* **2016**, *138*, 11156–11159.
(25) Feng, C.; Easter, Q. T.; Blum, S. A. *Organometallics* **2017**, *36*, 2389**–**2396.
(26) Hensle, E. M.; Blum, S. A. *J. Am. Chem. Soc.* **2013**, *135*, 12324**–**12328.
(27) Esfandiari, N. M.; Wang, Y.; Bass, J. Y.; Cornell, T. P.; Otte, D. A. L.; Cheng, M. H.; Hemminger, J. C.; Mcintire, T. M.; Mandelshtam, V. A.; Blum, S. A. *J. Am. Chem. Soc.* **2010**, *132*, 15167–15169.
(28) Esfandiari, N. M.; Wang, Y.; Mcintire, T. M.; Blum, S. A. *Organometallics* **2010**, *30*, 2901–2907.
(29) Esfandiari, N. M.; Wang, Y.; Bass, J. Y.; Blum, S. A. *Inorg. Chem.* **2011**, *50*, 9201–9203.
(30) Canham, S. M.; Bass, J. Y.; Navarro, O.; Lim, S.-G.; Das, N.; Blum, S. A. *Organometallics* **2008**, *27*, 2172–2175.
(31) Easter, Q. T.; Trauschke, V.; Blum, S. A. *ACS Catal.* **2015**, *5*, 2290–2295.
(32) Ng, J. D.; Upadhyay, S. P.; Marquard, A. N.; Lupo, K. M.; Hinton, D. A.; Padilla, N. A.; Bates, D. M.; Goldsmith, R. H. *J. Am. Chem. Soc.* **2016**, *138*, 3876–3883.
(33) Lakowicz, J. R. *Principles of Fluorescence Spectroscopy*, 3rd ed.; Springer: New York, **2006**.
(34) Decan, M. R.; Scaiano, J. C. *J. Phys. Chem. Lett.* **2015**, *6*, 4049–4053.
(35) Tachikawa, T.; Ohsaka, T.; Bian, Z.; Majima, T. *J. Phys. Chem. C* **2013**, *117*, 11219–11228.
(36) Tachikawa, T.; Cui, S.-C.; Tojo, S.; Fujitsuka, M.; Majima, T. *Chem. Phys. Lett.* **2007**, *443*, 313–318.
(37) Tachikawa, T.; Majima, T. *Langmuir* **2012**, *28*, 8933–8943.
(38) Rybina, A.; Lang, C.; Wirtz, M.; Gruβmayer, K.; Kurz, A.; Maier, F.; Schmitt, A.; Trapp, O.; Jung, G.; Herten, D.-P. *Angew. Chem. Int. Ed.* **2013**, *52*, 6322–6325.

(39) Wirtz, M.; Grüter, A.; Heib, F.; Hugh, V.; Zapp, J.; Herten, D.-P.; Schmitt, M.; Jung, G. *Methods Appl. Fluoresc.* **2015**, *3*, 044001.
(40) Ameloot, R.; Roeffaers, M.; Baruah, M.; De Cremer, G.; Sels, B.; De Vos, D.; Hofkens, J. *Photochem. Photobiol. Sci.* **2009**, *8*, 453–456.
(41) Velvadapu, V.; Paul, T.; Wagh, B.; Klepacki, D.; Guvench, O.; MacKerell, A., Jr.; Andrade, R. B. *ACS Med. Chem. Lett.* **2011**, *2*, 68–72.
(42) Alcaide, B.; Almendros, P.; Luna, A. *Chem. Rev.* **2009**, *109*, 3817–3858.
(43) Yoshida, K.; Shishikura, Y.; Takahashi, H.; Imamoto, T. *Org. Lett.* **2008**, *10*, 2777–2780.
(44) Katayama, H.; Urushima, H.; Nishioka, T.; Wada, C.; Nagao, M.; Ozawa, F. *Angew. Chem. Int. Ed.* **2000**, *39*, 4513–4515.
(45) Tenaglia, A.; Giordano, L.; Buono, G. *Org. Lett.* **2006**, *8*, 4315–4318.
(46) Williams, A. T. R.; Winfield, S. A.; Miller, J. N. *Analyst* **1983**, *108*, 1067–1071.
(47) MacGillavry, H. D.; Blanpied, T. A. *Curr. Protoc. Neurosci.* **2013**, 2.20.1–2.20.19.

Chapter 5

Evidence for Dynamic Chemical Kinetics at Individual Molecular Ruthenium Catalysts

Abstract: Catalytic cycles are typically depicted as possessing time-invariant steps with fixed rates. Yet the true behavior of individual catalysts with respect to time is unknown, hidden by the ensemble averaging inherent to bulk measurements. Evidence is presented for variable chemical kinetics at individual catalysts, with a focus on ring-opening metathesis polymerization catalyzed by the second-generation Grubbs' ruthenium catalyst. Fluorescence microscopy is used to probe the chemical kinetics of the reaction because the technique possesses sufficient sensitivity for the detection of single chemical reactions. Insertion reactions in submicron regions likely occur at groups of many (not single) catalysts, yet not so many that their unique kinetic behavior is ensemble averaged.

Introduction

Molecular catalysts contain well-defined ligand coordination environments.[1] This leads to their widespread classical depiction (e.g., in textbooks)[2] as progressing through one uniform catalytic cycle, complete with fixed steps with fixed rates that, after catalyst initiation, are independent of time. Whether or not this time independence is an accurate depiction is largely unknown because it is obscured by ensemble averaging in typical experiments. In an elegant recent experiment employing magnetic tweezers, Escobedo, Coates, and Chen[3] showed that a single polymer growing through ring-opening metathesis polymerization (ROMP) catalyzed by the second-generation Grubbs' catalyst does not lengthen linearly, but instead exhibits wait-and-jump

steps, where the jumps are attributed to previously added monomers that coil together and then suddenly physically uncoil, effecting a sudden jump in length. Notably, the number of monomers inserted was only determinable after the physical uncoiling step; therefore the kinetics of monomer insertions were not directly detectable in real time. Thus it remains unknown whether the chemistry itself—the rate of monomer insertions and catalytic turnover—is constant at individual catalysts or also variable with respect to time. Such variability is in contrast to the simplified textbook depiction but may be possible if, for example, similar conformational changes of the growing polymer restrict access of monomer to the catalyst center.

We are interested in exploring whether the simplified textbook depiction of the chemical kinetics is accurate, or whether more details can be parsed out by performing fluorescence microscopy experiments. We herein provide the first evidence that, surprisingly, the rate of monomer insertion with respect to time at individual ruthenium catalysts is dynamic, sometimes abruptly so, and that these dynamics are correlated with the reactivity of neighboring catalysts within one polymer aggregate (or less likely dominated by a single catalyst). Although changes in the rates of insertion at single catalysts cannot be isolated from these data, the kinetic profiles nevertheless provide the first evidence that such changes occur.

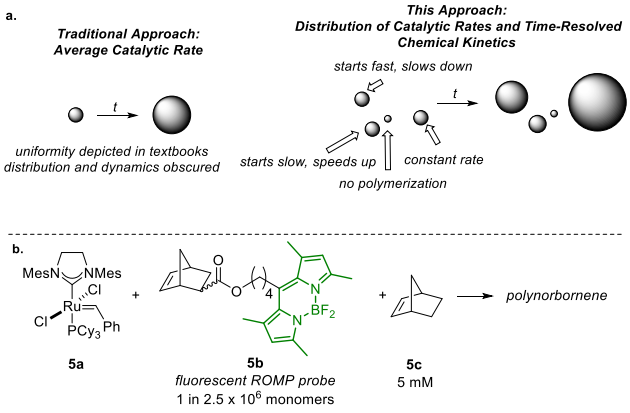

Figure 5.1. Approach to observing time-resolved chemical kinetics using fluorescence microscopy. **a.** Comparison of traditional ensemble techniques with this single-particle and single-molecule technique. **b.** Probe **5b** enables sensitive quantification of ROMP rates and rate changes in polynorbornene aggregates through fluorescence detection.

Results and Discussion

This detection was achieved with catalyst **5a**, industrially important norbornene monomer,[4] and a small amount of fluorescent probe **5b** as a dopant that enabled detection of polymerization through catalytic turnover as fluorescence intensity increases. Using fluorescence microscopy[5–16] with sensitivity sufficient for the detection of single insertion reactions[17] of **5b**, the changes in the rate of catalysis with respect to time were detected by changes in the slope of the intensity increase (Figure 5.1). The incorporation of probe **5b** into the growing polymer[18–23] was chemospecific to ring-opening metathesis as shown by a control probe containing the identical boron dipyrromethene (BODIPY) core, which lacked a functional group for olefin metathesis and was not incorporated (see Experimental for details). These experiments were performed under conditions similar to bulk polymer synthesis, in that: the catalyst and growing polymers were not tethered to glass or otherwise chemically modified;[3,7,8,11,15,21,22] the monomer was mostly untagged **5c** at high concentrations of 5 mM; the monomer was doped with low concentrations of fluorophore-tagged **5b** to avoid artifacts (2.0 nM probe, such that 1 in 2.5 x 10^6 monomers had a fluorescent tag); and the polymer chains were free to aggregate with each other.

After reaction initiation, aggregates of polynorbornene precipitated onto the microscope slide (Figure 5.2, green fluorescent particles, t = 300 s). This precipitation created a vertical jump in intensity at a given location, as seen in the corresponding intensity versus time trace at different times, followed by an intensity versus time profile unique to each examined aggregate. Aggregates that did not overlap were manually selected for further examination of their kinetic behavior (Figure 5.2, examples indicated with red boxes). The chemical kinetics of ROMP could be characterized by four features of each aggregate separately: its overall size increase, its absolute fluorescence intensity, its change in intensity with time (e.g., slope), and its variation of chemical

kinetics (i.e., if and how the slope changed with time). The latter three parameters further could be examined for subparticle regions of 0.53 x 0.53 μm^2 (0.29 μm^2) within single aggregates. Within the examined regions, a steeper slope denoted a faster rate of norbornene incorporation. Under these conditions, each aggregate likely contained multiple ruthenium catalysts,[17] but unexpectedly not so many that the kinetic behavior of the catalysts toward monomer insertion was ensemble averaged.

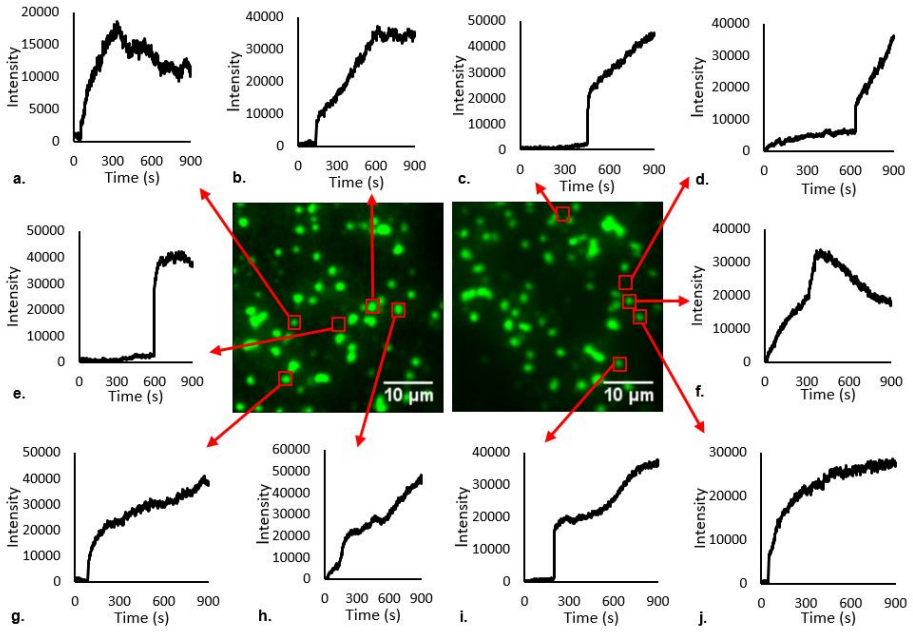

Figure 5.2. Distribution of chemical kinetics at precipitated polynorbornene particles, using probe **5b** at 2.0 nM. Intensity vs time traces for 0.29 μm^2 regions within single aggregates of polynorbornene (green particles). Red boxes denote the aggregate from which the subregion corresponding to each graph was derived; the exact coordinates for these smaller regions are available in Table 5.1. Initial vertical increases in fluorescence intensity represent polymer precipitation events. Central images from t = 300 s.

A range of time-resolved variable behavior of the subparticle chemical kinetics was observed, with some regions exhibiting time-resolved clear inflection points between states of rapid linear growth and slower linear growth (Figure 5.2b); in contrast, others displayed clear linear growth without change in the examined time window (Figure 5.2c,d,e), polymerization rates that gradually increased or decreased (Figure 5.2i,j), or polymerization rates that slowed to less

than the photobleaching rate (Figure 5.2a,f; for 2f, $t > 317$ s). Closer examination of the video shows that the reduction in rate in 2f was preceded by an increase in intensity caused by signal overlap from a growing neighboring aggregate. Adjacent aggregates showed markedly different kinetics, establishing that the time-resolved variable behavior did not arise from a global change in concentration of reagents or sample environment (compare Figure 5.2b and 5.2h; or 5.2d and 5.2f). These data suggest that: 1) the chemical kinetics in subparticle regions are variable, sometimes abruptly, and 2) the kinetics change in concert within these submicron regions of the same particle. The equally intriguing alternative, which was that these kinetics within one region were dominated by a single catalyst, was less likely given the multidirectional growth of most particles but could not be ruled out. Specifically, this multidirectional growth occurred from aggregates with multimicron diameters, too long of a distance to be attributable to growth from a single catalyst per particle (see Movies a and c in Experimental). Previous studies from our group also suggested multiple active catalysts per particle.[17]

We considered the possibility that the abrupt inflection points were not caused by a decrease in the (chemical) turnover rate of existing ruthenium catalysts but rather by a sudden (physical) decrease in the density of polymer, which would concurrently and proportionally decrease the quantity of catalyst in that region. This possibility, however, was ruled out on the basis of the intensity values at the points of inflection: if the density of the polymer suddenly decreased significantly, the absolute value of the intensity at that region should drop suddenly. In contrast to that hypothesis, no drop in intensity occurred at the inflection points (i.e., a sudden decrease in slope was not accompanied by a corresponding sudden decrease in absolute intensity; examples, Figures 5.2b and 5.2h). Thus, the density of the polymer was effectively constant on the few second timescale in which the reactivity changed between two dramatically different

kinetic states, an example of which is displayed in Figure 5.2b at $t \approx 600$ s. Therefore, the abrupt decreases in polymerization rate were assigned to changes in chemical reactivity of a fixed quantity of catalyst. The time variable data further show, then, that the degrees of chemical reactivity are not solely attributable to the quantity of ruthenium in different aggregates or in different regions of the same aggregate.

Furthermore, particles of similar shape and size display different kinetics. Representative examples shown in Figure 5.2b and 5.2h have similar shapes and sizes at $t = 300$ s but display different kinetics at that time point and over the course of the reaction. Thus, kinetics are not dominated by particle shape or size.

The changes in insertion rate with respect to time show qualitative polymerization kinetics. We next considered if quantitative kinetics of polymerization could be estimated for the linear growth regions exhibited by many particles. In order to do so, the following assumptions were applied: 1) the rate of insertion of probe **5b** was similar to that of untagged norbornene; 2) the fluorescence intensity increased linearly with respect to the number of monomers incorporated (an assumption supported by the linear regions of many graphs); and 3) the average intensity increase from chemical incorporation of a single fluorophore was ~500 intensity units. This value was obtained through detection of single-fluorophore/single-monomer incorporation and photobleaching events[24] at a lower ratio of probe to untagged monomer (0.20 pM probe **5b** and 30 mM **5c**) in which individual insertion events could be resolved in the growing polymers. This number served as a maximum for the estimate of a single monomer incorporation because of a selection bias for clearly resolved single-molecule events (two representative examples are displayed in Figure 5.3; see Experimental for details).

Estimates for the rate obtained with these assumptions provided a lower limit for the actual

rate because: 1) the larger fluorophore-tagged monomer may have diffused more slowly than untagged norbornene due to its size; 2) photobleaching reduced the signal observed (for photobleaching control, see Figure 5.11); and 3) the value of a single fluorophore was overestimated as described above. Employing this estimation with examination of 75 unique linear growth portions of 0.29 μm^2 regions, each within a distinct aggregate and from three experimental replicates, provided polymerization rates of 0.52 x 10^5–20. x 10^5 monomers s^{-1} with an average of 6.1 x 10^5 monomers s^{-1}, wherein the range reflected the distribution of kinetics in the sample (see Figure 5.8 for linear fits). The pseudo-zero order kinetics[25] implied by these linear regions indicated the possibility of a monomer-concentration independence on the observed rates. This feature may arise from diffusion-limited access of the monomer to the ruthenium[26] or from the measurement of the kinetics for short times over which the effective concentration of monomer is constant.

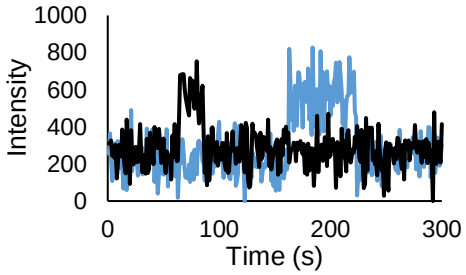

Figure 5.3. Two representative intensity vs time traces of single-monomer ROMP reactions of probe **5b** at 0.20 pM.

The time-resolved chemical kinetics within a single particle could be further interrogated within smaller regions (Figure 5.4). The data in Figure 5.4 shows that adjacent submicron regions of 267 x 267 nm^2 (0.073 μm^2) exhibit distinguishable kinetic states characterized by a rapid initial growth followed by one (Figure 5b) or two (Figure 5.4a,d) slower growth states. Graphs 5.4c, 5.4e, 5.4f, and 5.4g (yellow and blue arrows) contained rate increases at $t \approx 600$ s, attributable to the expansion of the growing polymer into those regions late in the reaction. Each of these regional

kinetic profiles was distinct from that of the particle average (Figure 5.4h, purple box).

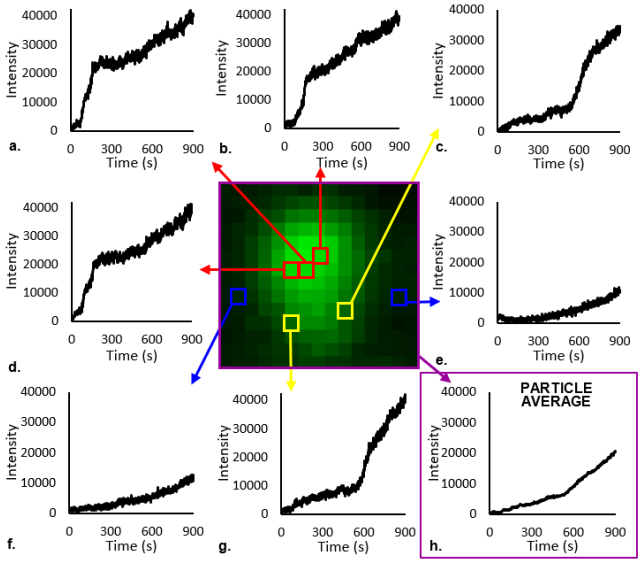

Figure 5.4. Subparticle polymerization kinetics showing different rates and variable kinetic states in different submicron regions of a single polynorbornene aggregate. Each pixel corresponds to 267 x 267 nm^2; central image from t = 650 s.

The data are consistent with changes in accessibility of the ruthenium centers towards monomer over the course of the precipitation polymerization reaction. These changes could plausibly be caused by dynamic blocking of the monomer from the ruthenium due to the growing polymer, which produces a distinct and dynamic local environment that impacts multiple neighboring ruthenium centers in concert. The conformational changes reported for single polymer strands, for example, might occur on length scales significantly longer than those previously studied.[3] Alternatively, motions caused by hydraulic pressure from the growing polymers[27] or local heating[28] might effect changes in diffusion within regions of the aggregates. The reasons for these time-dependent variations, however, are not yet fully understood.

Conclusion

In conclusion, the experiments herein provide evidence for dynamic chemical kinetics at individual molecular polymerization catalysts. Although the rates of monomer insertion at single catalysts were not measured, real-time chemical kinetics information could nevertheless be measured without the averaging that occurs in a traditional ensemble measurement (Figure 5.2). The sensitivity to detect single fluorophores from individual ROMP reactions enabled estimation of quantitative kinetics of polymerization at subparticle, submicron regions of polymer aggregates (Figure 5.3). These data unexpectedly showed that regions of polymer aggregates change catalytic chemical reactivity abruptly and that distinct kinetics dominate within a subparticle region (Figure 5.2 and 5.4). Broadly, such changing kinetic states plausibly affect the macroscopic properties of resulting polymers (for example, through regionally differing amounts of comonomer incorporation in block copolymers).[29] Key details about chemical kinetics are generally hidden by ensemble measurements, and this fluorescence microscopy approach provides a way to gain insight into the dynamic behavior of molecular catalysts and thus redefine the dogmatic view of catalytic cycles.

Experimental

I. General Information

All reagents and solvents were used as received from commercial sources unless otherwise noted. Analytical thin layer chromatography (TLC) was performed using Merck F_{250} plates and visualized under UV irradiation at 254 nm. Flash chromatography was conducted using a Teledyne Isco Combiflash® Rf 200 Automatic Flash Chromatography System, and Teledyne Isco Redisep® 35–70 μm silica gel. Spectrophotometric grade heptane (OmniSolv®) was purchased from EMD

Millipore and was used for all microscopy studies. Catalyst **1** (Grubbs Catalyst, 2nd Generation) was purchased from Sigma-Aldrich. 5-Norbornene-2-carboxylic acid (predominantly endo isomer, 97%) was purchased from Alfa Aesar. Ultra-pure water with >18 MΩ resistance and total organic content of <5 ppb was obtained from a Milli-Q Gradient A10 water purifier (Millipore, Billerica, MA) using a Q-Gard 2 purification pack and a Quantum EX Ultrapure Organex cartridge. All proton and carbon nuclear magnetic resonance (^{1}H and ^{13}C NMR) spectra were recorded on a Bruker DRX-500 spectrometer outfitted with a cryoprobe. All coupling constants were measured in Hertz (Hz). Chemical shifts were reported in ppm and referenced to residual protiated solvent peak (δ_H = 7.26 ppm for $CDCl_3$ in ^{1}H NMR spectroscopy experiments; δ_C = 77.16 ppm for $CDCl_3$ in ^{13}C NMR spectroscopy experiments. High-resolution mass spectrometry data were obtained at the University of California, Irvine.

II. Construction of Reaction Cells and Preparation of Coverslips for Microscopy

Glass coverslips (25 × 25 mm, No. 1.5, VWR Scientific) with a thickness of 0.17 mm were cleaned by sonication in 20 mL of a 0.6% solution of Hellmanex Detergent (Fisher Chemical) in MilliQ water for 60 min and then rinsed sequentially with MilliQ water and spectrophotometric grade ethanol six times. The rinsed coverslips were dried with compressed air, then placed on aluminum foil and further dried in an oven at 115 °C for 10 to 20 min. Coverslips were either stored covered in aluminum foil or used immediately after drying.

Bottomless vials were formed by cutting the ends from glass reaction vials (Short Form Style, VWR Scientific). The resulting cylinders were rinsed thoroughly with MilliQ water and spectrophotometric grade ethanol and dried in an oven at 115 °C for 20 to 30 min before use.

To assemble the reaction cells, the cleaned and dried hollow bottomless vials were attached to the cleaned coverslips by applying epoxy (Devcon) to the outside base of the tubes, then the assembled tubes were covered with aluminum foil and stored overnight or longer before use in microscopy experiments.

III. Microscopy Parameters

All microscopy imaging was performed with an inverted microscope (IX71, Olympus Corporation) and an oil-immersion, 60x objective with a 1.45 numerical aperture. Samples were imaged with a C9100-13 CCD camera (Hamamatsu Photonics). Fluorescence microscopy samples were illuminated with the 488 nm line obtained from a Ar/Kr ion laser (Coherent Inc.) set to 1.00 W. The CCD chip was a back-thinned electron multiplication type with an effective 512 × 512 array of pixels. The cell size was 16 μm, which with the 60x objective resulted in each pixel in the acquired images representing an area of approximately 270 x 270 nm. The focus was changed with a *z*-axis controller (MS-2000, Applied Scientific Instruments, Inc.). All images were acquired in total internal reflection fluorescence (TIRF).[30] The SlideBook 6.0 software (Intelligent Imaging) was set to acquire images every 1 s with 300 ms exposure to the 488 nm line per frame. Images were viewed in ImageJ (NIH, available at http://rsbweb.nih.gov/ij/).

The minimum and maximum intensity values of the videos exported from SlideBook were adjusted in ImageJ but are displayed here at constant min/max for all controls and repetitions of data at a given concentration (Section VI and Section IX). When probes **5b** and **5e** (Section IV) were added at t = 0 min at a final concentration of 2.0 nM, the display values were set to min = 6000 and max = 65535. When probe **5b** was added at t = 0 min at a final concentration of 0.20 pM, the display values were set to min = 3000 and max = 4300. No gamma correction was used.

IV. Synthetic Procedures

a. *Synthesis of fluorophore-tagged norbornene ester monomer **5b**.*

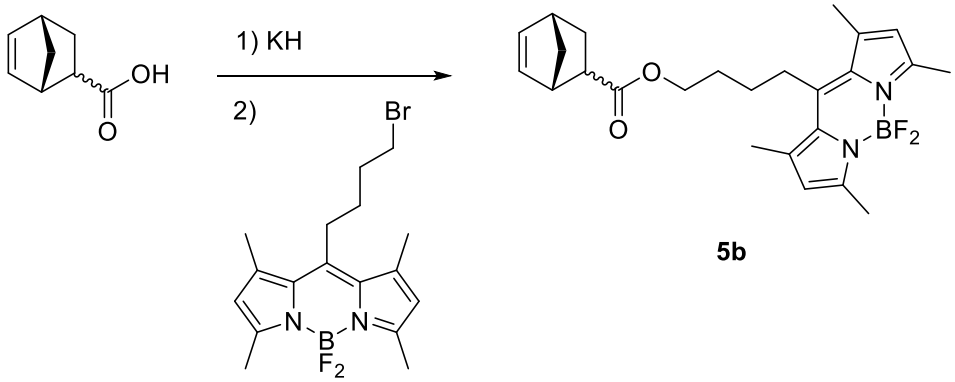

Starting material **5d** was synthesized according to an existing literature procedure.[30] In a nitrogen glove box, potassium hydride (133 mg, 3.32 mmol) and THF (20 mL) were added to a 50 mL round bottom flask. A stir bar was added, and the solution was capped with a rubber septum and removed from the glove box. Dry THF (~10 mL) was dispensed from the dry solvent system into an oven-dried 25 mL round bottom flask. This flask was removed from the system and capped with a rubber septum, briefly exposing the contents to air. From this THF was taken 5 mL via syringe and added to a separate 10 mL round bottom flask, which had previously been oven dried, capped with a septum, and flushed with nitrogen. To this 5 mL of THF was added 5-norbornene-2-carboxylic acid in an endo:exo ratio of 3:1 (392 mg, 2.84 mmol). The resulting solution was added dropwise to the separate KH/THF slurry. This solution was stirred overnight. The solution was then filtered (glass frit, medium) to yield an off-white solid. This solid was collected and without washing was immediately transferred by spatula to a second 50 mL round bottom flask with a stir bar. To the off-white solid was added **5d** (376 mg, 0.991 mmol) and DMF (25 mL). The solution was stirred for 72 h at 50 °C under dynamic nitrogen to prevent protonation of the carboxylic acid. After cooling to room temperature, the solution was diluted with ethyl acetate and washed with

water (3 × 50 mL) and brine (3 × 50 mL). The EtOAc/DMF solution was dried over magnesium sulfate, filtered, and concentrated in vacuo to give a dark red solid crude product. The resulting solid was purified by silica gel flash column chromatography using an elution of 50% CH_2Cl_2 in C_6H_{14} (R_f = 0.55), which yielded analytically pure bright red-orange solid **5b** (124 mg, 28%).

^{1}H NMR spectroscopy analysis showed a 3.0:1.0 mixture of endo:exo isomers of **5b**. ^{1}H NMR ($CDCl_3$, 500 MHz): δ 6.18 (dd, *J* = 5.5 Hz, 1H), 6.06 (s, 2H), 5.90 (dd, *J* = 5.5 Hz, 1H), 4.08 (t, *J* = 12.5 Hz, 2H), 3.17 (m, 1H), 2.98–2.95 (m, 2H), 2.94–2.89 (m, 2H), 2.52 (s, 6H), 2.42 (s, 6H), 1.90–1.87 (m, 1H), 1.82–1.79 (m, 2H), 1.75–1.72 (m, 2H), 1.44–1.37 (m, 2H), 1.28–1.25 (m, 1H). ^{13}C NMR ($CDCl_3$, 126 MHz): δ 174.8, 154.1, 145.7, 140.2, 138.0, 135.8, 131.9, 121.8, 63.5, 49.7, 45.7, 43.4, 42.6, 29.3, 28.3, 28.0, 16.4, 16.4, 14.5. HRMS (ESI+) *m/z* calcd. for $C_{25}H_{31}O_2N_2BF_2$ ($[M+Na]^+$) 463.2349, found 463.2337.

b. *Synthesis of butyl BODIPY control probe **5e**.*

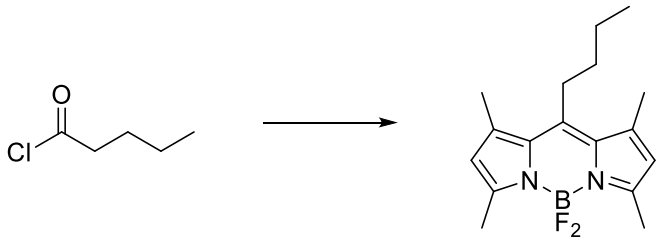

5e

Our group has previously synthesized butyl BODIPY control probe **5e**, the characterization[30] of which is reproduced here for convenience and clarity. ^{1}H NMR (500 MHz, $CDCl_3$) δ: 6.05 (s, 2H), 2.96–2.90 (m, 2H), 2.51 (s, 6H), 2.41 (s, 6H) 1.66–1.58 (m, 2H), 1.52 (sextet, *J* = 8 Hz, 2H), 0.99 (t, *J* = 8 Hz, 3H). ^{13}C NMR (126 MHz, $CDCl_3$) δ: 153.8, 146.9, 140.4,

131.6, 121.7, 33.9, 28.2, 23.6, 14.6 (t, J_{C-F} = 3 Hz), 13.9. HRMS (ESI): m/z calculated $[M+Na]^+$ 327.1823, found 327.1819.

V. Quantum Yield of Norbornene Ester Probe **5b**

Probe **5b** (1.0 mg, 2.3×10^{-3} mmol) was weighed into a 20 mL glass vial. Spectrophotometric grade heptane (2.0 mL) was added to the vial via syringe, and the solution was sonicated for 1 h to fully dissolve the compound. This afforded a solution of 1.2×10^{-3} M **2** in heptane, which was green-orange in appearance. Serial dilution using this 1.2×10^{-3} M stock solution, a 10 µL gastight syringe (Hamilton Company), and heptane allowed for the preparation of 0.50 µM **5b** in spectrophotometric heptane, which was faintly green in appearance.

To prepare **5b** for fluorescence measurements, drops of the 0.50 µM solution were added via plastic pipette to cuvettes, then filled to the indicated line with spectrophotometric grade heptane. The first cuvette contained 1 drop of the 0.50 µM solution of **5b**, the second contained 2 drops of the 0.50 µM solution, the third contained 3 drops of the 0.50 µM solution, the fourth contained 4 drops of the 0.50 µM solution, and the fifth contained 5 drops of the 0.50 µM solution. All resulting solutions were clear and colorless.

After zeroing the spectrophotometer, the absorption and excitation/emission spectra were recorded for each cuvette, with λ_{ex} = 488 nm and λ_{em} = 506 nm. A plot of the integrated emission vs. absorbance was generated, yielding a linear graph of the data (Figure 5.5). Fluorescein in 0.1 M NaOH (Φ=0.925) and Rhodamine 6G in EtOH (Φ=0.95) were used as standards.[31] The quantum yield of probe **5b** in heptane is 0.48.

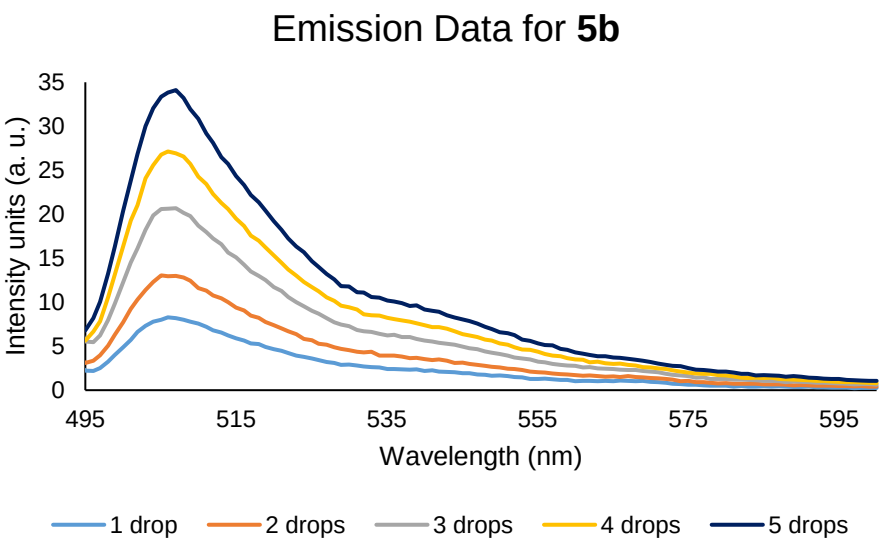

a.

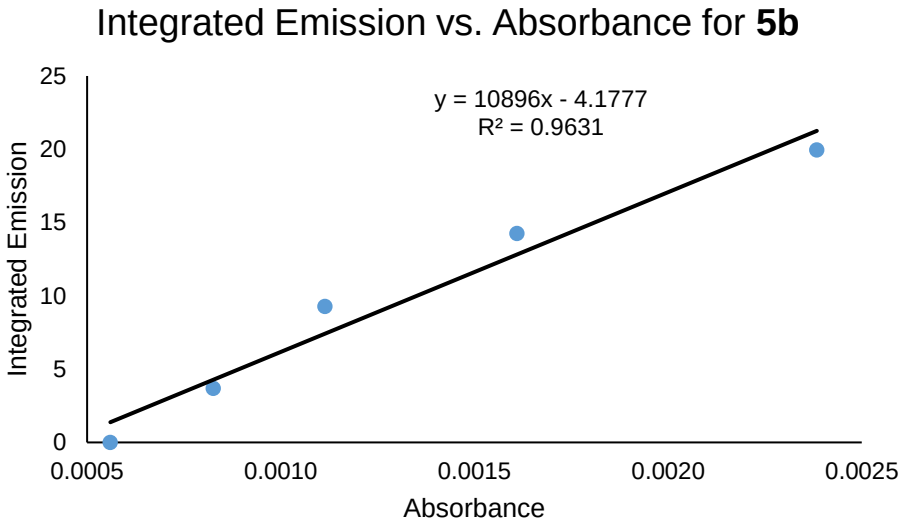

b.

Figure 5.5. **a.** Emission vs. wavelength and **b.** integrated emission vs. absorbance plots of **5b** in heptane.

VI. Sample Preparation

a. *Preparation of catalyst **5a** for fluorescence microscopy.* In a nitrogen filled glove box, catalyst **5a** (1.5 mg, 1.8×10^{-3} mmol) was weighed out into a 1 dram vial, which was then capped and brought out of the box. Spectrophotometric grade heptane (1.0 mL) was added to the vial via syringe. The resulting mixture was gently swirled, then transferred via the same syringe to

a prepared microscopy reaction vial. The solution was a light pink due to some dissolved catalyst, but much of the catalyst remained insoluble and settled on the bottom of the microscope coverslip inside the reaction vial. The microscopy vial was placed on the microscope, and the top of the coverslip was brought into focus, using room light and catalyst crystals to focus.

b. *Preparation of solutions containing monomer **5b** for microscopy.* Monomer **5b** (1.0 mg, 2.3×10^{-3} mmol) was weighed into a 20 mL glass vial. Spectrophotometric grade heptane (2.0 mL) was added to the vial via syringe, and the solution was sonicated for 1 h to fully dissolve the compound. This afforded a solution of 1.2×10^{-3} M **5b** in heptane, which was green-orange in appearance. Serial dilution using this 1.2×10^{-3} M stock solution, a 10 µL gastight syringe (Hamilton Company), and heptane allowed for the preparation of 10. nM and 1.0 pM solutions of **5b** in heptane. The solutions of **5b** prepared via serial dilution were clear and colorless in appearance.

VII. Image Acquisition of Dynamic Rate Kinetics of Polymerization of Monomer **5b** via In Operando Fluorescence Microscopy

a. *Observation of dynamic rates of polymerization of commercial norbornene and probe **5b** at 2.0 nM.* In a 1 dram vial, norbornene (0.6 mg, 6×10^{-6} mol) was weighed out and dissolved in a solution of 10. nM **5b** in heptane (0.25 mL, 2.5×10^{-12} mol), added via syringe. This solution was taken up into the same syringe, then added all at once to the mixture of catalyst **5a** in heptane prepared according to the process described in Section VI, yielding a final solution volume of 1.25 mL. The resultant concentration of norbornene was 0.005 M, and the resultant concentration of probe **5b** was 2.0 nM. Immediately after the solution was added, the sample was

focused in TIRF, and video acquisition of the sample began (Section III). The stage was not moved after the sample was focused on the coverslip.

Upon initiating video acquisition of the sample and focusing into TIRF, bright green round polymer spheres were immediately visible on the glass coverslip surface. As time progressed, more bright green polymer spheres precipitated out of solution. Polymer sphere size varied at initial precipitation, but polymers that precipitated at later time points were somewhat larger than polymers that precipitated at earlier time points.

Final video acquisition of the sample began at t = 1 min and lasted until t = 16 min after addition of the monomer solution to catalyst **5a**. During the acquisition, some polymers that had previously precipitated out of solution onto the surface of the coverslip showed an increase in brightness and diameter with the progression of time. Further, these polymers also became brighter with their concurrent diameter increase (Figure 5.6). These observations are consistent[17] with the insertion of **5b** into the growing polymer chain.

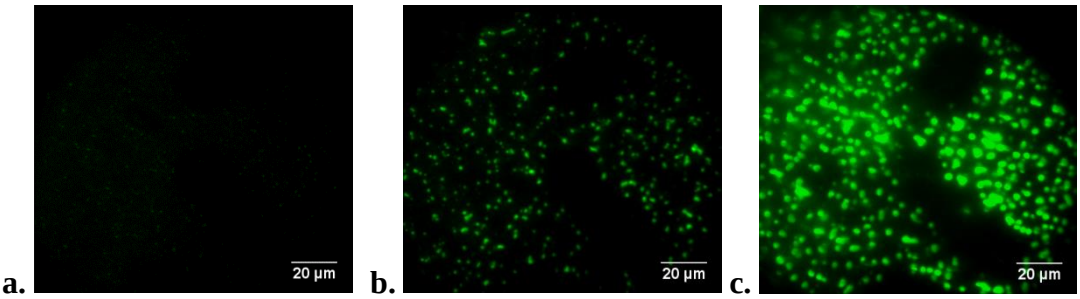

Figure 5.6. Polymerization of **5b** at 2.0 nM. Images taken at t = **a.** 1 min, **b.** 6 min, and **c.** 16 min.

Time trace data graphs were compiled by first selecting a 2 × 2 pixel region of the polymer (Table 5.1, coordinates of polymers), corresponding to 534 × 534 nm^2. ImageJ gave an output of intensity values at specific times, which were plotted using Excel. To facilitate comparison of kinetics, the lowest intensity value from all points collected was then subtracted, giving the total overall intensity change at individual polymers. Examination of the time trace data acquired from

specific locations of polymer growth (Figure 5.2) showed that the time traces were distinct from each other. The differences in time trace shape and final intensity were also observed for adjacent precipitated polymers, showing that the differences did not arise from a global change in conditions. Since the increase in fluorescence intensity is attributable to insertion of **5b** into the polymer, the varying shapes of the time traces illustrate a difference in dynamic rates of insertion of **5b**.

Table 5.1. Coordinates of polymers used for analysis of rate dynamics in Figure 5.2.

Polymer	**X-coordinates**	**Y-coordinates**
1	381, 382	194, 195
2	381, 382	218, 219
3	349, 350	164, 165
4	390, 391	167, 168
5	391, 392	131, 132
6	333, 334	476, 477
7	379, 380	449, 450
8	353, 354	491, 492
9	340, 341	483, 484
10	320, 321	408, 409

b. *Quantification of rate kinetics of polymerization of commercial norbornene and **5b** at 2.0 nM and replicate data.* A second and third run were performed identical to that described in Section VIIa. Figure 5.7 shows data from replicate 2. All three of the triplicate runs were used for kinetic analysis. For clarity, example fitting from run number 2 is shown here. The other runs were fit using an identical process.

Time trace data graphs were compiled by first selecting a 2 × 2 pixel region of the polymer that was within the red box shown in Figure 5.2 (red boxes denote the particle from which the kinetics of the smaller area were taken, corresponding to 534 × 534 nm^2). The regions are so small that use of smaller boxes overlaid on top of the images would obscure the selected regions. Exact coordinates for these smaller 2 × 2 pixel regions are given in Table 5.1. The value $t = 0$ refers to the starting time of the video, approximately 1 minute after the reagents were mixed. ImageJ gave an output of intensity values at specific times, which were plotted using Excel. The lowest intensity value from all points collected was then subtracted, giving the total overall intensity change at individual polymers. For direct comparison of the time trace data, multiple graphs were overlaid into one final graph, with different colors highlighting the shape of each curve (Figure 5.8a). Different shapes were observed, along with varying polymer precipitation times. This distribution of curve shapes and precipitation times provided further evidence for dynamic rates of insertion of **5b** into the growing polymer.

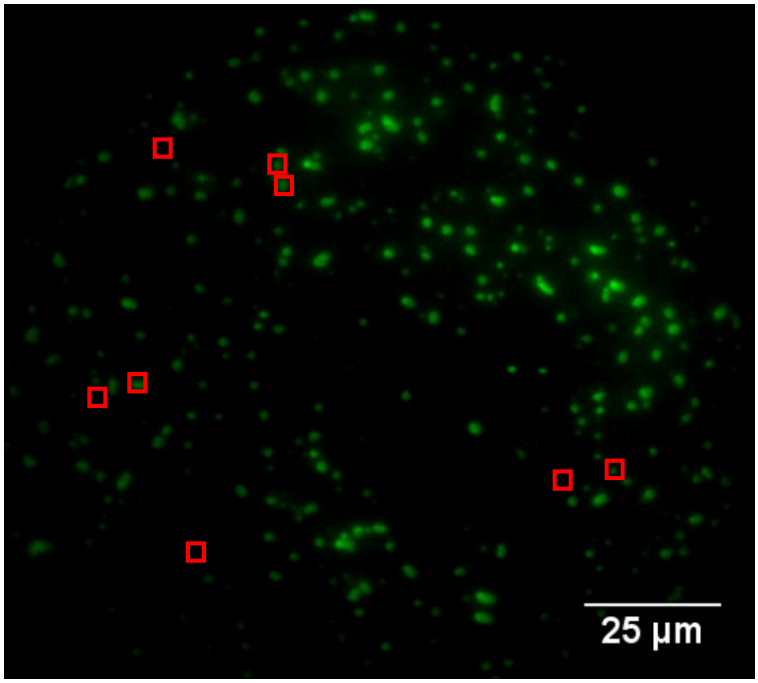

Figure 5.7. Polymer growth at *t* = 300 s. Red boxes denote particles from which smaller regions were selected; exact coordinates for these smaller regions are given in Table 5.1.

Some curves contained linear regions of increasing intensity corresponding to pseudo zero order kinetics[25]. If a region contained more than one linear portion, the one with the steepest slope was evaluated. These regions were plotted in Figure 5.8b with $R^2 > 0.90$. The slopes of the lines obtained represented an increase in fluorescence intensity given as intensity units per second. Multiplying these slope by 60, then dividing by the average intensity unit value per fluorophore, ~500 intensity units (see Section VIId for details), allowed for the conversion of the slope into monomers per minute (Table 5.2), which represented an estimate of the rate of catalytic activity at the precipitated polymers. This time unit of monomers per minute was chosen as a logical descriptor instead of monomers per second because using the unit per second implied that fractional values of fluorophore-tagged monomers were inserted per second.

To evaluate the total monomer consumption at these polymers, including untagged monomer, the monomers per minute slopes were multiplied by the ratio of tagged to untagged

monomer (2.6×10^6:1 untagged:tagged), then divided by 60, giving total monomers per second (Table 5.2). In this case, monomers per second was a logical unit. These slopes thus provide information on chemical kinetics and corresponding dynamics at individual regions of polymer.

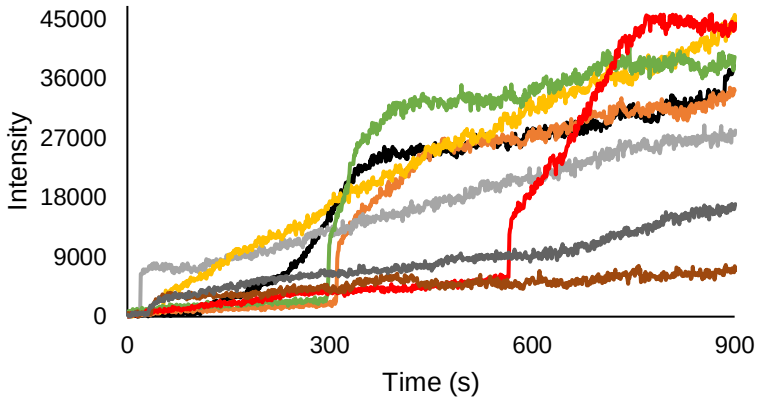

a.

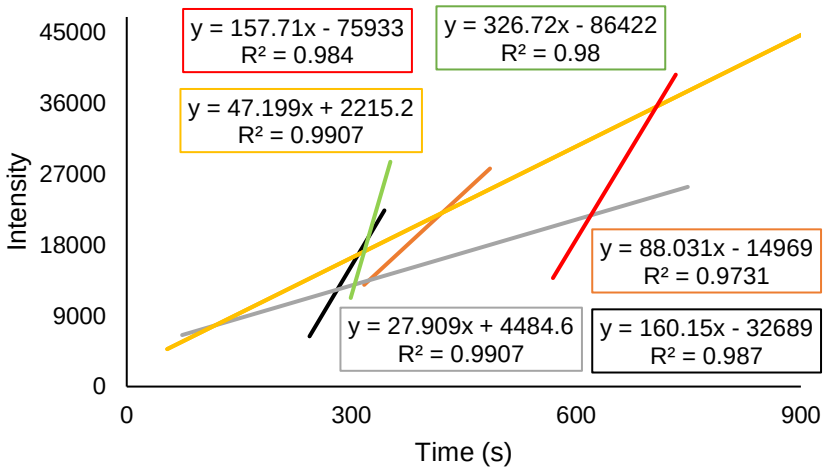

b.

Figure 5.8. Time-resolved nonuniform chemical kinetics. **a.** Overlay of multiple graphs of dynamic rates of insertion of **5b** into growing polymers. **b.** Example plots of some of the linear regions of rates of insertion of **5b** in intensity units/s, corresponding to data in part **a**.

Table 5.2. Converted rates of insertion of **5b** into growing polymers in monomers/min and total monomers/s for the examples in Figure 5.8.

Line color	**Tagged monomers/min**	**Total monomers/s**
yellow	5.7	2.5×10^5
red	18.9	8.3×10^5
orange	10.6	4.7×10^5
black	19.2	8.3×10^5
green	39.2	1.7×10^6
grey	3.5	1.5×10^5

c. *Single-particle rate kinetics of polymerization of commercial norbornene and **5b** at 2.0 nM.* For analysis, time trace data graphs were compiled by selecting 1 × 1 pixel regions in and around the polymer, corresponding to 267 × 267 nm^2 selection areas. ImageJ gave an output of intensity values at specific times, which were plotted using Excel. The lowest intensity value from all points collected was then subtracted, giving the total overall intensity change at individual locations in and around the polymer. Figure 5.4 shows a selected particle with highlighted boxes, accompanied by the time traces according to each box, which include control areas outside the area of polymer growth. Further, the entire observation area was also averaged. The data show that single particles can exhibit nonuniform rate kinetics during polymerization. Polymer growth at two different areas within the same particle occurs with distinguishable kinetics.

d. *Single molecule insertions of **5b** at 0.20 pM into growing polynorbornene*. In a 1 dram vial, norbornene (3.0 mg, 3.2×10^{-5} mol) was weighed out and dissolved in a solution of 1.0 pM **5b** in heptane (0.25 mL, 2.5×10^{-16} mol), added via syringe. This solution was taken up into the same syringe, then added all at once to the mixture of catalyst **5a** in heptane prepared according to the process described in Section VI, yielding a final solution volume of 1.25 mL. The resultant concentration of norbornene was 0.026 M, and the resultant concentration of probe **5b**

was 0.20 pM. Immediately after the solution was added, the sample was focused in TIRF, and video acquisition of the sample began. The stage was not moved once the sample was focused on the coverslip.

As soon as video acquisition of the sample began, including focusing the sample into TIRF, the sample was illuminated clearly by the laser but did not have any discernible features, unlike when a higher probe concentration was used. However, at t = 7 min, dynamic flickers could be seen at the surface of the coverslip. These flickers became more clearly resolved at t = 18 min. Time trace data of 2 × 2 pixel regions, corresponding to 534 × 534 nm^2, of these flickering regions showed quantized fluorescence intensity increases, lasting for multiple frames, before the corresponding quantized fluorescence intensity decreases (three examples from different polymers, Figure 5.9). These quantized events are consistent with the detection of single fluorophore molecules.[24] Probe **5b** contains only a norbornene unit capable of chemical reaction with catalyst **5a**. Thus, individual ring-opening events of **5b** into the growing polymer were observed. The average intensity value from these insertions was estimated as 500 intensity units.

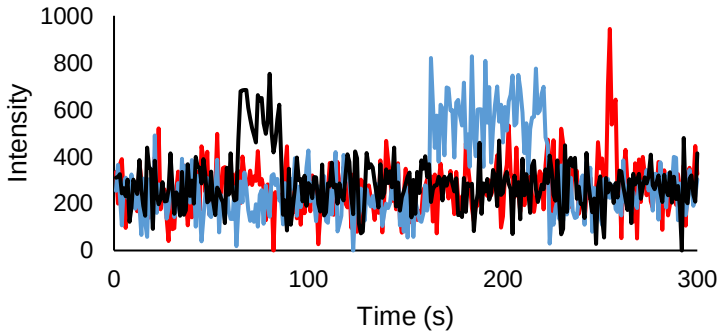

Figure 5.9. Single ring-opening events of **5b** at 0.20 pM. Events were resolved at different polymers.

VIII. Control Experiments for Assignment of Fluorescent Regions as Products of Ring-Opening Metathesis Polymerization

a. *Use of probe **5e** in place of **5b** at 2.0 nM.* Probe **5e** had no norbornene unit and therefore could not participate in ROMP reactions with catalyst **5a** to give rise to rates (Section VII). Butyl BODIPY control probe **5e** (1.0 mg, 3.3×10^{-3} mmol) was weighed out into a 20 mL glass vial. Spectrophotometric grade heptane (2.0 mL) was added to the vial via syringe, and the solution was sonicated for 1 h to fully dissolve the compound. This afforded a solution of 1.7×10^{-3} M **5e** in heptane, which was green-orange in appearance. Serial dilution using this 1.7×10^{-3} M stock solution, a 10 µL gastight syringe (Hamilton Company), and heptane allowed for the preparation of 10. nM **5e** in heptane, which was a clear colorless solution.

In a 1 dram vial, norbornene (0.6 mg, 6×10^{-6} mol) was weighed out and dissolved in a solution of 10. nM **5e** in heptane (0.25 mL, 2.5×10^{-12} mol), added via syringe. This solution was taken up into the same syringe, then added all at once to the mixture of catalyst **5a** in heptane prepared according to the process described in Section V, yielding a final solution volume of 1.25 mL. The resultant concentration of norbornene was 0.005 M, and the resultant concentration of probe **5e** was 2.0 nM. Immediately after the solution was added, the sample was focused in TIRF, and video acquisition of the sample began (Section III). The stage was not moved after the sample was focused on the coverslip.

On the surface of the coverslip, no fluorescent green regions were observed (Figure 5.10), in contrast to Figure 5.2. Therefore, the growth of the fluorescent green polymer is due to chemical incorporation of **5e** into the polymer, and is not due to physical uptake of probe into the polymer.

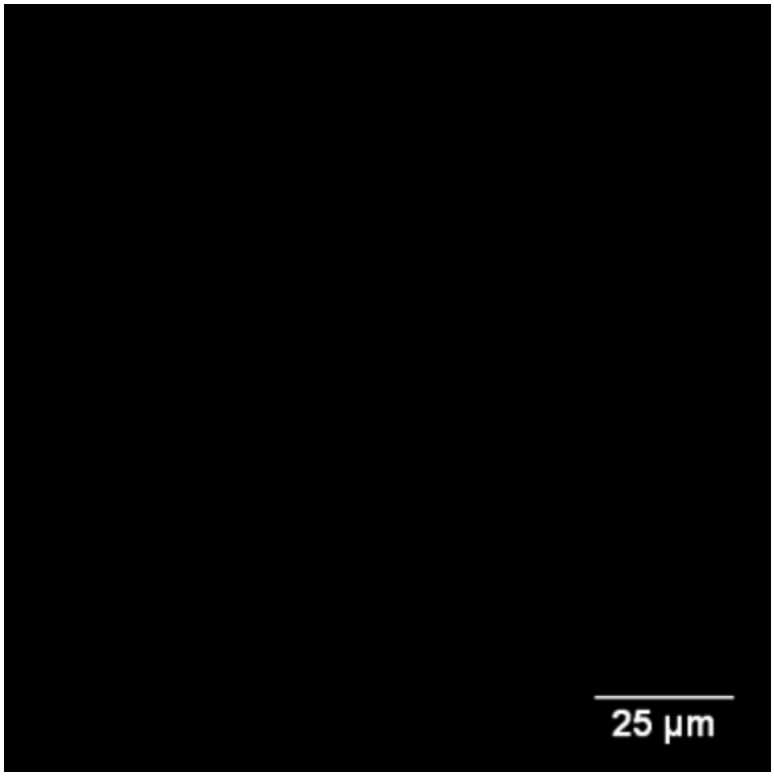

Figure 5.10. Image of polymerization of norbornene with control probe **5e** at t = 900 s. Control experiment image displayed at identical min/max settings as Figure 5.2.

b. *Photobleaching control: Removal of mother liquor containing 2.0 nM **5b** at t = 450 s.* In a 1 dram vial, norbornene (0.6 mg, 6×10^{-6} mol) was weighed out and dissolved in a solution of 10. nM **5b** in heptane (0.25 mL, 2.5×10^{-12} mol), added via syringe. This solution was taken up into the same syringe, then added all at once to the mixture of catalyst **5a** in heptane prepared according to the process described in Section VI, yielding a final solution volume of 1.25 mL. The resultant concentration of norbornene was 0.005 M, and the resultant concentration of probe **5b** was 2.0 nM. Immediately after the solution was added, the sample was focused in TIRF, and video acquisition of the sample began (Section III). The stage was not moved after the sample was focused on the coverslip.

Upon initiating video acquisition of the sample and focusing into TIRF, bright green round polymer spheres were immediately visible on the glass coverslip surface. As time progressed,

bright green polymer spheres continued to precipitate out of solution. Polymer sphere size varied at initial precipitation, but polymers that precipitated at later times were somewhat larger than polymers that precipitated at earlier times.

Video acquisition of the sample under standard conditions began at t = 1 min and lasted until t = 8 min 30 s after addition of the monomer solution to catalyst **5a**. During the acquisition, some polymers, which had previously precipitated out of solution onto the surface of the coverslip, showed an increase in brightness and diameter with the progression of time. Further, these polymers also became brighter with their concurrent diameter increase. These observations are consistent[17] with the insertion of **5b** into the growing polymer chain.

At t = 8 min 30 s, the mother liquor was removed via syringe, and blank spectrophotometric grade heptane (0.25 mL) was added to the sample via a separate syringe. Video acquisition of this sample began at t = 9 min (Figure 5.11, image at t = 0 of acquisition) and lasted for another 5 min with the same SlideBook parameters that were originally used. During the observation period, the bright green polymers exhibited a gradual decrease in fluorescence intensity due to photobleaching (Figure 5.11). Since all tagged monomer had been removed from solution, the decrease in fluorescence intensity was due to the photobleaching of previously incorporated probe. The graphs are plotted with intensity as the y-axis, and the minimum value was set to zero for ease of comparison between graphs.

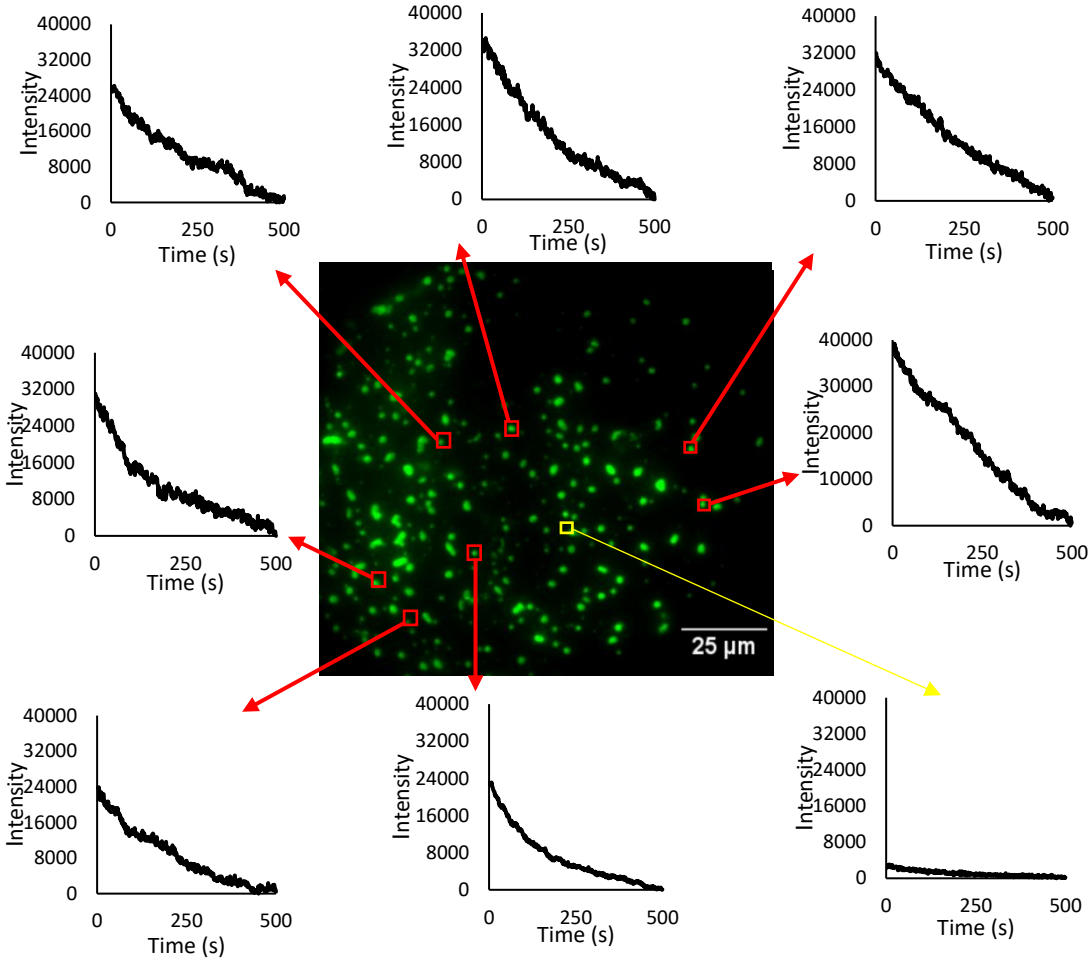

Figure 5.11. Polymers prior to photobleaching at t = 9 min. Accompanying graphs show photobleaching over 8 min (500 s) of exposure to the laser. Background decrease (yellow) in lower right graph.

References

(1) Buchmeiser, M. R. *Chem. Rev.* **2000**, *100*, 1565–1604.
(2) Crabtree, R. H. *The Organometallic Chemistry of the Transition Metals*, 5th ed.; John Wiley & Sons, Inc.: Hoboken, **2009**, p. 380.
(3) Liu, C.; Kubo, K.; Wang, E.; Han, K.-S.; Yang, F.; Chen, G.; Escobedo, F. A.; Coates, G. W.; Chen, P. *Science* **2017**, *358*, 352–355.
(4) Mol, J. C. *J. Mol. Catal. A: Chem.* **2004**, *213*, 39–45.
(5) Weckhuysen, B. M. *Angew. Chem. Int. Ed.* **2009**, *48*, 4910–4943.
(6) Buurmans, I. L. C.; Weckhuysen, B. M. *Nat. Chem.* **2012**, *4*, 873–886.
(7) Cordes, T.; Blum, S. A. *Nat. Chem.* **2013**, *5*, 993–999.
(8) Blum, S. A. *Phys. Chem. Chem. Phys.* **2014**, *16*, 16333–16339.
(9) Chen, P.; Zhou, X.; Andoy, N. M.; Han, K.-S.; Choudhary, E.; Zou, N.; Chen, G.; Shen, H. *Chem. Soc. Rev.* **2014**, *43*, 1107–1117.
(10) Tachikawa, T.; Majima, T. *Langmuir* **2012**, *28*, 8933–8943.

(11) Rybina, A.; Lang, C.; Wirtz, M.; Gruβmayer, K.; Kurz, A.; Maier, F.; Schmitt, A.; Trapp, O.; Jung, G.; Herten, D.-P. *Angew. Chem. Int. Ed.* **2013**, *52*, 6322–6325.
(12) Kubarev, A. V.; Janssen, K. P. F.; Roeffaers, M. B. J. *ChemCatChem* **2015**, *7*, 3646–3650.
(13) Ristanović, Z.; Kerssens, M. M.; Kubarev, A. V.; Hendriks, F. C.; Dedecker, P.; Hofkens, J.; Roeffaers, M. B. J.; Weckhuysen, B. M. *Angew. Chem. Int. Ed.* **2015**, *54*, 1836–1840.
(14) Hodgson, G. K.; Impellizzeri, S.; Scaiano, J. C. *Chem. Sci.* **2016**, *7*, 1314–1321.
(15) Ng, J. D.; Upadhyay, S. P.; Marquard, A. N.; Lupo, K. M.; Hinton, D. A.; Padilla, N. A.; Bates, D. M.; Goldsmith, R. H. *J. Am. Chem. Soc.* **2016**, *138*, 3876–3883.
(16) Kitagawa, K.; Blum, S. A. *ACS Catal.* **2017**, *7*, 3786–3791.
(17) Easter, Q. T.; Blum, S. A. *Angew. Chem. Int. Ed.* **2017**, *56*, 13772–13775.
(18) Wöll, D.; Braeken, E.; Deres, A.; De Schryver, F. C.; Uji-i, H.; Hofkens, J. *Chem. Soc. Rev.* **2009**, *38*, 313–328.
(19) Esfandiari, N. M.; Blum, S. A. *J. Am. Chem. Soc.* **2011**, *133*, 18145–18147.
(20) Hensle, E. M.; Blum, S. A. *J. Am. Chem. Soc.* **2013**, *135*, 12324–12328.
(21) Wirtz, M.; Grüter, A.; Heib, F.; Huch, Y.; Zapp, J.; Herten, D.-P.; Schmitt, M.; Jung, G. *Methods Appl. Fluoresc.* **2015**, *3*, 044001.
(22) Easter, Q. T.; Trauschke, V.; Blum, S. A. *ACS Catal.* **2015**, *5*, 2290–2295.
(23) Keshavarz, M.; Engelkamp, H.; Xu, J.; Braeken, E.; Otten, M. B. J.; Uji-i, H.; Schwartz, E.; Koepf, M.; Vananroye, A.; Vermant, J.; Nolte, R. J. M.; De Schryver, F.; Maan, J. C.; Hofkens, J.; Christianen, P. C. M.; Rowan, A. E. *ACS Nano* **2016**, *10*, 1434–1441.
(24) Lakowicz, J. R. *Principles of Fluorescence Spectroscopy*, 3rd ed.; Springer: New York, **2006**.
(25) Elling, B. R.; Xia, Y. *J. Am. Chem. Soc.* **2015**, *137*, 9922–9926.
(26) Gallardo, A.; Rodríguez, G.; Aguilar, M. R.; Fernández, M.; San Román, J. *Macromolecules* **2003**, *36*, 8876–8880.
(27) Fink, G.; Steinmetz, B.; Zechlin, J.; Przybyla, C.; Tesche, B. *Chem. Rev.* **2000**, *100*, 1377–1390.
(28) Duda, J. L. *Pure & Appl. Chem.* **1985**, *57*, 1681–1690.
(29) Schacher, F. H.; Rupar, P. A.; Manners, I. *Angew. Chem. Int. Ed.* **2012**, *51*, 7898–7921.
(30) Esfandiari, N. M.; Wang, Y.; Bass, J. Y.; Cornell, T. P.; Otte, D. A. L.; Cheng, M. H.; Hemminger, J. C.; Mcintire, T. M.; Mandelshtam, V. A.; Blum, S. A. *J. Am. Chem. Soc.* **2010**, *132*, 15167–15169.
(31) Williams, A. T. R.; Winfield, S. A.; Miller, J. N. *Analyst* **1983**, *108*, 1067–1071.

Chapter 6

Kinetics of the Same Reaction over Nine Orders of Magnitude of Concentration: When Are Unique Subensemble and Single-Turnover Information Displayed?

Abstract: Essentially no information is known about the behavior of individual molecular catalysts under reaction conditions, due to the averaging inherent to traditional analytical techniques. Herein, a combined fluorescence microscopy and ^{1}H NMR spectroscopy study reveals that unique (that is, non-ensemble averaged) time-variable kinetics from molecular ruthenium catalysts within growing polynorbornene occur and are detectable between 10^{-9} M and, surprisingly, 10^{-6} M of substrate, just 1000-fold less concentrated than a typical laboratory bench-scale reaction. The kinetic states governing single-turnover events are determinable by overlay of the signal arising from individual monomer insertion reactions with that from polymer growth from neighboring catalysts.

Introduction

The behavior of individual molecular catalysts underpins all reactivity observed at the bulk scale, yet there is essentially no information about the behavior of individual molecular catalysts.[1–3] The main challenge with identifying the behavior of individual molecular catalysts is the ensemble averaging inherent to traditional analytical techniques. Molecular catalysts are typically depicted as proceeding through uniform catalytic cycles because of their well-defined ligand coordination sphere; however, it is poorly understood if they display reactivity that deviates from

uniformity, what reaction conditions cause these deviations, and when and how these deviations could be observed. Employing fluorescence microscopy[4,5,14,6–13] with sensitivity sufficient for the detection of single insertion reactions, we recently reported the first imaging of single turnover at individual molecular catalysts.[1,2] These experiments begin to realize the potential of single-molecule techniques to reveal the otherwise obscured nonuniform behavior of molecular catalysts; specifically, it was discovered that individual molecular ruthenium polymerization catalysts proceed through distinct, abruptly changing kinetic states, plausibly dictated by changing local environments within growing polymer aggregates.[2] We are now interested in determining boundary conditions in which molecular catalysts display unique and detectible non-ensemble-averaged reactivity, including conditions amenable to single-turnover detection at molecular catalysts. Herein, we examine a norbornene polymerization reaction over nine orders of magnitude in substrate concentration—all the way from single-turnover detection at 10^{-12} M (by fluorescence microscopy)[1] to fully ensemble-averaged kinetics at 10^{-3} M (by ^{1}H NMR spectroscopy), and including three concentrations in between[15] (Experimental Schematic, Figure 6.1a). These results provide early conceptual guidance for designing experiments that revise our understanding of the behavior of molecular catalysts through characterization of their non-averaged, divergent behavior.

These fluorescence microscopy experiments, capable of detecting single monomer insertion reactions, raise questions about how to determine the kinetic criteria that govern individual molecular catalysts in soft materials. Studies of inorganic zeolite catalysts, in contrast, have been well-studied and display largely time invariant kinetics;[16–19] gold nanoparticles display activity fluctuations attributed to dynamic surface restructuring.[13] Polymers have been previously studied by fluorescence microscopy[20–22] but not during growth with molecular catalysts. Our recent

studies showed that in catalytic polymerization, the kinetics at a single region may change abruptly.[2] Further, such states appear to follow both pseudo zero-order and higher-order kinetics during the same reaction.[2] Thus, the rate law dictating the reactivity of one chemical reaction is not appropriately modeled by summing events and averaging over the duration of the observation time, during which the material might have cycled through many distinct catalytic states, possibly unobserved.[13]

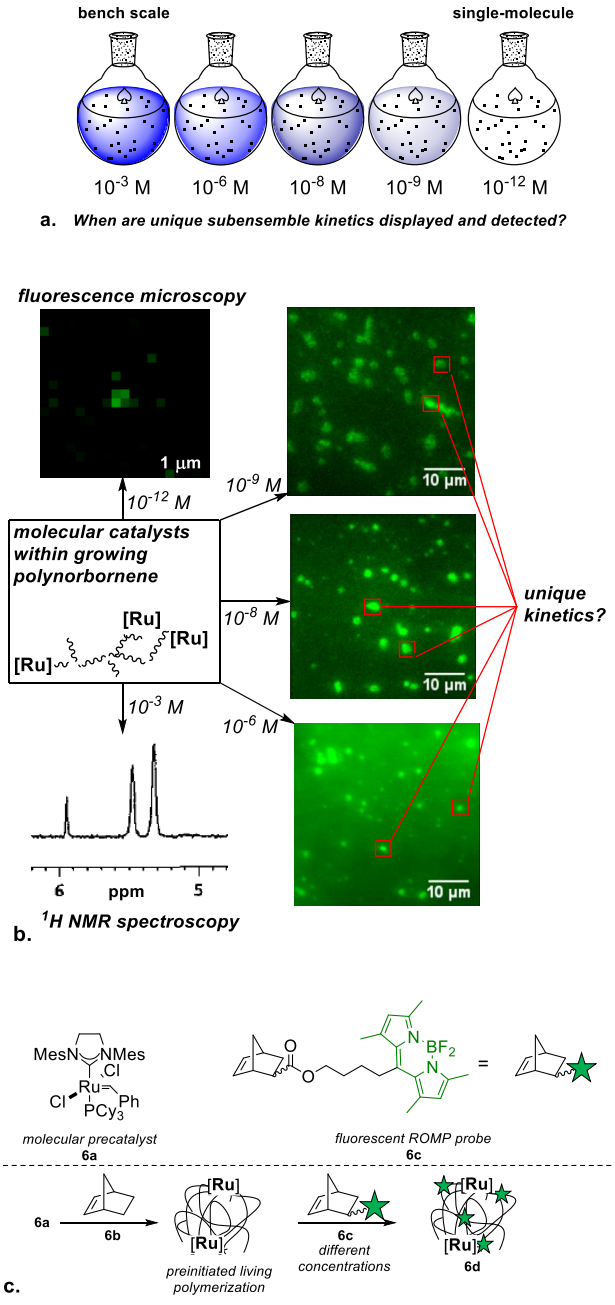

Figure 6.1. a. Schematic showing experimental question. **b.** Representative fluorescence microscopy images and ^{1}H NMR spectrum of the polymerization of norbornene by molecular ruthenium catalysts. Growing polymer aggregates are bright green shapes at 10^{-9}, 10^{-8}, and 10^{-6} M of monomer **6c**. Image at 10^{-12} M shows a single insertion reaction at t = 189 s after reaction initiation. **c**. Schematic showing catalyst, probe molecules, and generation of preinitiated polymers.

Results and Discussion

Here, we demonstrate a strategy wherein single chemical insertion events are constituents of overall signal increases indicative of the time-variable kinetic state of that region at that time, thereby allowing qualitative determination of the kinetic criteria that underpin a single chemical reaction. Specifically, while each individual turnover or monomer insertion event occurs at an individual molecular catalyst, multiple detected insertion events likely occur at different neighboring catalysts.[1,2] Key to this approach is the prior knowledge that the time-variable kinetics in this system are regionally synchronized (i.e., that groups of molecular catalysts in local regions are changing kinetics in concert);[2] thus, the measurement of the time-variable kinetics governing a region is a reasonable indicator of those that govern a single turnover reaction within that region.

The experimental design (eq 1) employed a precipitation polymerization reaction of commercially available second-generation Grubbs' catalyst **6a** and industrially important[23] norbornene monomer **6b** in order to create pre-initiated growing particles of polynorbornene with active ruthenium catalysts contained within, as a stage of a living polymerization reaction.[24] The mother liquor was then removed, leaving behind polymer particles containing multiple active ruthenium catalysts.[1,2] In-house synthesized imaging agent **6c** consisted of a reactive norbornene monomer tagged to a spectator boron dipyrromethene (BODIPY) fluorophore. Incorporation of this monomer into a pre-initiated growing particle of fluorophore-free polynorbornene enabled its detection through fluorescence microscopy. This experimental protocol was selected so that the dark background[25] of untagged polynorbornene would not produce a fluorescence signal, providing conditions most amenable to detection of single insertion events against a dark background after addition of imaging agent **6c** at t = 6 min to the pre-initiated polymers.

At concentrations of 10^{-8} and 10^{-9} M **6c**, chemical incorporation of imaging agent **6c** into the growing polymers was sufficiently fast that growing green aggregates of polynorbornene **6d** were clearly visible in fluorescence images against a dark background of the solution (Figure 6.2b). At the higher concentration of 10^{-6} M **6c**, individual particles of **6d** could still be resolved, but the background fluorescence from monomer **6c** diffusing in solution became sufficiently high so as to create a notable haze in the images. At concentrations higher than 10^{-6} M, the background became too bright for monitoring the kinetic behavior of individual particles of **6d**, providing an upper bound to this technique. At the other concentration extreme, 10^{-12} M **6c**, flashes corresponding to single insertion events could be seen. (Figure 6.2b shows a fluorescence image corresponding to a single chemical insertion event.) Use of a control probe that contained the identical BODIPY unit but no olefin-metathesis-reactive functional group did not show this incorporation under otherwise identical conditions (see Experimental for details). Thus, the increase in fluorescence signal was attributed to chemical incorporation of tagged monomer **6c** into the growing polymers by molecular ruthenium catalysts contained within the precipitated polymer aggregates (**6d**).

Next, 512 x 512 nm^2 regions within individual aggregates of **6d** were examined for the kinetics of catalytic polymerization under each of the concentrations examined by fluorescence microscopy. Intensity vs. time graphs provided both quantitative and qualitative kinetic information. Figure 6.2 shows representative rate data obtained from each of these concentrations for comparison.

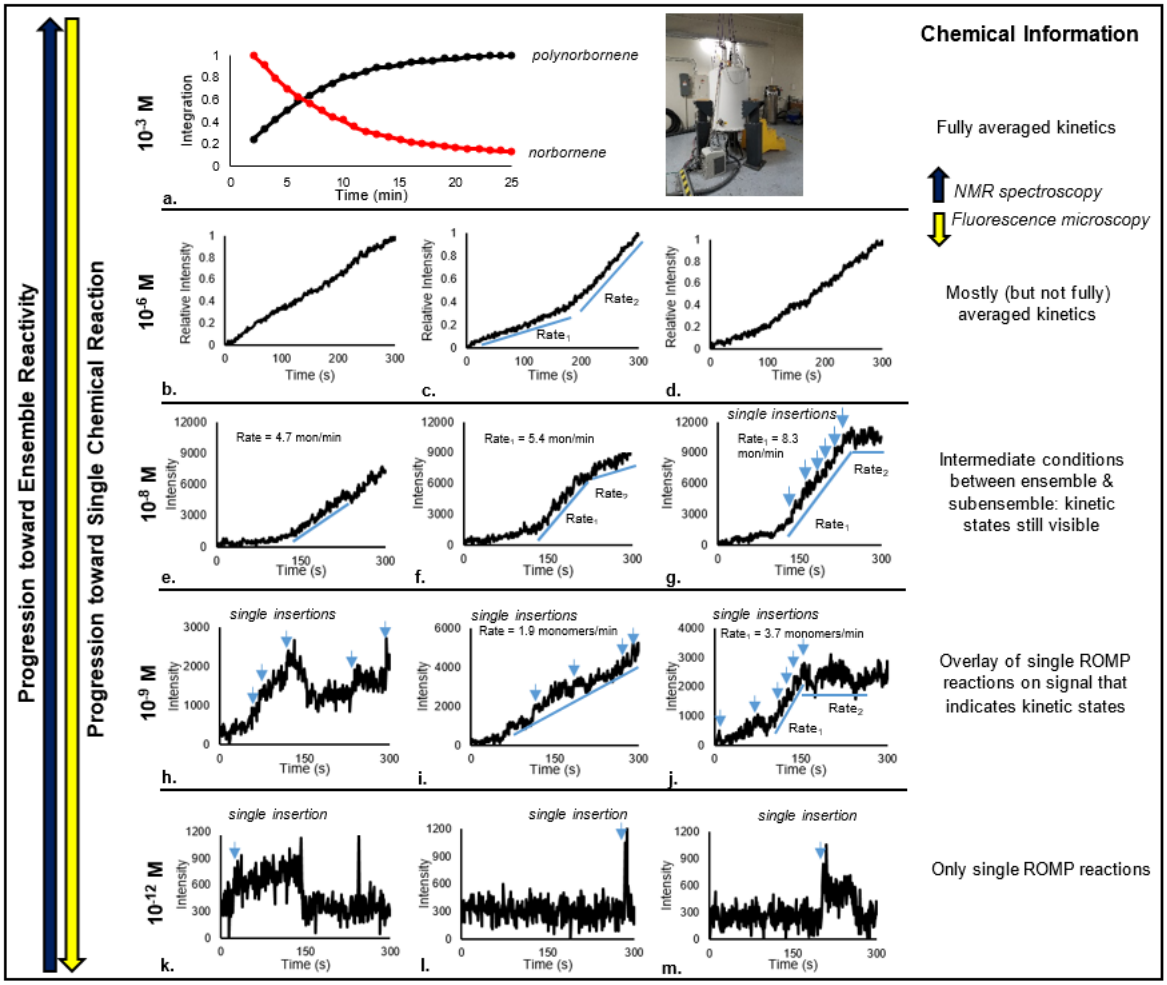

Figure 6.2. Comparison of reaction progress data from 10^{-12} M to 10^{-3} M via a combined fluorescence microscopy and ^{1}H NMR spectroscopy approach. Lower concentrations of monomer **6c** reveal not only single chemical reactions (10^{-12} M) but also resolvable time-variable kinetic states (10^{-9} M and 10^{-8} M). Higher concentrations of monomer reveal progressively averaged polymerization kinetics (10^{-6} M **6c** and 10^{-3} M **6b**), yet the time variable kinetic state switching can still be resolved in a subset of particles at 10^{-6} M.

At the lowest examined concentration of substrate, 10^{-12} M **6c**, single insertion reactions at individual molecular catalysts within precipitated polynorbornene aggregates were visible, as characterized by their well-established quantized "step up" behavior in the intensity vs. time profiles followed by quantized photobleaching "step down" events[26] (Figure 6.2k–m). This data provided limited information on the chemical reaction kinetics that were governing the region of

6d at the moment in time during which an individual reaction occurred, however, given the rare nature of the chemical insertion events at this concentration.

We hypothesized that a higher concentration of **6c**, 10^{-9} M, would provide an overlay of single-molecule detection and polymer growth kinetics. Indeed, precipitated polymers that were initially not visible due to lack of fluorophore incorporation became bright green when tagged monomer **6c** was added to the solution (Figure 6.2h–j). Within the time traces from these polymers, there were multiple quantized steps up within the fluorescence signal traces within individual particles of **6d**, corresponding to insertion events of individual monomers of **6c**. The magnitude of the quantized steps are each also consistent with insertion of single molecules of **6c**.[1,2] In addition, some quantized decreases corresponding to individual photobleaching events are visible. Yet at this concentration, the number of chemical insertion events of **6c** at the example regions was sufficiently faster than photobleaching so as to provide information regarding the kinetic states of catalysis at the moment of many of the single incorporation events.

For example, the polymerization kinetics in Figure 6.2i fit a single, pseudo zero-order kinetic state for the duration of the imaging. The rate of insertion of monomer **6c** can be estimated with a linear fit of the increase in intensity with time. Assuming that each monomer insertion results in an increase of ~500 intensity counts[2] yields an estimated rate of 1.9 monomers/min in Figure 6.2i. Figures 6.2h and 6.2j, in contrast, show the abrupt, time-variable kinetic state changes previously observed.[2] Figure 6.2j shows two well-resolved pseudo zero-order kinetic states, indicated by the blue lines marked Rate 1 (3.7 monomers/min) and Rate 2 (insertion slowed to the rate of photobleaching). Blue arrows indicate quantized increases corresponding to individual monomer insertion reactions of **6c**. Many such increases are resolved in the intensity vs. time traces, producing a “stair pattern” in the increase in intensity. Some of the individual chemical

events in 2j occurred during kinetic state Rate 1, and thus are plausibly governed by these kinetics. In contrast, kinetics shown in Figure 6.2h, while displaying similar abrupt changes in polymerization states, do not provide sufficiently constant kinetics in any individual state for reasonable linear fitting.

Spatiotemporal variations in catalytic activity can be resolved within the time trace data at 10^{-9} M. If catalytic activity at each polymerization location was identical and/or different but at sufficient concentrations to be ensemble averaged upon detection, all polymerization locations would exhibit the same intensity vs. time curve shapes and absolute magnitudes. Instead, the molecular catalysts exhibit varying kinetics and rates of insertion that are consistent with unique and dynamic local environments.

While zero-order kinetics have been observed in ROMP reactions with norbornene catalyzed by titanium complexes, those kinetics arise from buildup of a catalyst-monomer complex,[27] which is not expected to be the case with ruthenium[28]. Therefore, each pseudo-zero order kinetic state observed by fluorescence microscopy is attributed to measurement of the reaction kinetics under conditions wherein the local effective monomer concentration is not changing significantly. These pseudo-zero order kinetic states are spatiotemporally distributed, i.e. not only at different locations but also at different time points within the same polymer. These clearly resolved changes within the time traces allow for defined kinetic states to be identified. Within these kinetic states, single insertion reactions can be resolved overlaid onto the signal. A lower bound for unique subensemble kinetics was thus established.

An increase in the concentration of **6c** from 10^{-9} M to 10^{-8} M led to a system that continued to exhibit resolvable time-variable chemical kinetic states. The ability to resolve quantized single insertion reactions was limited, however, to a subset of the examined aggregates (e.g., Figure 6.2g

but not 2e or 2f). Time trace data were well-fit by pseudo-zero order kinetics of incorporation of monomer **6c** (Figure 6.2; e, rate = 4.2 monomers/min; f, $rate_1$ = 5.4 monomers/min; g, $rate_1$ = 8.3 monomers/min). These reaction conditions produced an intermediate stage between fully averaged polymerization kinetics and clearly resolvable single ring-opening events.

At a concentration of 10^{-6} M **6c**, precipitated polymers increased rapidly in brightness (Figure 6.2b-d; these conditions necessitated different camera settings, meaning that absolute intensity values at this concentration are not directly comparable to those at lower concentrations). Surprisingly, a degree of kinetic distribution and state-changing information was exhibited and detectable at 10^{-6} M. Though most variation in kinetics was averaged out (Figure 6.2b and 6.2d), different kinetic states could be resolved in a subset of the precipitated polymers, shown by the regions labeled Rate 1 and Rate 2 in Figure 6.2c. This concentration, while below that typical for NMR spectroscopy, is similar to that for benchtop UV-vis-fluorescence spectroscopy.[29] This outcome suggests that standard instrument detectors with a microscopy/spatial resolution component may be sufficient for detection of some of the interesting switching of kinetics states of molecular polymerization catalysts that are usually hidden in ensemble experiments.

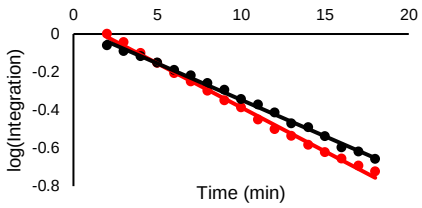

Figure 6.3. Consumption of norbornene and appearance of polynorbornene. Log plot showing first-order kinetics in consumption of norbornene (black data and line) and appearance of polynorbornene (red data and line) as measured by ^{1}H NMR spectroscopy.

For comparison, the kinetics of the polymerization reaction were followed by ^{1}H NMR spectroscopy at 10^{-3} M, using untagged norbornene **6b** in toluene, a solvent in which the catalyst

and polynorbornene were fully soluble so that the ensemble kinetics of the entire sample were analyzed. The chemical kinetics from ^{1}H NMR spectroscopy[30] differ from those obtained via fluorescence microscopy. The reaction follows first-order kinetics via ^{1}H NMR spectroscopy (first-order fits shown in Figure 6.3). Any subensemble reactivity at solubilized molecular catalysts is fully averaged out, and no in-depth chemical information of the time-variable dynamics or distribution of kinetics of the molecular catalysts is available. The degree to which time-variable states might exist in fully soluble, solution phase polymerization reactions remains intriguingly unknown. This set of conditions is therefore insufficient to provide a full, accurate picture of the catalytic activity within the system due to the inherent averaging.

Conclusion

In conclusion, these experiments observe single turnovers at individual molecular catalysts. They determine the kinetic parameters that dictate these single reactions at individual catalysts, by overlaying the signal from individual catalysts onto signal from several, regionally located catalysts that indicate the local polymerization kinetic state[2] (Figure 6.2g-j). Time-variable kinetic states occur and can be resolved from 10^{-9} M to 10^{-6} M, which is unexpectedly high in substrate concentration. This unique chemical information was not available through complementary traditional ^{1}H NMR spectroscopic analysis of the fully soluble reaction mixture (Figure 6.2a), wherein ensemble averaging obscured any potential time-variable catalytic kinetic states. The characterized time-variable catalytic kinetic behavior plausibly dictates macroscopic properties of polymers, for example by determining local variability in comonomer incorporation in block copolymers.[31] These experiments aid in the conceptual understanding of the behavior of individual molecular catalysts—thus revising the concept of uniformity in molecular catalysts.

Experimental

I. General Information

All reagents and solvents were used as received from commercial sources unless otherwise noted. Spectrophotometric grade heptane (OmniSolv®) was purchased from EMD Millipore and was used for all microscopy studies. Catalyst **1** (Grubbs Catalyst, 2nd Generation) was purchased from Sigma-Aldrich. Ultra-pure water with >18 MΩ resistance and total organic content of <5 ppb was obtained from a Milli-Q Gradient A10 water purifier (Millipore, Billerica, MA) using a Q-Gard 2 purification pack and a Quantum EX Ultrapure Organex cartridge. All proton nuclear magnetic resonance (^{1}H NMR) spectra were recorded on a Bruker DRX-500 spectrometer outfitted with a cryoprobe. Chemical shifts were reported in ppm and referenced to the residual protiated solvent peak (δ_H = 2.08 ppm for d_8-toluene) in ^{1}H NMR spectroscopy experiments.

II. Construction of Reaction Cells and Preparation of Coverslips for Microscopy[5]

Glass coverslips (25 × 25 mm, No. 1.5, VWR Scientific) with a thickness of 0.17 mm were cleaned by sonication in 20 mL of a 0.6% solution of Hellmanex Detergent (Fisher Chemical) in MilliQ water for 60 min, then rinsed sequentially with MilliQ water and spectrophotometric grade ethanol six times. The rinsed coverslips were dried with compressed air, then placed on aluminum foil and further dried in an oven at 115 °C for 10 to 20 min. Coverslips were either stored covered in aluminum foil or used immediately after drying.

Bottomless vials were formed by cutting the ends from glass reaction vials (Short Form Style, VWR Scientific). The resulting cylinders were rinsed thoroughly with MilliQ water and spectrophotometric grade ethanol six times and dried in an oven at 115 °C for 20 to 30 min before use in assembling reaction cells.

To assemble the reaction cells, the cleaned and dried hollow bottomless vials were attached to the cleaned coverslips by applying epoxy (Devcon) to the outside base of the tubes, then the assembled tubes were covered with aluminum foil and stored overnight or longer before use in microscopy experiments.

III. Microscopy Parameters

All microscopy imaging was performed with an inverted microscope (IX71, Olympus Corporation) and an oil-immersion, 60x objective with a 1.45 numerical aperture. Samples were imaged with a C9100-13 CCD camera (Hamamatsu Photonics). Fluorescence microscopy samples were illuminated with the 488 nm line obtained from a Ar/Kr ion laser (Coherent Inc.) set to 1.00 W. The CCD chip was a back-thinned electron multiplication type with an effective 512 × 512 array of pixels. The cell size was 16 μm, which with the 60x objective resulted in each pixel in the acquired images representing an area of approximately 270 × 270 nm. The focus was changed with a *z*-axis controller (MS-2000, Applied Scientific Instruments, Inc.). All images were acquired in total internal reflection fluorescence (TIRF).[5] The SlideBook 6.0 software (Intelligent Imaging) was set to acquire images every 1 s with 300 ms exposure to the 488 nm line per frame. Images were viewed in ImageJ (NIH, available at http://rsbweb.nih.gov/ij/). The intensification value was set to 141 for all sample measurements, except the observations at 10^{-6} M, which used an intensification value of one.

The minimum and maximum intensity values of the videos exported from SlideBook were adjusted in ImageJ but are displayed here at constant min/max for all controls and repetitions of data at a given concentration (Section VI and Section IX). When probes **6c** and **6e** were added at *t* = 5 min at a final concentration of 10^{-6} M, 10^{-8} M, and 10^{-9} M, the display values were set to

min = 4000 and max = 12000. When probe **6c** was added at *t* = 5 min at a final concentration of 10^{-12} M, the display values were set to min = 3900 and max = 4800. No gamma correction was used for any video.

IV. Synthetic Procedures

*a. Synthesis of ester norbornene BODIPY probe **6c**.*

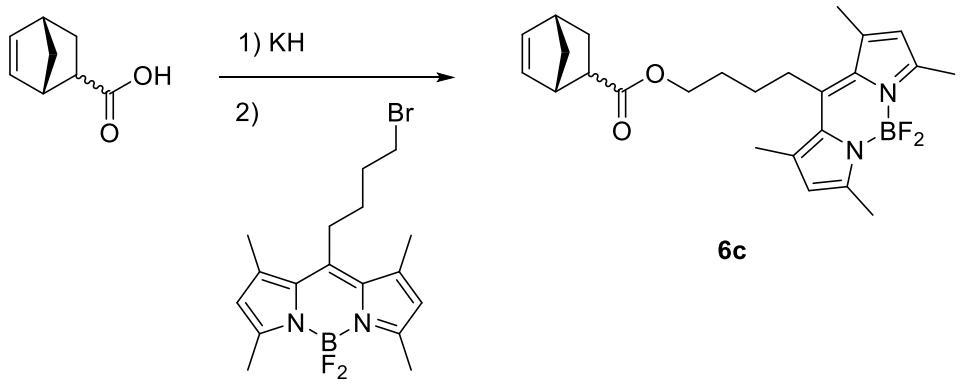

6c

Our laboratory has previously reported the synthesis of ester norbornene BODIPY probe **6c**, the characterization[2] of which is reproduced here for convenience and clarity. ^{1}H NMR spectroscopy analysis showed a 3.0:1.0 mixture of endo:exo isomers of ester norbornene BODIPY. ^{1}H NMR ($CDCl_3$, 500 MHz): δ 6.18 (dd, *J* = 5.5 Hz, 1H), 6.06 (s, 2H), 5.90 (dd, *J* = 5.5 Hz, 1H), 4.08 (t, *J* = 12.5 Hz, 2H), 3.17 (m, 1H), 2.98–2.95 (m, 2H), 2.94–2.89 (m, 2H), 2.52 (s, 6H), 2.42 (s, 6H), 1.90–1.87 (m, 1H), 1.82–1.79 (m, 2H), 1.75–1.72 (m, 2H), 1.44–1.37 (m, 2H), 1.28–1.25 (m, 1H). ^{13}C NMR ($CDCl_3$, 126 MHz): δ 174.8, 154.1, 145.7, 140.2, 138.0, 135.8, 131.9, 121.8, 63.5, 49.7, 45.7, 43.4, 42.6, 29.3, 28.3, 28.0, 16.4, 16.4, 14.5. HRMS (ESI+) *m/z* calcd. for $C_{25}H_{31}O_2N_2BF_2$ ($[M+Na]^+$) 463.2349, found 463.2337.

b. *Synthesis of butyl BODIPY control probe **6e**.*

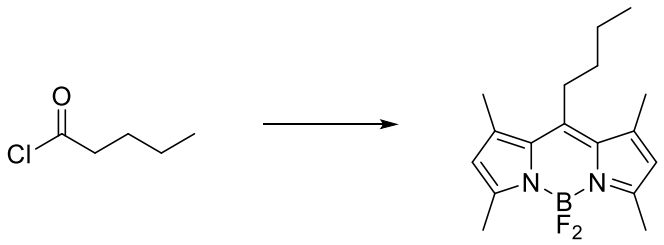

6e

Our laboratory has previously reported the synthesis of butyl BODIPY control probe **6e**, the characterization[5] of which is reproduced here for convenience and clarity. ^{1}H NMR (500 MHz, $CDCl_3$) δ: 6.05 (s, 2H), 2.96–2.90 (m, 2H), 2.51 (s, 6H), 2.41 (s, 6H), 1.66–1.58 (m, 2H), 1.52 (sextet, J = 8 Hz, 2H), 0.99 (t, J = 8 Hz, 3H). ^{13}C NMR (126 MHz, $CDCl_3$) δ: 153.8, 146.9, 140.4, 131.6, 121.7, 33.9, 28.2, 23.6, 14.6 (t, $J_{C–F}$ = 3 Hz), 13.9. HRMS (ESI): m/z calculated $[M+Na]^+$ 327.1823, found 327.1819.

V. Sample Preparation

a. *Preparation of catalyst **6a** for fluorescence microscopy.* In an N_2-filled glove box, catalyst **6a** (1.5 mg, 1.8×10^{-3} mmol) was weighed out into a 1 dram vial, which was then capped and brought out of the box. Spectrophotometric grade heptane (1.0 mL) was added to the vial via syringe. The resulting mixture was gently swirled, then transferred via the same syringe to a prepared microscopy reaction vial. The solution was light pink due to some dissolved catalyst, but much of the catalyst remained insoluble and settled on the bottom of the microscope cover slip inside the reaction vial. The microscopy vial was placed on the microscope, and the top of the cover slip was brought into focus, using room light and catalyst crystals to focus.

b. *Preparation of catalyst **6a** for ^1H NMR spectroscopy.* In an N_2-filled glove box, catalyst **6a** (1.5 mg, 1.8×10^{-3} mmol) was weighed out into a 1 dram vial, which was then capped and brought out of the box. d_8-Toluene (1.00 mL, measured via 2.50 mL gastight syringe [Hamilton Company]) was added to **6a**, which immediately dissolved and gave a faint pink solution of 1.8×10^{-3} M. Separately, the 2.50 mL gastight syringe was used to measure out d_8-toluene (2.00 mL) into a 1 dram vial. A 10 µL gastight syringe (Hamilton Company) was used to transfer 1.8×10^{-3} M stock solution (11 µL) to this volume, affording a 10^{-5} M solution of **6a**. This solution was used in ^{1}H NMR spectroscopy experiments.

c. *Preparation of solutions containing either monomer **6c** or **6e** (control) for microscopy.* Ring-opening metathesis[2] monomer **6c** (1.0 mg, 2.3×10^{-3} mmol) was weighed into a 20 mL glass vial. Spectrophotometric grade heptane (2.0 mL) was added to the vial via syringe, and the solution was sonicated for 1 h to fully dissolve the compound. This afforded a 1.2×10^{-3} M solution of **6c** in heptane, which was green-orange in appearance. Serial dilution using this 1.2×10^{-3} M stock solution, a 10. µL gastight syringe (Hamilton Company), and heptane allowed for the preparation of 10^{-6} M, 10^{-8} M, 10^{-9} M, and 10^{-12} M solutions of **6c** in heptane. The solutions of **6c** prepared via serial dilution were clear and colorless in appearance, with the exception of the 10^{-6} M solution, which was faint green.

Preparation of solutions containing control probe **6e** (1.0 mg, 2.3×10^{-3} mmol) instead of monomer **6c** followed the same procedure. Concentrations of 10^{-6} M, 10^{-8} M, and 10^{-9} M of control probe **6e** in heptane were thus obtained. The solutions of **6e** prepared via serial dilution were clear and colorless in appearance, with the exception of the 10^{-6} M solution, which was faint green.

VI. Image Acquisition of Rate Kinetics of Polymerization of Monomer **6c** via In Operando Fluorescence Microscopy

a. *Resolution of single ring-opening events at molecular catalysts in pre-initiated polynorbornene using probe **6c** at 10^{-12} M.* In a 1 dram vial, norbornene (0.6 mg, 6×10^{-6} mol) was weighed out and dissolved in heptane (0.25 mL), added via syringe. This solution was taken up into the same syringe, then added all at once to the mixture of catalyst **6a** in heptane (Section Va), yielding a final solution volume of 1.25 mL. The resultant concentration of norbornene was 0.005 M. Immediately after the solution was added, the sample was focused in TIRF, and video acquisition of the sample began (Section III). The stage was not moved after the sample was focused on the cover slip.

Upon initiating video acquisition of the sample and focusing close to TIRF, neither bright green round polymer spheres nor any bright green flashes were visible on the glass cover slip surface. These observations were not visible due to the absence of fluorescent species in solution. Holding the focus area constant for 5 min confirmed there was no increase in fluorescence intensity at the precipitated polymers.

At the end of the 5 min observation window, the mother liquor was removed via syringe. Then, a 10^{-12} M (0.25 mL, 2.5×10^{-16} mol) solution of **6c** in spectrophotometric grade heptane (Section Vc) was added to the residual precipitated polynorbornene via syringe. The sample was focused into TIRF upon addition of **6c**. Video acquisition over a 5 min period revealed dynamic bright green flashing at the surfaces of the precipitated polynorbornene spheres (Figure 6.4). Since molecular catalysts are contained within polynorbornene, and monomer **6c** is chemospecific to ring-opening metathesis, the bright green flashes at the precipitated polymers are consistent with single ring-opening metathesis reactions at molecular catalysts.

Time trace data graphs were compiled by first selecting a 2×2 pixel region of the polymer, corresponding to 534×534 nm^2. ImageJ gave an output of intensity values at specific times, which were plotted using Excel. The value $t = 0$ refers to the starting time of the video. The lowest intensity value from all points collected was then subtracted, giving the total overall intensity change (Figure 6.4). Examination of the time trace data acquired from specific locations of the bright green flashes revealed quantized intensity increases and decreases consistent with the fingerprints of single molecules.[26] These time traces confirmed ring-opening metathesis occurred at active molecular polymerization catalysts within polynorbornene.

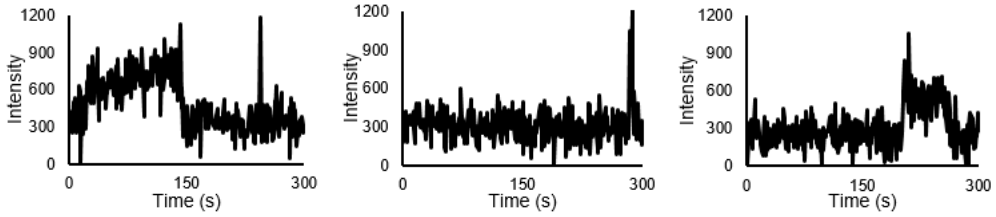

Figure 6.4. Examples of single ring-opening metatheses of **6c** at a concentration of 10^{-12} M by molecular catalysts into precipitated polynorbornene.

b. *Resolution of chemical kinetics and kinetic states at molecular catalysts in polynorbornene using probe **6c** at 10^{-9} M.* In a 1 dram vial, norbornene (0.6 mg, 6×10^{-6} mol) was weighed out and dissolved in heptane (0.25 mL), added via syringe. This solution was taken up into the same syringe, then added all at once to the mixture of catalyst **6a** in heptane (Section Va), yielding a final solution volume of 1.25 mL. The resultant concentration of norbornene was 0.005 M. Immediately after the solution was added, the sample was focused in TIRF, and video acquisition of the sample began (Section III). The stage was not moved after the sample was focused on the cover slip.

Upon initiating video acquisition of the sample and focusing close to TIRF, neither bright green round polymer spheres nor any bright green flashes were visible on the glass cover slip

surface. These observations were not visible due to the absence of fluorescent species in solution. Holding the focus area constant for 5 min confirmed there was no increase in fluorescence intensity at the precipitated polymers.

At the end of the 5 min observation window, the mother liquor was removed via syringe. Then, a 10^{-9} M (0.25 mL, 2.5×10^{-13} mol) solution of **6c** in spectrophotometric grade heptane (Section Vc) was added to the residual precipitated polynorbornene. The sample was focused into TIRF upon addition of **6c**. Over the progression of the following 5 min acquisition window, the brightness and fluorescence intensity at the precipitated polymers increased. The brightness of these polymers was nonuniform: some polymers appeared brighter than others did, and there appeared to be no correlation between polymer brightness and polymer size. Since the concentration of **6c** had been increased by 1000×, there was more available monomer for insertion into the precipitated polymers, leading to an increase in fluorescence intensity rather than photobleaching of single monomers. Therefore, the rate of ring-opening metathesis of **6c** at this concentration outcompetes photobleaching.

Time trace analysis showed that individual quantized steps up could be resolved within the data. These quantized steps up (raw data, Figure 6.5; see Main Text, Figure 6.2 for details) appeared faster than photobleaching, confirming the rate of insertion outcompeted photobleaching. Additionally, within the time traces, regions of fluorescence intensity increases appeared linear, and the particles abruptly changed from inserting monomer to slower rates and/or not inserting monomer. These data are consistent with the resolution of kinetics[2] and kinetic states of reaction during ring-opening metathesis. Further, these kinetic states do not occur at the same time, nor for the same length of time in different particles.

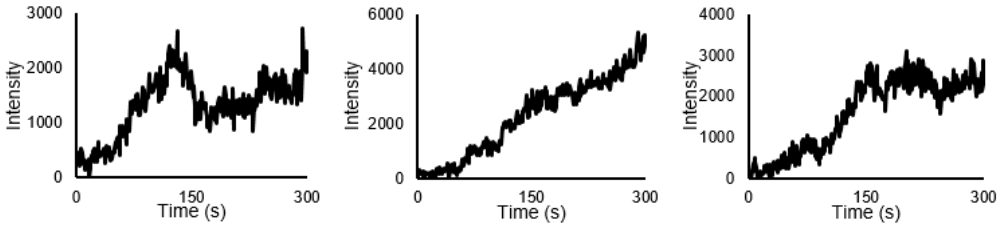

Figure 6.5. Increase in fluorescence intensity faster than photobleaching with resolvable quantized steps up, resulting from insertion of **6c** at a concentration of 10^{-9} M by molecular catalysts into precipitated polynorbornene.

c. *Resolution of chemical kinetics and kinetic states at molecular catalysts in polynorbornene using probe **6c** at 10^{-8} M.* In a 1 dram vial, norbornene (0.6 mg, 6×10^{-6} mol) was weighed out and dissolved in heptane (0.25 mL), added via syringe. This solution was taken up into the same syringe, then added all at once to the mixture of catalyst **6a** in heptane (Section Va), yielding a final solution volume of 1.25 mL. The resultant concentration of norbornene was 0.005 M. Immediately after the solution was added, the sample was focused in TIRF, and video acquisition of the sample began (Section III). The stage was not moved after the sample was focused on the cover slip.

Upon initiating video acquisition of the sample and focusing close to TIRF, neither bright green round polymer spheres nor any bright green flashes were visible on the glass cover slip surface. These observations were not visible due to the absence of fluorescent species in solution. Holding the focus area constant for 5 min confirmed there was no increase in fluorescence intensity at the precipitated polymers.

At the end of the 5 min observation window, the mother liquor was removed via syringe. Then, a 10^{-8} M (0.25 mL, 2.5×10^{-12} mol) solution of **6c** in spectrophotometric grade heptane (Section Vc) was added to the residual precipitated polynorbornene. The sample was focused into TIRF upon addition of **6c**. Over the progression of the following 5 min acquisition window, the brightness and fluorescence intensity at the precipitated polymers increased. Polymer size and

brightness varied, with no correlation between polymer brightness and polymer size. The rate of ring-opening metathesis of **6c** at this concentration also outcompetes photobleaching and self-quenching. Thus, nanomolar concentrations of **6c** are sufficient for resolving fluorescence intensity increases faster than photobleaching.

Time trace analysis of the data further confirms insertion of **6c** faster than concurrent photobleaching (Figure 6.6). Quantized fluorescence intensity increases are visible within the data. However, within the time traces, although the individual quantized steps up could still be resolved, predominantly the increases in intensity were most similar to a linear increase[2] (see Main Text Figure 6.2 for details). These linear increases were steeper than the data using **6c** at 10^{-9} M. The rates of insertion could be fit with lines for increases in intensity units (see Main Text Figure 6.2 for details), showing differences in chemical kinetics of the active molecular catalysts within the precipitated polymers. Time points of the kinetic states of active catalysts varied, evidenced by the differing rates of insertion (Figure 6.6). Therefore, this concentration of fluorophore is sufficient to resolve not only single insertion events in a subset of particles but also kinetic states of reaction.

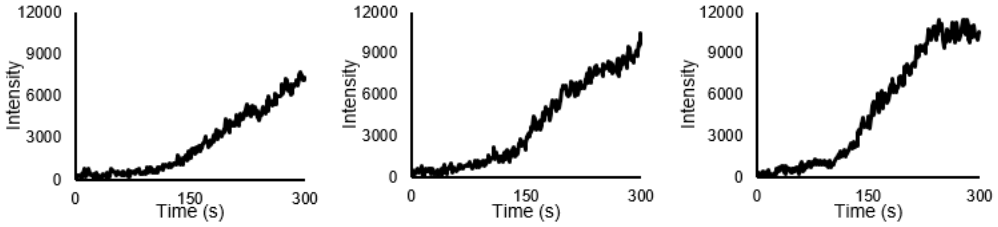

Figure 6.6. Increase in fluorescence intensity faster than photobleaching with resolvable kinetic states, resulting from insertion of **6c** at a concentration of 10^{-8} M by molecular catalysts into precipitated polynorbornene.

d. *Qualitative resolution of kinetic states of polymerization at molecular catalysts in pre-initiated polynorbornene using probe **6c** at 10^{-6} M.* In a 1 dram vial, norbornene (0.6 mg, 6×10^{-6} mol) was weighed out and dissolved in heptane (0.25 mL), added via syringe.

This solution was taken up into the same syringe, then added all at once to the mixture of catalyst **6a** in heptane (Section Va), yielding a final solution volume of 1.25 mL. The resultant concentration of norbornene was 0.005 M. Immediately after the solution was added, the sample was focused in TIRF, and video acquisition of the sample began (Section III). The stage was not moved after the sample was focused on the cover slip.

When video acquisition of the sample was initiated and focused close to TIRF, neither bright green round polymer spheres nor any bright green flashes were visible on the glass cover slip surface. These observations were not visible due to the absence of fluorescent species in solution. Holding the focus area constant for 5 min confirmed there was no increase in fluorescence intensity at the precipitated polymers.

At the end of the 5 min observation window, the mother liquor was removed via syringe. Then, a 10^{-6} M (0.25 mL, 2.5×10^{-9} mol) solution of **6c** in spectrophotometric grade heptane (Section Vc) was added to the residual precipitated polynorbornene. The sample was focused into TIRF upon addition of **6c**. Over the progression of the following 5 min acquisition window, the brightness and fluorescence intensity at the precipitated polymers increased. Polymer size and brightness varied, with no correlation between polymer brightness and polymer size. Notably, some polymers increased in brightness such that the surface of the cover slip was no longer resolvable, nor were the sizes and shapes of polymers. Therefore, the data suggest that subensemble measurement ability is still present but nearly lost, due to the higher concentration of fluorophore.

Time trace analysis of the data confirms insertion of **6c** faster than concurrent photobleaching (Figure 6.7). However, at this concentration, only qualitative analysis of the data is available. Since the measurements were taken using intensification of one, rather than 141, the

increases represent general shapes rather than quantifiable data. Nonetheless, the data is not so averaged that kinetic states cannot be resolved in a subset of examined particles.

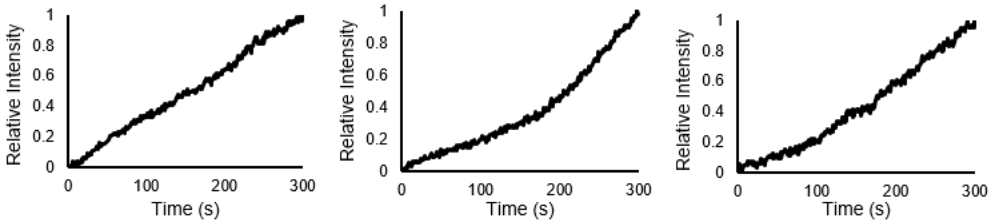

Figure 6.7. Linear increases in fluorescence intensity faster than photobleaching with resolvable kinetic states, resulting from insertion of **6c** at a concentration of 10^{-6} M by molecular catalysts into precipitated polynorbornene.

VII. ^{1}H NMR Spectroscopy of Molecular Polymerization Catalysts

A solution of catalyst **6a** was prepared according to the procedures described in Section Vb. Following the preparation, a 1.00 mL gastight syringe (Hamilton Company) was used to dispense the solution of catalyst **6a** into three NMR tubes (0.40 mL added to each NMR tube). In a 1 dram vial, norbornene (3.3 mg, 3.5×10^{-5} mol) was weighed out and dissolved in d_8-toluene (0.50 mL), added via 1.00 mL gastight syringe. The effective concentration of norbornene was 6.4×10^{-3} M.

For each experimental run, the 0.40 mL aliquots of catalyst **6a** in d_8-toluene were placed in the Bruker DRX-500 spectrometer, and then shimmed. Prior to running the experiment, the NMR tube was removed, and exactly 0.10 mL of the solution of norbornene in d_8-toluene was added to the NMR tube via gastight syringe. The effective concentration of norbornene was 1.3×10^{-3} M, and the effective concentration of catalyst **6a** was 8.0×10^{-6} M. The tube was capped, inverted three times, and replaced in the Bruker DRX-500 spectrometer. Spectra were acquired every minute with single scan settings.

In the three experimental runs, the concentration of norbornene decreased, and the concentration of polynorbornene increased. The observations were concluded based on the gradual disappearance of the norbornene sp^2 C–H peak (δ 5.95 ppm), and the appearance of two polynorbornene sp^2 C–H peaks (5.48, 5.33 ppm). These peaks were chosen because although other norbornene peaks disappeared and other polynorbornene peaks appeared, the sp^2 peaks were easily differentiable from each other.

The values from the experimental runs were normalized and plotted into an integration vs. time graph (Figure 6.8). Both the consumption of norbornene and the appearance of polynorbornene appeared as curves on the graphs, and their shapes nearly mirrored one another. Plotting the natural log of the integration vs. time revealed first-order kinetics for both consumption of norbornene and appearance of polynorbornene.

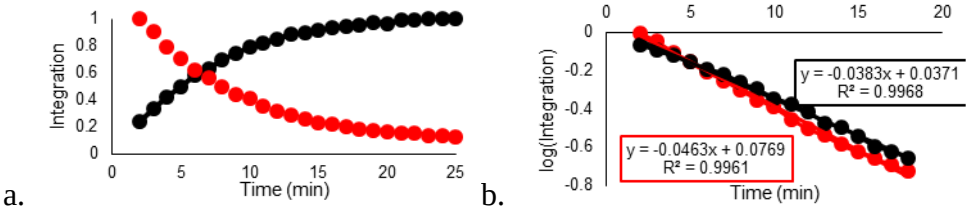

Figure 6.8. ^{1}H NMR spectroscopy study of norbornene consumption and polynorbornene appearance. a) Relative integration values of disappearance of norbornene (red curve) and appearance of polynorbornene (black curve) over time. b) Log plots with first-order linear fits of relative integration values of norbornene disappearance (red line) and polynorbornene appearance (black line) over time.

VIII. Control Experiments for Assignment of Fluorescent Regions as Products of Ring-Opening Metathesis Polymerization

a. *Use of control probe **6e** in place of **6c** at 10^{-9} M.* In a 1 dram vial, norbornene (0.6 mg, 6×10^{-6} mol) was weighed out and dissolved in heptane (0.25 mL), added via syringe. This solution was taken up into the same syringe, then added all at once to the mixture of catalyst

6a in heptane (Section Va), yielding a final solution volume of 1.25 mL. The resultant concentration of norbornene was 0.005 M. Immediately after the solution was added, the sample was focused in TIRF, and video acquisition of the sample began (Section III). The stage was not moved after the sample was focused on the cover slip.

Upon initiating video acquisition of the sample and focusing close to TIRF, neither bright green round polymer spheres nor any bright green flashes were visible on the glass cover slip surface. These observations were not visible due to the absence of fluorescent species in solution. Holding the focus area constant for 5 min confirmed there was no increase in fluorescence intensity at the precipitated polymers.

At the end of the 5 min observation window, the mother liquor was removed via syringe. Then, a 10^{-9} M (0.25 mL, 2.5×10^{-13} mol) solution of **6e** in spectrophotometric grade heptane (Section Vc) was added to the residual precipitated polynorbornene. The sample was focused into TIRF upon addition of **6e**. Over the progression of the following 5 min acquisition window, no bright green flickers could be seen (Figure 6.9), nor were any bright green areas of polymer growth resolved on the surface of the cover slip, in contrast to Figure 6.5. Therefore, the growth of the fluorescent green polymer faster than photobleaching is due to chemical incorporation of **6c** into the polymer, and is not due to physical uptake of any probe into the polymer.

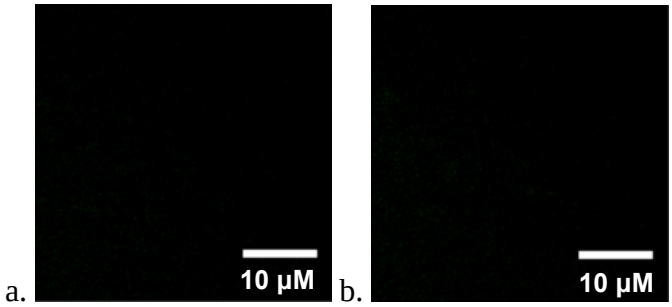

Figure 6.9. Image of absence of reactivity and/or incorporation of control probe **6e** at 10^{-9} M. Images acquired at a) t = 0 s and b) t = 300 s, displayed at identical min/max as the data resulting in Figure 6.5.

b. *Use of control probe **6e** in place of **6c** at 10^{-8} M.* In a 1 dram vial, norbornene (0.6 mg, 6×10^{-6} mol) was weighed out and dissolved in heptane (0.25 mL), added via syringe. This solution was taken up into the same syringe, then added all at once to the mixture of catalyst **6a** in heptane (Section Va), yielding a final solution volume of 1.25 mL. The resultant concentration of norbornene was 0.005 M. Immediately after the solution was added, the sample was focused in TIRF, and video acquisition of the sample began (Section III). The stage was not moved after the sample was focused on the cover slip.

Upon initiating video acquisition of the sample and focusing close to TIRF, neither bright green round polymer spheres nor any bright green flashes were visible on the glass cover slip surface. These observations were not visible due to the absence of fluorescent species in solution. Holding the focus area constant for 5 min confirmed there was no increase in fluorescence intensity at the precipitated polymers.

At the end of the 5 min observation window, the mother liquor was removed via syringe. Then, a 10^{-8} M (0.25 mL, 2.5×10^{-12} mol) solution of **6e** in spectrophotometric grade heptane (Section Vc) was added to the residual precipitated polynorbornene. The sample was focused into TIRF upon addition of **6e**. Over the progression of the following 5 min acquisition window, no bright green areas of polymer growth could be resolved on the surface of the cover slip (Figure 6.10), in contrast to Figure 6.6. Therefore, the growth of the fluorescent green polymer faster than photobleaching is due to chemical incorporation of **6c** into the polymer, and is not due to physical uptake of any probe into the polymer.

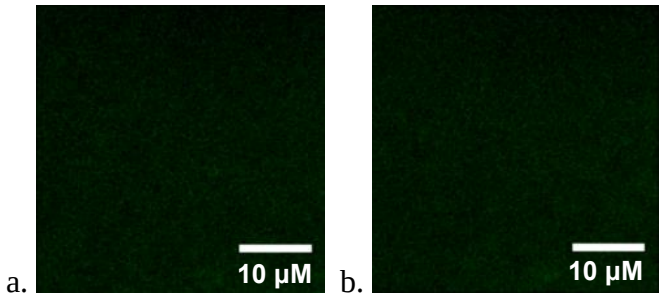

Figure 6.10. Image of absence of reactivity and/or incorporation of control probe **6e** at 10^{-8} M. Images acquired at a) t = 0 s and b) t = 300 s, displayed at identical min/max as the data resulting in Figure 6.6.

c. *Use of control probe **6e** in place of **6c** at 10^{-6} M.* In a 1 dram vial, norbornene (0.6 mg, 6×10^{-6} mol) was weighed out and dissolved in heptane (0.25 mL), added via syringe. This solution was taken up into the same syringe, then added all at once to the mixture of catalyst **6a** in heptane (Section Va), yielding a final solution volume of 1.25 mL. The resultant concentration of norbornene was 0.005 M. Immediately after the solution was added, the sample was focused in TIRF, and video acquisition of the sample began (Section III). The stage was not moved after the sample was focused on the cover slip.

Upon initiating video acquisition of the sample and focusing close to TIRF, neither bright green round polymer spheres nor any bright green flashes were visible on the glass cover slip surface. These observations were not visible due to the absence of fluorescent species in solution. Holding the focus area constant for 5 min confirmed there was no increase in fluorescence intensity at the precipitated polymers.

At the end of the 5 min observation window, the mother liquor was removed via syringe. Then, a 10^{-6} M (0.25 mL, 2.5×10^{-9} mol) solution of **6e** in spectrophotometric grade heptane (Section Vc) was added to the residual precipitated polynorbornene. The sample was focused into TIRF upon addition of **6e**. Due to the brightness of the solution background, over the progression of the following 5 min acquisition window, the precipitated polymers could be seen on the surface

of the cover slip, but they did not increase in brightness or fluorescence intensity (Figure 6.11), in contrast to Figure 6.7. Therefore, despite being able to see the shapes of the polymers, the imaging data is clearly different in the case of the control probe.

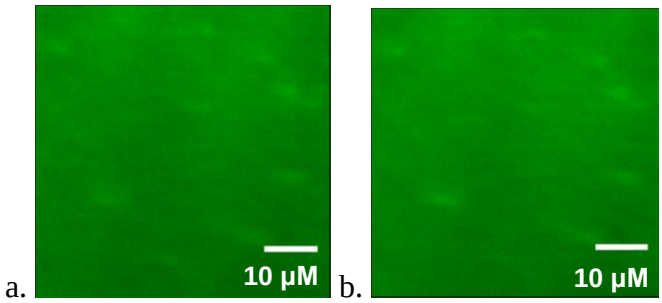

Figure 6.11. Image of absence of reactivity and/or incorporation of control probe **6c** at 10^{-6} M. Images acquired at a) t = 0 s and b) t = 300 s, displayed at identical min/max as the data resulting in Figure 6.7.

References

(1) Easter, Q. T.; Blum, S. A. *Angew. Chem. Int. Ed.* **2017**, *56*, 13772–13775.
(2) Easter, Q. T.; Blum, S. A. *Angew. Chem. Int. Ed.* **2018**, *57*, 1572–1575.
(3) Liu, C.; Kubo, K.; Wang, E.; Han, K.-S.; Yang, F.; Chen, G.; Escobedo, F. A.; Coates, G. W.; Chen, P. *Science* **2017**, *358*, 352–355.
(4) Cordes, T.; Blum, S. A. *Nat. Chem.* **2013**, *5*, 993–999.
(5) Esfandiari, N. M.; Wang, Y.; Bass, J. Y.; Cornell, T. P.; Otte, D. A. L.; Cheng, M. H.; Hemminger, J. C.; Mcintire, T. M.; Mandelshtam, V. A.; Blum, S. A. *J. Am. Chem. Soc.* **2010**, *132*, 15167–15169.
(6) Feng, C.; Cunningham, D. W.; Easter, Q. T.; Blum, S. A. *J. Am. Chem. Soc.* **2016**, *138*, 11156–11159.
(7) Feng, C.; Easter, Q. T.; Blum, S. A. *Organometallics* **2017**, *36*, 2389–2396.
(8) Rybina, A.; Lang, C.; Wirtz, M.; Grußmayer, K.; Kurz, A.; Maier, F.; Schmitt, A.; Trapp, O.; Jung, G.; Herten, D.-P. *Angew. Chem. Int. Ed.* **2013**, *52*, 6322–6325.
(9) Ng, J. D.; Upadhyay, S. P.; Marquard, A. N.; Lupo, K. M.; Hinton, D. A.; Padilla, N. A.; Bates, D. M.; Goldsmith, R. H. *J. Am. Chem. Soc.* **2016**, *138*, 3876–3883.
(10) Blum, S. A. *Phys. Chem. Chem. Phys.* **2014**, *16*, 16333–16339.
(11) Esfandiari, N. M.; Blum, S. A. *J. Am. Chem. Soc.* **2011**, *133*, 18145–18147.
(12) Hensle, E. M.; Blum, S. A. *J. Am. Chem. Soc.* **2013**, *135*, 12324–12328.
(13) Chen, P.; Zhou, X.; Andoy, N. M.; Han, K.-S.; Choudhary, E.; Zou, N.; Chen, G.; Shen, H. *Chem. Soc. Rev.* **2014**, *43*, 1107–1117.
(14) Buurmans, I. L. C.; Weckhuysen, B. M. *Nat. Chem.* **2012**, *4*, 873–886.
(15) Easter, Q. T.; Trauschke, V.; Blum, S. A. *ACS Catal.* **2015**, *5*, 2290–2295.
(16) Roeffaers, M. B. J.; Sels, B. F.; Uji-i, H.; De Schryver, F. C.; Jacobs, P. A.; De Vos, D. E.; Hofkens, J. *Nature* **2006**, *439*, 572–575.
(17) Sambur, J. B.; Chen, T. Y.; Choudhary, E.; Chen, G.; Nissen, E. J.; Thomas, E. M.; Zou, N.; Chen, P. *Nature* **2016**, *530*, 77–80.

(18) Kubarev, A. V.; Janssen, K. P. F.; Roeffaers, M. B. J. *ChemCatChem* **2015**, *7*, 3646–3650.
(19) Ristanović, Z.; Kubarev, A. V; Hofkens, J.; Roeffaers, M. B. J.; Weckhuysen, B. M. *J. Am. Chem. Soc.* **2016**, *138*, 13586–13596.
(20) Nevskyi, O.; Sysoiev, D.; Oppermann, A.; Huhn, T.; Wöll, D. *Angew. Chem. Int. Ed.* **2016**, *55*, 12698–12702.
(21) Wöll, D.; Braeken, E.; Deres, A.; De Schryver, F. C.; Uji-i, H.; Hofkens, J. *Chem. Soc. Rev.* **2009**, *38*, 313–328.
(22) Flier, B. M. I.; Baier, M.; Huber, J.; Müllen, K.; Mecking, S.; Zumbusch, A.; Wöll, D. *Phys. Chem. Chem. Phys.* **2011**, *13*, 1770–1775.
(23) Mol, J. C. *J. Mol. Catal. A: Chem.* **2004**, *213*, 39–45.
(24) Walsh, D. J.; Lau, S. H.; Hyatt, M. G.; Guironnet, D. *J. Am. Chem. Soc.* **2017**, *139*, 13644–13647.
(25) Esfandiari, N. M.; Wang, Y.; Bass, J. Y.; Blum, S. A. *Inorg. Chem.* **2011**, *50*, 9201–9203.
(26) Lakowicz, J. R. *Principles of Fluorescence Spectroscopy*, 3rd ed.; Springer: New York, **2006**.
(27) Gilliom, L. R.; Grubbs, R. H. *J. Am. Chem. Soc.* **1986**, *108*, 733–742.
(28) Romero, P. E.; Piers, W. E. *J. Am. Chem. Soc.* **2005**, *127*, 5032–5033.
(29) Lim, S.-G.; Blum, S. A. *Organometallics* **2009**, *28*, 4643–4645.
(30) Sanford, M. S.; Love, J. A.; Grubbs, R. H. *J. Am. Chem. Soc.* **2001**, *123*, 6543–6554.
(31) Schacher, F. H.; Rupar, P. A.; Manners, I. *Angew. Chem. Int. Ed.* **2012**, *51*, 7898–7921.